National Library of Canada
Acquisitions and Bibliographic Services Branch
395 Wellington Street
Ottawa, Ontario
K1A 0N4

Bibliothèque nationale du Canada
Direction des acquisitions et des services bibliographiques
395, rue Wellington
Ottawa (Ontario)
K1A 0N4

Your file Votre référence

Our file Notre référence

NOTICE

The quality of this microform is heavily dependent upon the quality of the original thesis submitted for microfilming. Every effort has been made to ensure the highest quality of reproduction possible.

If pages are missing, contact the university which granted the degree.

Some pages may have indistinct print especially if the original pages were typed with a poor typewriter ribbon or if the university sent us an inferior photocopy.

AVIS

La qualité de cette microforme dépend grandement de la qualité de la thèse soumise au microfilmage. Nous avons tout fait pour assurer une qualité supérieure de reproduction.

S'il manque des pages, veuillez communiquer avec l'université qui a conféré le grade.

La qualité d'impression de certaines pages peut laisser à désirer, surtout si les pages originales ont été dactylographiées à l'aide d'un ruban usé ou si l'université nous a fait parvenir une photocopie de qualité inférieure.

Canada

Compliant Articulated Robot Leg
With Antagonistic LADD Actuation

Giuseppe Mennitto

Department of Mechanical Engineering
McGill University, Montréal, Canada

February 1995

A Thesis submitted to the Faculty of Graduate Studies and Research in partial fulfillment of the requirements of the degree of Master's of Engineering.

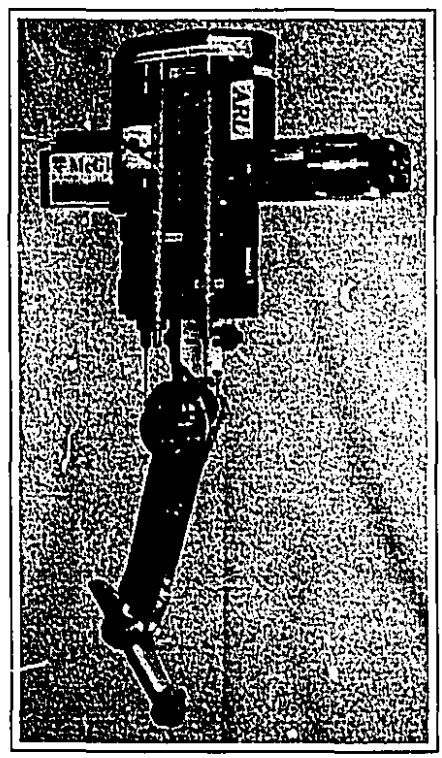

ISBN 0-612-05463-2

Canada

Dedica a mia mamma,

Desidero esprimere la mia sincera gratitudine per il grande sopporto morale che mia mamma mi ha offerto durante questi lunghi anni dedicati agli studi. Il suo costante incoraggiamento e amore mi hanno permesso di continuare anche nei momenti più critici. Ne approfitto dunque per ringraziarla di tutto cuore.

Con affetto,

Giuseppe

Abstract

This thesis describes a new Compliant Articulated Robot Leg (CARL) which is a prototype leg for an autonomous quadruped robot. The leg is designed for dynamic walking, trotting and bounding gaits, with an expected top speed of $3m/s$. To facilitate the construction of multi-legged creatures, the leg was designed as a modular, self-contained unit with integrated amplifiers and control electronics. It is an articulated 3 DOF design with revolute joints as opposed to prismatic joints for improved mobility, simplicity and low friction. It employs electric actuation instead of hydraulics for indoor power autonomy, improved modeling, control and reliability. The use of fractional horsepower DC motors in a running robot is feasible through a novel AnTagonistic LADD Actuation System (ATLAS) which converts motor effort to high joint torques with similar efficiencies as the best conventional transmissions, but at substantial weight savings.

Résumé

Cette thèse décrit une nouvelle jambe robotique articulée nommée CARL ("Compliant Articulated Robot Leg") servant comme prototype d'une jambe d'un robot quadrupède qui est conçue pour marcher, trotter et sauter à une vitesse maximale prévue de $3m/s$. Pour faciliter la construction des créatures a jambes multiples, cette jambe a été créé d'une façon modulaire et autonome possédant des amplificateurs intégrés et des circuits de contrôle électroniques. C'est un modèle articulée possédant 3 degrés de liberté et des articulations à révolution au lieu d'articulations prismatiques. Ces caractéristiques mènent à une meilleure mobilité, une simplicité et faible friction. La jambe utilise l'énergie électrique au lieu d'hydraulique pour fournir une puissance autonome, ainsi qu'un model, un contrôle et une fiabilité amélioré. L'utilisation d'un moteur à courant continu et à faible puissance dans un robot est devenu possible grâce au nouveau système "An'Tagonistic LADD Actuation System" (ATLAS) qui transforme la puissance d'un moteur en moment de torsion élevé ayant une efficacité semblable à celle des systèmes de transmission conventionelle et cela est effectué avec une conservation de poids substantielle.

Acknowledgements

I wish to thank the following people for their timely contributions which helped me through to the completion of my degree:

- Martin Buehler, my supervisor and friend, for getting me interested in legged locomotion, believing in my design choices and overall generous support;
- Pedro Gregorio, fellow colleague and friend, for his continuous assault of questions and jokes;
- Patrick Grégoire, Tommy Marincic and Olivier Payant, three undergraduate students who helped design and build CARL;
- Mojtaba Ahmadi for his knowledge of CIM's computer facilities and various software packages;
- Andrew Ogilvie, summer student extraordinaire, for helping me build LADDs and taking dozens of CARL photos;
- Nadim El-fata for his electrical expertise; and,
- Sandy Meek of the University of Utah for relating his experience from working with LADDs.

I also acknowledge the support of the Natural Sciences and Engineering Research Council of Canada through an NSERC PGSA scholarship. In addition, this work was supported by an FCAR New Researcher Grant and by an NSERC/CIAR junior industrial research chair, held by my supervisor, Prof. M. Buehler.

Contents

List of Figures

List of Tables

Chapter 1

Introduction

1.1 Goals of Dynamic Legged Robot Research

Legged locomotion is a useful form of robot movement. Unlike wheeled robots, which are restricted to a locally flat environment, legged robots have the ability to negotiate uneven terrains. This type of maneuverability is extremely practical and may make legged systems the mobile platform of choice in many applications. Tracked vehicles are a good trade-off between wheeled and legged systems in terms of complexity and terrain maneuverability. However, neither wheeled nor tracked vehicles can exhibit similar mobility, efficiency and dexterity as legged robots.

Introducing dynamic operation and active balance to legged robots promises further performance improvements over static walkers. The latter, which do not balance actively, require at least three legs in contact with the ground to maintain stability. Dynamic operation eliminates this restriction and permits a dramatic increase in mobility and speed through running gaits, jumps and dynamic balance.

Past legged robot research has focused primarily on control and less heavily on design. With more sophisticated control algorithms has come an increased demand on the mechanics of robot design. It is fair to say, aside from control, that the performance of any system is a function of its physical nature: structure, actuation

and energy source. This thesis focuses on improvements on the first two aspects for dynamic legged robot design.

1.2 Biological Legs

For the design of a robot leg, it is instructive to look at biological models for inspiration. Their developments are the result of millions of years of natural selection and evolution. The great diversity of leg types is due to this very advanced adaptation, enabling a broad study of existing models. Different types of legs generate different gaits: the hopping of kangaroos, the pacing of camels, the galloping of horses, and the bipedal locomotion of humans. These are but a few examples of nature's adaptation process and many more can be found in [27].

Knowing the specifications of a robot leg (size, speed of gait, number of articulations), it can be useful to find biological legs that possess these same qualities. The specific features of the biological legs can then be incorporated into the design. A look at a particular biological system also helps with the dynamic aspect of legged robot design by understanding the action of the muscles, tendons and bones on the overall performance of the leg. The horse has been known to maintain a speed of $70km/h$ for $55km$ [15]. It may be natural to think that such a performance is mainly due to the horse's extraordinary metabolism, but the design of the animal's legs plays a key role in optimizing speed and minimizing effort. What could explain in part the efficiency is the elastic ligaments in the lower leg that are able to store energy when the hoof strikes the ground, and then reuse the same energy to impart forward momentum to the leg. In addition, the large number of articulations increases its potential for speed. But for a robot leg, the addition of an extra leg segment increases the system complexity, which cannot be justified by a small increase in speed. However, leg compliance is an option to be considered for improved system efficiency.

R. McN. Alexander and T. A. McMahon are just a few of the leading researchers in animal locomotion. An extensive review of the mechanics, energetics and diversity

of animal locomotion can be found in [7, 9, 15, 25].

1.3 Dynamic Legged Robot Designs

Much of the work on dynamically stable legged robot design has come from M. H. Raibert [35] who built many different running robots based on prismatic (telescoping) legs. He started with a planar one-legged machine and followed with a 3D one-legged robot shown in Fig. 1.1 (top left) which recorded a top running speed of $2.2m/s$. The follow-up to this robot is a 3D two-legged machine (Fig. 1.1, top right), where each leg has four actuated degrees of freedom. He also built a quadruped (Fig. 1.1, bottom left) which performs a variety of gaits that include trotting, pacing and bounding. Most recently, Raibert built a one-legged robot kinematically similar to a kangaroo's leg [37]. Some features of this robot leg, shown in Fig. 1.1 (bottom right), include revolute joints as opposed to prismatic, and an ankle tendon responsible for adding compliance to the hopping motion of the robot. Except for the first one-legged planar hopper, which was pneumatically actuated, his designs use powerful hydraulic actuators and rely on pneumatics for the leg spring only. In this way, Raibert effectively eliminated power constraints and focused exclusively on robot control issues with a great deal of success.

K. V. Papantoniou [30, 31] built an electrically powered actively balanced one-legged planar machine, illustrated in Fig. 1.2. It weighs $7.5kg$ and is capable of operating with an average $48W$ power requirement at a maximum speed of $0.3m/s$. The leg design consists of a four-bar linkage system that emulates the behaviour of a prismatic leg while conserving the mechanical efficiency of an articulated design. A clutch engages the spinning motor at maximum leg compression to maximize energy transfer to the leg.

There are many more research laboratories working on dynamic legged locomotion and an extensive review of the research can be found in [36].

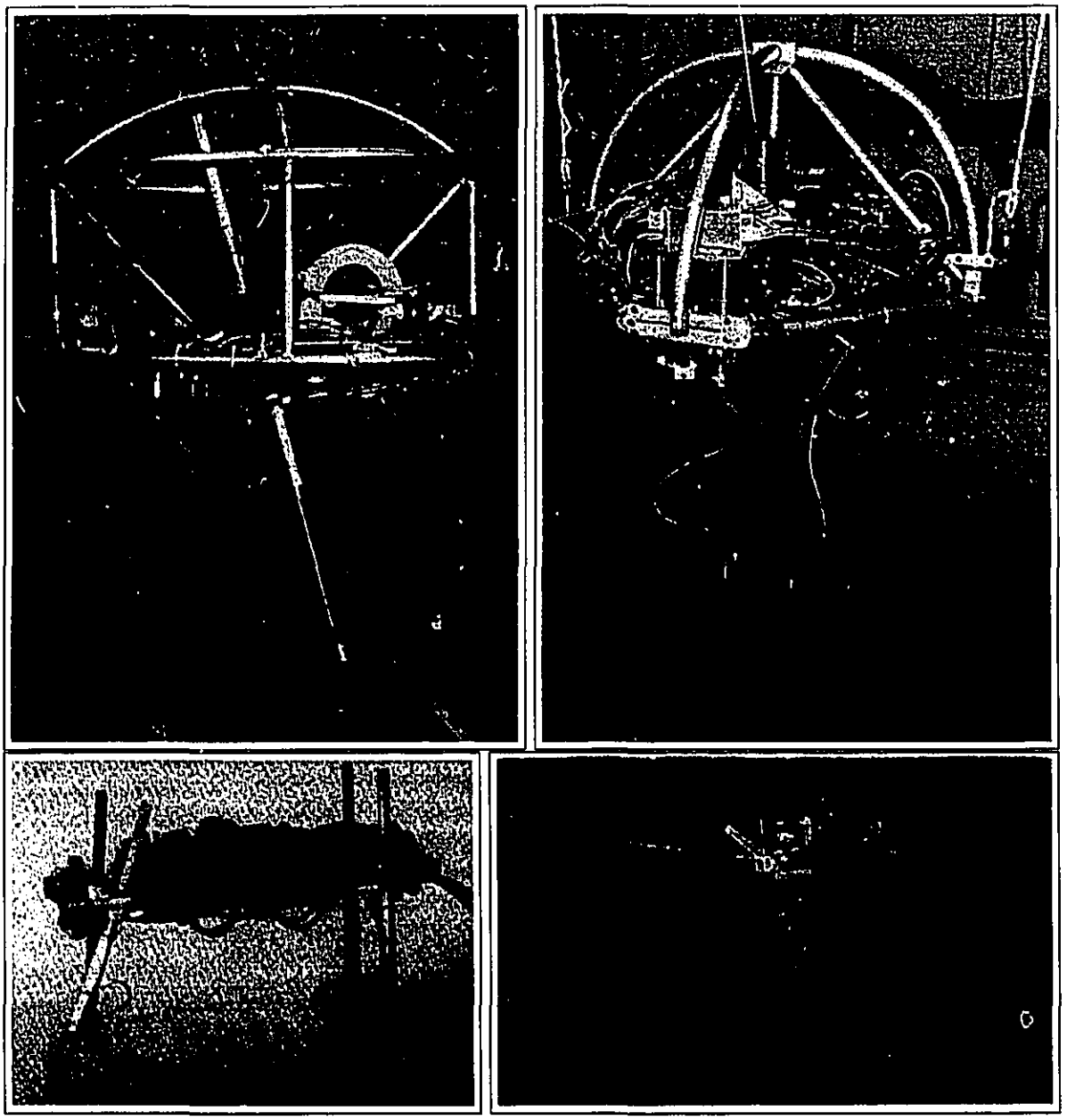

Figure 1.1: *M. H. Raibert's Legged Robots: 3D hopping machine, 1983 (top left); 3D bipedal machine, 1989 (top right); 3D quadruped, 1984 (bottom left); and planar kangaroo, 1990 (bottom right). Left photos taken from [35], and right photos provided by M. Buehler.*

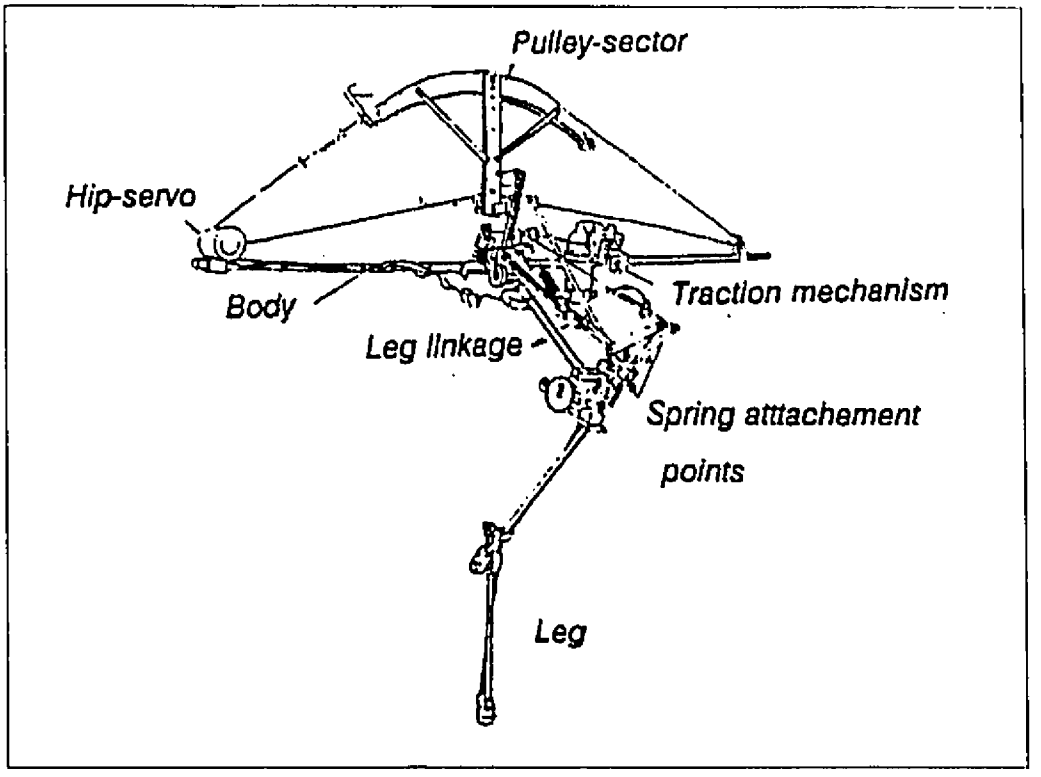

Figure 1.2: *K. V. Papantoniou's one-legged planar robot, 1991; taken from [31].*

1.4 Progress at McGill's ARL

Research on legged robots at McGill began in 1991 at the Ambulatory Robotics Laboratory (ARL) of McGill's Centre for Intelligent Machines (CIM). Work at ARL is directed toward understanding the theoretical and practical issues involved in legged locomotion with the goal of building a fully autonomous, four-legged robot capable of static and dynamic stable walking and running. Such a system will permit the study of the fundamental issues in multi-legged locomotion design and control. In addition, it will serve as a generic platform from which customized versions for particular applications will be derived.

ARL's current planar monopod [18], shown in Fig. 1.3, represents an important first step towards that goal. The process of mechanical design and controller development and implementation, as well as results gathered from experimental runs, have proven

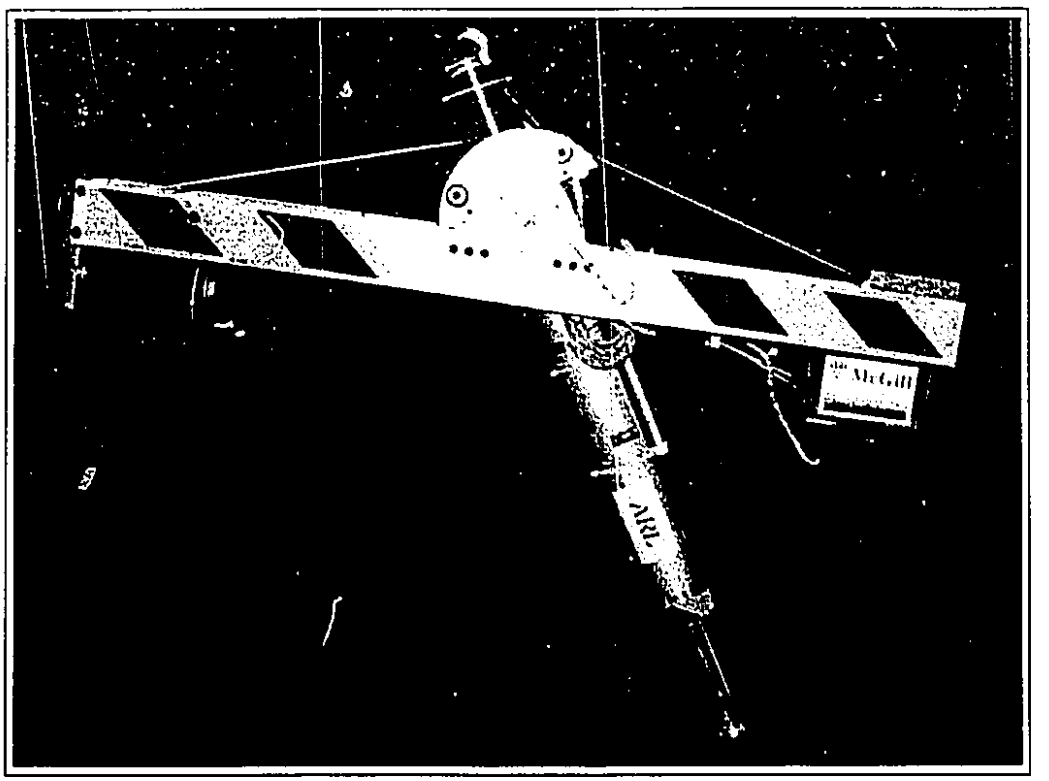

Figure 1.3: *The ARL Monopod, 1993; photo provided by P. Gregorio.*

invaluable to developing the next generation of legged robots. The planar monopod may seem simple and removed from practicality, however its simplicity allows for development of analytic results as well as providing conceptual insights, since it displays all the relevant properties of active balance and dynamic operation.

1.5 Problem Statement

ARL has selected a four-legged robot as a research platform to study the design and control of autonomous, dynamically stable legged creatures. Projected quadruped specifications are in line with those of a large dog and include a height and length of $0.75m$, a total mass of less than $50kg$ and a top running speed of $3m/s$. The initial goal, and the subject of this thesis, is to design and build a single prototype leg suitable for such a quadruped.

1.6 Author's Contributions

CARL Design and Construction

I designed a new Compliant Articulated Robot Leg[1] (CARL) which was constructed as a prototype for ARL's autonomous quadruped robot. The leg is a modular, self-contained unit with integrated amplifiers and control electronics. The design accommodates dynamic walking, trotting and bounding gaits, with an expected top speed of $3m/s$. It is an articulated 3 DOF design with revolute joints as opposed to prismatic joints for improved mobility, simplicity and low friction. It employs electric actuation instead of hydraulics for indoor power autonomy, improved modeling, control and reliability. While all previous compliant robot legs have used single springs for energy efficient locomotion and power autonomy [32, 34, 35], CARL is the first robot leg to have distributed compliance permitting the exploitation of passive limb motion in more than one degree of freedom.

ATLAS Design and Construction

To minimize leg mass, CARL features an AnTagonistic LADD Actuation System (ATLAS) which makes motor power available as high joint torques efficiently and at substantial weight savings compared to traditional transmissions. ATLAS features concentric LADD transmissions which due to their low mass and packaging show considerable promise for autonomous legged systems. Since these devices were not commercially available, I had to develop my own manufacturing technique as well as select LADD materials and system variables. The use of antagonistic LADDs required a variable radius pulley which maintains tension in the antagonistic LADDs in the presence of their kinematic nonlinearities. The thesis further describes two break-in phenomena that I identified for LADDs which are important for practical use and any kinematic modeling effort.

[1] Featured on national television [28].

(C)LADD Modeling

I introduce two new compliance models for LADD transmissions which reduce, by an order of magnitude, inelastic model errors of up to 18% full scale over force and position operating ranges. Elastic models introduced so far in the literature were all based on fiber elasticity, and show an increase in LADD length over the inelastic length with increasing force. I show that in experiments the opposite is true. The LADD is always shorter than predicted from the inelastic model. As the load force increases, the LADD length approaches the inelastic length. I found the cause for this fundamentally different elastic behavior to be fiber bending. I also employ one of the new models to improve the prediction of the kinematics of a concentric LADD. The new LADD models are essential for the design of LADD based systems, such as ATLAS, the online estimation of LADD forces, and accurate control.

1.7 Organization of the Thesis

The thesis is organized as follows. Chapter 2 discusses the design and construction of CARL while that of ATLAS is presented in Chapter 3. In Chapter 4, modeling of LADDs which form the basics to ATLAS is presented along with model validation through experimental work. Chapter 5 provides an interpretation of the findings along with proposed future work and design recommendations.

Chapter 2

CARL Design and Construction

A well-structured approach to the design of CARL assured its success. I applied the design process outlined in [29] which consists of task clarification, conceptual design and embodiment design. Task clarification (Sec. 2.1) involves the collection of information about the requirements and constraints in the leg design. In conceptual design (Sec. 2.2), major design decisions are made determining the layout and form of the leg. In embodiment design (Sec. 2.3), the details of the leg are presented and discussed. Finally, details of CARL's construction and cost are included for completeness in Sec. 2.4.

2.1 Task Clarification

CARL is a prototype compliant articulated robot leg for an autonomous quadruped capable of dynamic operation and active balance. It serves as a platform to evaluate new design and control ideas intended to improve dynamic legged robot performance.

Many existing legged robots use prismatic legs and do so with a great deal of success [35] but there are limitations and drawbacks. Prismatic legs lose a substancial amount of energy through sliding friction and have restricted dexterity due to limits on retractability. Articulated legs with revolute joints have less friction than prismatic

joints and allow for improved mobility and dexterity. Also, we expect to obtain higher running speeds and increased reliability through the simpler revolute joint designs.

To be most versatile, we require non-polluting operation in indoor and outdoor environments. Mainly for this reason, we decided on battery based electric actuation, instead of pneumatic or hydraulic systems [35]. The resulting clean, safe and quiet operation is also important since the quadruped could well be in frequent and close contact with people. While high battery energy densities today are still major challenges, we will be able to exploit battery improvements resulting from automotive electric vehicle developments. Furthermore, it is possible to achieve accurate models of the electrically actuated robot leg, similar to [34]. Such accurate models are critical for model based controllers, and are in general more difficult to obtain for hydraulic or pneumatic systems [10, 11, 23, 24].

Maxon 2260 motors feature an excellent peak torque to mass ratio of $1.4 Nm/kg$ and have been selected in previous work [18, 34]. For this reason, the current prototype leg is actuated by these motors powered by *Advanced Motion Controls 25A PWM* servo amplifiers. During development, an off-board power supply is used. The next design iteration will be completely autonomous incurring more weight savings with the use of *Inland 1200* series motors and full power autonomy with Ni-Cd batteries.

Leg compliance is vital for energy efficient locomotion and power autonomy since much of the cyclic limb motion and the body's vertical oscillation can be provided by the nearly passive oscillation of a body's spring–mass systems [35]. This principle is used extensively in most mammals during dynamic gaits, and it saves as much as 50% in energy expenditure during locomotion [8]. In animals, the tendons, muscles, cartilage and bones act as energy storing elements. While some robots have used single springs for this purpose in the past [32, 34, 35], we design CARL with distributed compliance permitting the exploitation of this principle in more than one degree of freedom.

Projected quadruped specifications are in line with those of a large dog and in-

clude a height and length of $0.75m$, and maximum width of $0.6m$. Leg positioning includes two fore and two rear legs symmetrical about the quadruped's sagittal plane. Each prototype leg is adaptable to the planarizer, currently used for the ARL Monopod [26], for initial testing prior to being included on the quadruped. The quadruped is expected to perform a number of gaits such as walking, trotting and bounding, therefore requiring forward and lateral movement. Expected top running speed of the quadruped is $3m/s$. In addition, the quadruped is expected to negotiate obstacles such as jumping across a ditch one and half times its length, and hurdling an object half its height.

Loading conditions on individual legs for limb and joint design come from a simulation of a planar two-legged robot developed by M. Ahmadi. The worst case loading scenario drops the planar model from a $1.5m$ height onto a single leg. The expected weight of the quadruped used in the simulation is $50kg$ ($40kg$ plus $10kg$ for on-board batteries) equally distributed over the four legs. Compliance is modeled through the revolute joints as torsional springs while the limbs and body are rigid.

The quadruped will have two levels of control. A high level control will be responsible for overall quadruped motion. This electronic hardware along with the power supply ($10kg$ batteries) and any guidance systems such as gyroscopes, vision or sonar will be located on the quadruped's body. Each leg will have its own integrated computer with custom I/O to read sensors, process the information, implement control algorithms, send signals out to the motors and communicate with the high level control. Power to each leg will be provided from the main supply on the quadruped's body.

Attention is paid to safety with joint movement limitations designed for all degrees of freedom to prevent damage to the leg and injury to the operator. In addition, a number of operational safety devices will be coded in the control software.

The current prototype is constructed from materials readily accessible to ARL. Final leg cost must be kept below $\$10,000$ in order to keep the quadruped within

$50,000. A ten month project line was established from the onset of design to final assembly: September 1993 to June 1994.

2.2 Conceptual Design

In this section we divide CARL's development into three subsystems: leg kinematics, actuation and compliance.

Leg Kinematics

Since the overall robot quadruped size and performance specifications are similar to those of a large dog, we choose to model CARL after the hind leg shown in Fig. 2.1. A drawing of the proposed quadruped along with a general leg description is given in Fig. 2.2. The leg has a total of 4 degrees of freedom with respect to the body. All three limbs: foot (metatarsal), lower limb (tibia) and upper limb (femur), have revolute motion on the same plane. The upper limb has an additional degree of freedom for lateral movement. We choose the ratio of the lengths of the femur, tibia and metatarsal to be the same of a dog: $1 : 1 : 0.4$ [9]. With a maximum quadruped height of $0.75m$, we set the upper and lower limbs to be of equal lengths of $0.30m$ and the foot of $0.12m$. In addition, the foot has a single contact point (toe) with the ground.

Actuation

Due to mass constraints of $8 - 9kg$ per leg, only three motors are made available to actuate the four joints. Both knee and hip fore-aft movement are provided through compliance in series with actuation, while ankle movement is solely compliant. The ankle is not actuated in order to keep the system simple, and to minimize leg mass, unsprung mass and inertia. The hip lateral motion is directly actuated without compliance since the energy stored in lateral motion is relatively small and not periodic. To keep leg inertia to a minimum for better leg performance, we locate the lateral

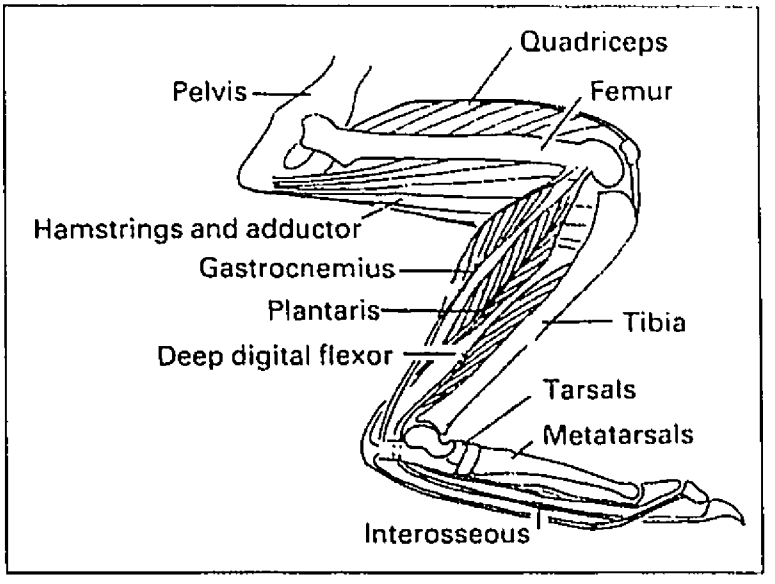

Figure 2.1: *The skeleton, and some of the principal muscles, of a hind leg of a typical mammal, taken from [6].*

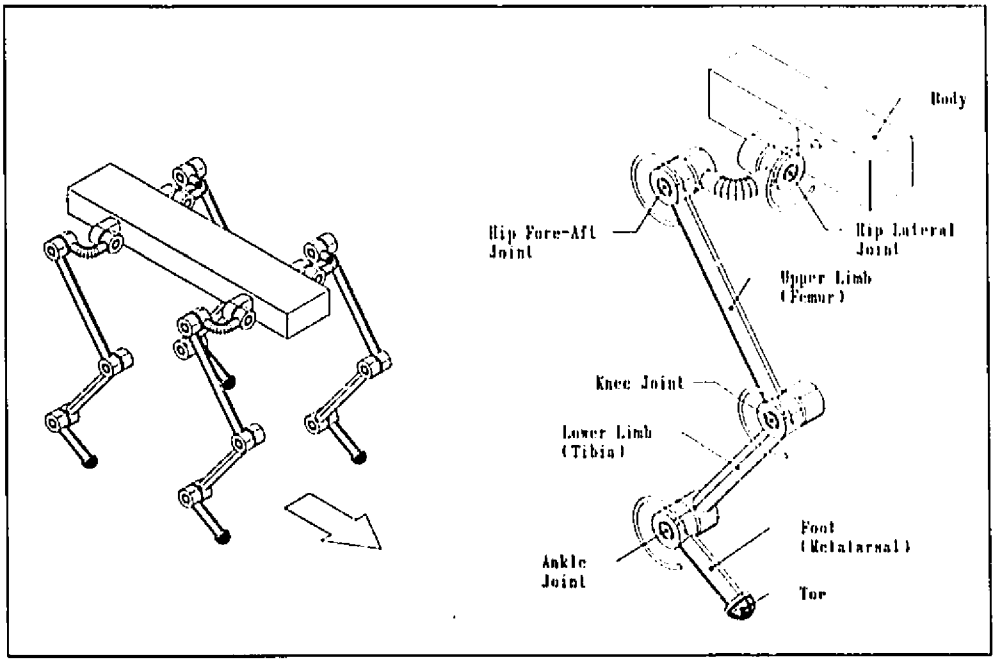

Figure 2.2: *A drawing of the proposed quadruped (left) and a general description of CARL (right).*

actuation motor on the body, and both knee and hip fore-aft motors clustered about the hip. We do so because each motor weighs a hefty $1.3kg$.

A key design challenge is exploiting fully the limited power density ($\approx 62W/kg$) of the *Maxon 2260* motor. The torque-speed curve specified by the manufacturer and our own experimental one is given in Fig. 2.3. We simulated a planar two-legged compliant robot (shown in Fig. 2.4) to obtain realistic torque-speed specifications. While the available power of the motor is adequate ($80W$), transmission ratios of $30 - 50$ are needed to provide the necessary joint torques. We found that this is difficult to achieve with traditional transmissions, while still remaining within the leg's weight constraints of between $8 - 9kg$ and maintaining low leg inertia. For this reason we decided to pursue a technology invented and pioneered by S. C. Jacobsen [19], based on fiber connected hoops, termed LADD transmissions. We develop ATLAS, a LADD based actuation package, suitable for the knee and hip fore-aft actuation of CARL.

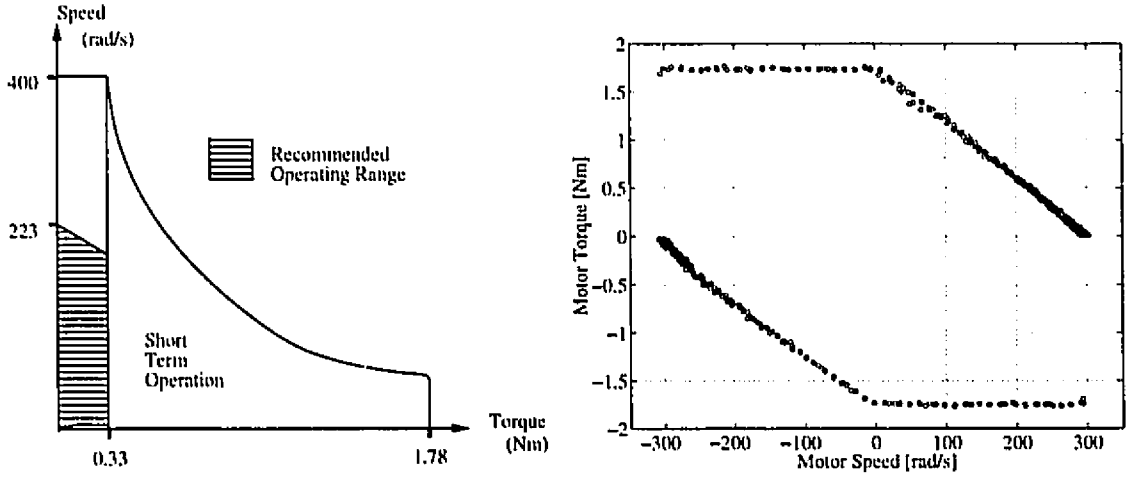

Figure 2.3: *Torque-speed curve of the Maxon 2260 brush 80W DC motor, adapted from [5] (left) and experimental torque-speed curve (right), taken from [18]. The torque is limited to* $1.8Nm$ *as specified by the manufacturer.*

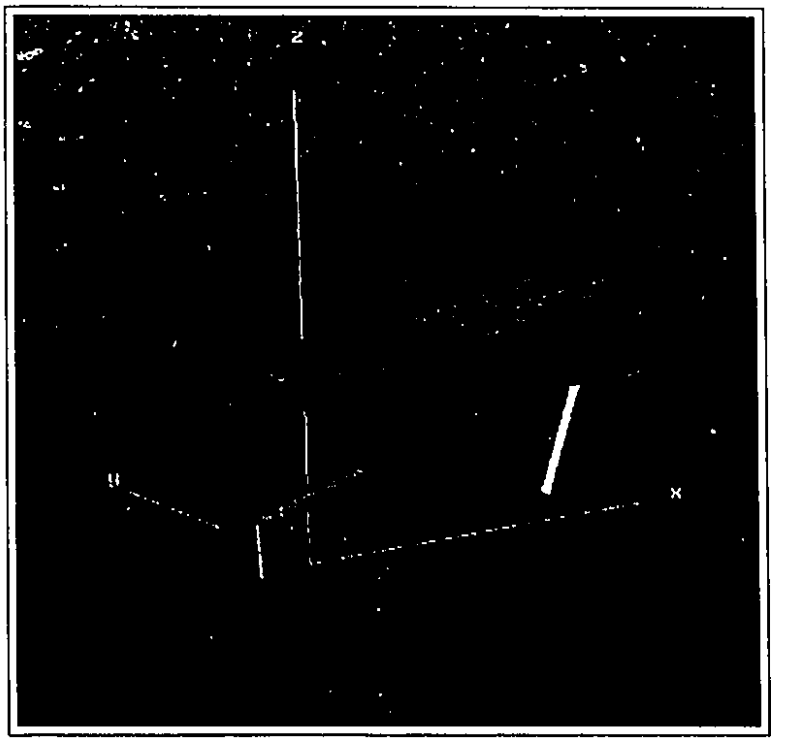

Figure 2.4: *Simulation of a planar two-legged compliant robot.*

Compliance

Projections obtained from simulations require approximately 30*J* of energy storage per compliant joint. By using elastomers, we are able to achieve an efficient compliant system compared to conventional steel-coil or leaf springs. The material's extremely high energy density (150 times that of steel, see Table 2.1) makes the design lightweight and compact. We accomplish this with a torsion disk which is a simple power transmission coupling that assumes a simple shear mode of deformation [14], illustrated in Fig. 2.5. This deformation mode is used extensively for rubber springs and corresponds well with the predicted linear stress-strain relationship up to approximately 80% strain.

Material	*Energy Density [J/kg]*
Grey Cast Iron	1.11
Extra-Soft Steel	9.18
Phosphor Bronze	12.2
Rolled Aluminum	22.6
Hardened and Tempered Spring Steel	284
Hickory Wood	365
Vulcanized Rubber	44,800

Table 2.1: *Energy densities of selected materials, taken from [14].*

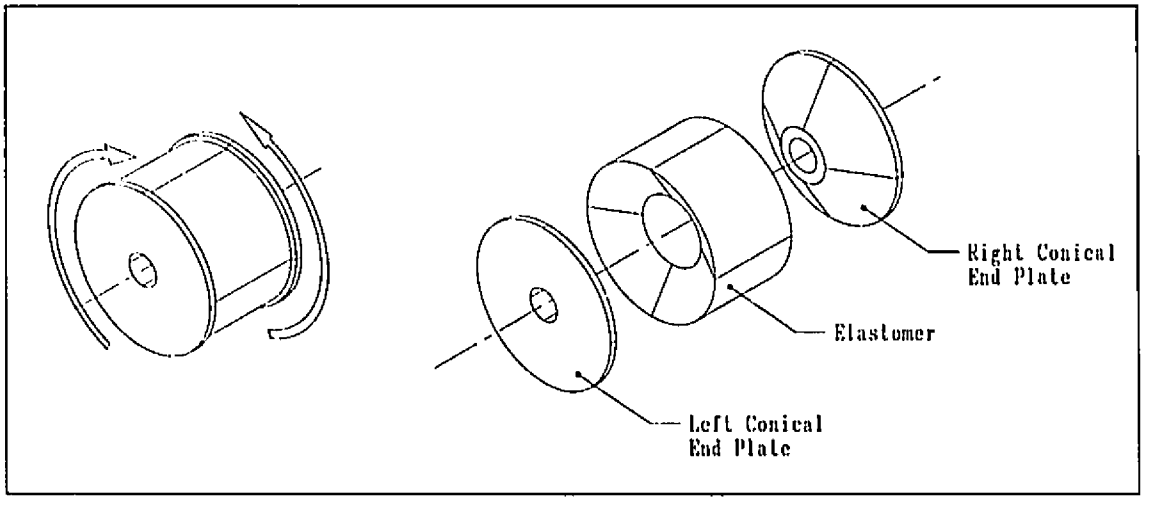

Figure 2.5: *Elastomeric torsional compliance: assembled (left) and labeled exploded view (right).*

2.3 Embodiment Design

Detail design work of CARL was accomplished with the assistance of graduate students P. Gregorio and M. Ahmadi, and undergraduate mechanical engineering students P. Grégoire, T. Marincic, and O. Payant. P. Gregorio inspired many of the ideas incorporated in the design of limbs and joints. T. Marincic and O. Payant worked on a thorough force analysis of CARL based on the planar two-legged robot simulation developed by M. Ahmadi [17]. P. Grégoire, along with P. Gregorio, carried out the detail design of the leg compliance. My responsibility was to supervise the group, gather their ideas, work on actuation and produce a functional leg. A total of seven months of design work was necessary to complete CARL. The sum of our efforts is shown in Fig. 2.6.

In this section, I review the designs of the leg's limbs, joints, lateral actuation and joint compliance. I end discussion on the leg design with details on the distribution of leg mass. Details of CARL knee and hip fore-aft actuation provided through ATLAS are presented in Chapter 3.

Limb Design

The limbs, shown in Fig. 2.7 (parts 34,43,55), were designed to be monolithic instead of an assembly of smaller parts. Although this was more complicated to manufacture, it proved to be a wise design choice that resulted in lighter and stronger limbs with fewer fasteners and machined parts. Aluminum was chosen for the limb material because of cost, machinability and availability.

The limbs were designed to be used for all legs of the quadruped with minimal machining differences. This was accomplished with symmetrical designs which required such things as similar joint limits. An I-beam cross section for the upper and lower limbs provides the best strength to weight ratio with no difficulties in manufacturing. To alleviate unnecessary effort in lateral actuation when the leg is in planar operation, the lower limb is offset. This positions the toe (part 53) under the action line of the

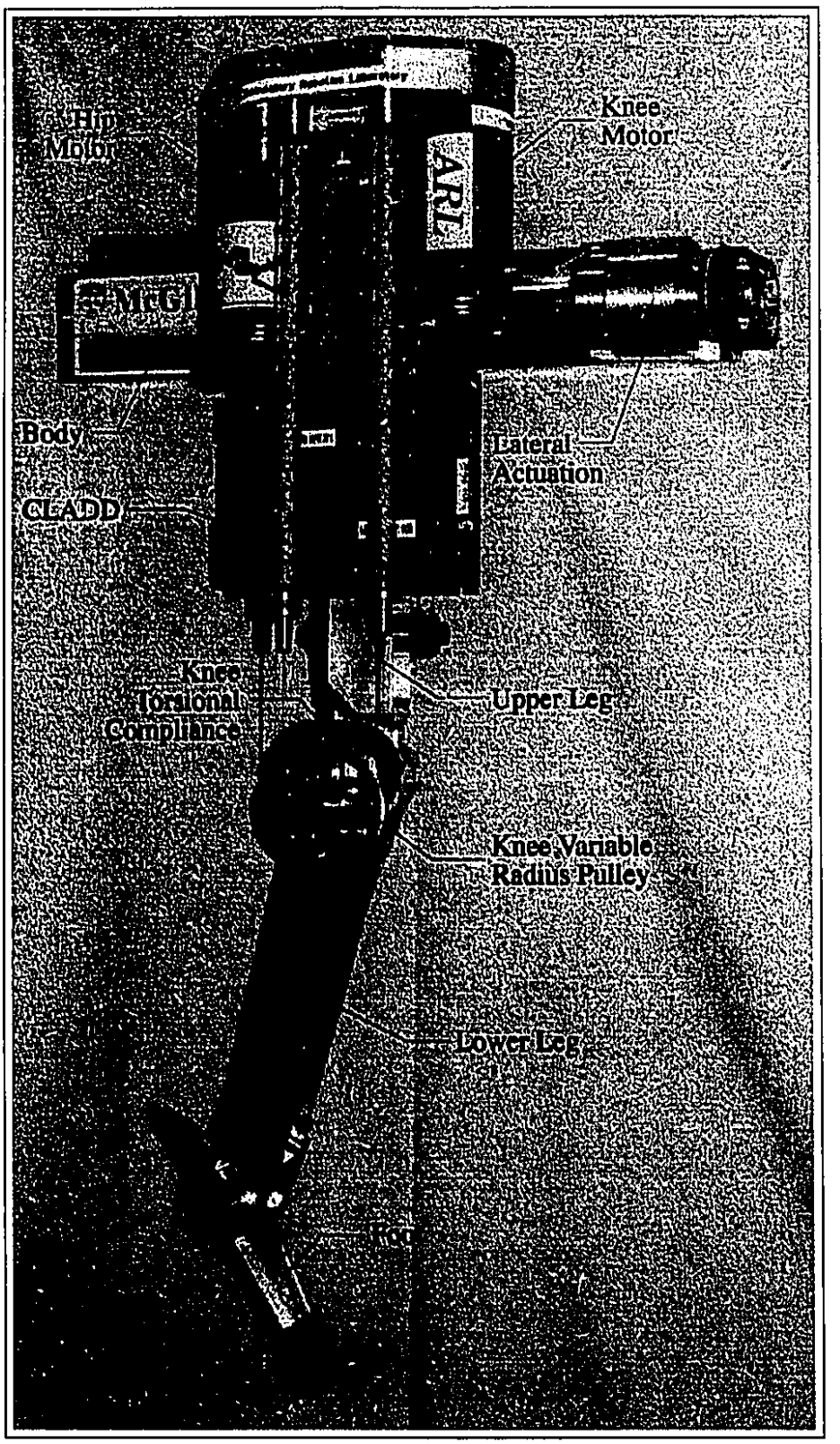

Figure 2.6: *CARL.*

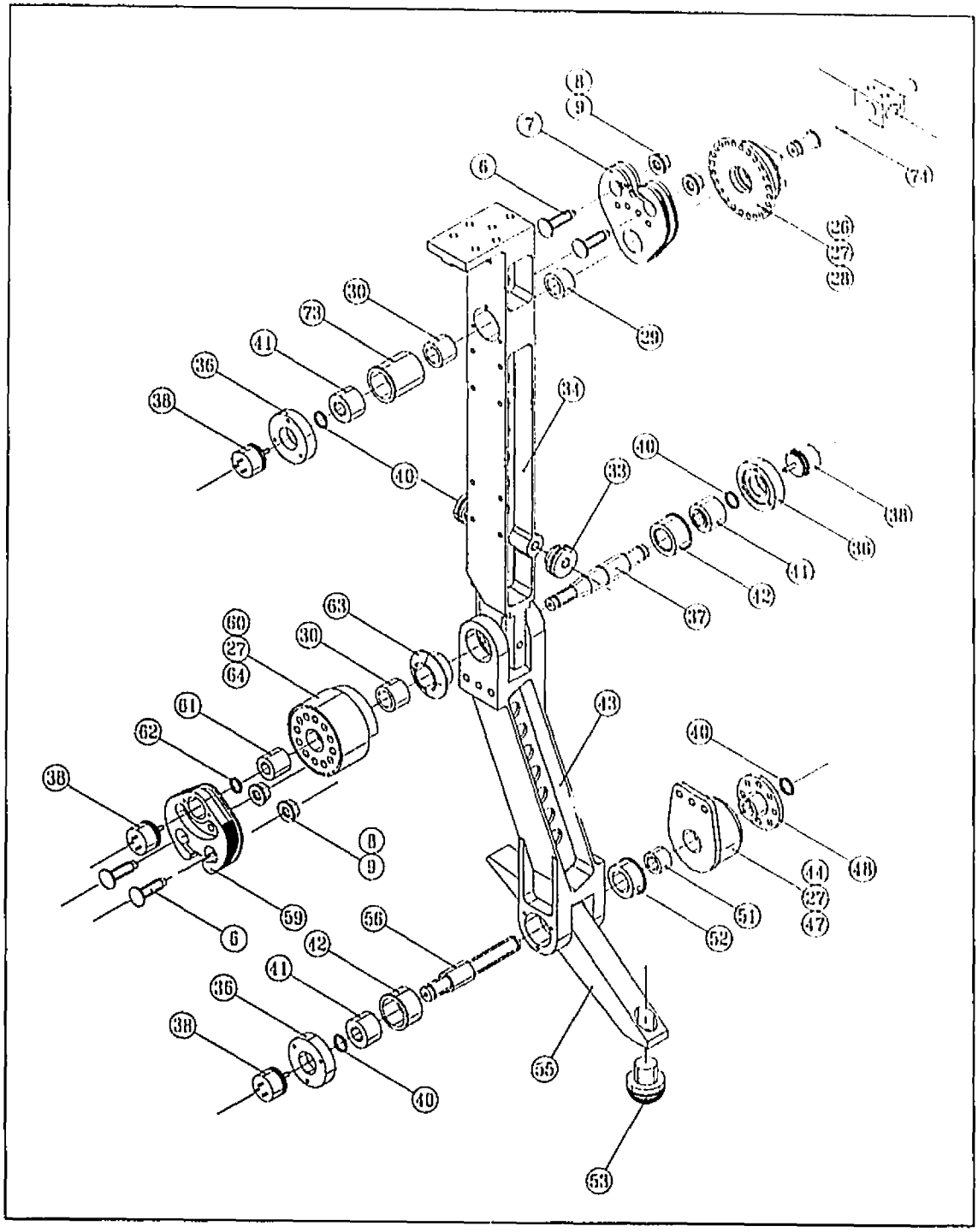

Figure 2.7: *CARL: Planar leg exploded view. Refer to Appendix B for CARL's list of parts. Fasteners and keyways are not shown.*

lateral actuation system eliminating any unnecessary energy expenditure.

The upper limb provides support for the ATLAS packages for both the knee and hip fore-aft actuation and respective motor servo amplifiers, while the lower limb provides support for knee and ankle compliance systems. The lower limb provides rotation limits of 100° for the ankle and 155° for the knee. Limits for lateral actuation are provided with hard stops located on the body. Lateral movement is set but not limited to 40° to the exterior and 5° to the interior. There are no physical limits for the hip fore-aft motion but rather the design allows unobstructed movement which serves to increase leg workspace.

Joint Design

Exploded view drawings of the ankle, knee and hip fore-aft joints are shown in Fig. 2.7 illustrating their similarities in design. All joints are supported in double shear and have *NKIB 5901* bearings (part 41) supporting both radial and axial loads. Needle roller bearings provide further radial support: *HK 1212* (part 51) for the ankle and *HK 1516* (part 30) for both the knee and hip. Joint shafts (parts 37,56,74) were manufactured from 4140 steel quenched and tempered at 205°*C*. The quenching and tempering provides the necessary shaft strength and a hard enough surface to eliminate the need for inner races for the needle roller bearings. Use of inner races would have required larger bearings which in turn would have increased limb size and mass.

Position sensing of all joints is accomplished with *CP-2FK Midori Green Pots* (part 38) fitted with local A/D circuitry designed by P. Gregorio [18]. These were chosen as opposed to incremental optical encoders because of compactness and the increase in sensor resolution available with the use of scaling circuitry.

Lateral Actuation

Details of CARL's lateral actuation are shown in Fig. 2.8. A harmonic drive (part 85)

provides transmission for this joint because of the space limitations. This design proves advantageous in that we can evaluate ATLAS' design and performance against a competitive transmission such as this one. We purchased a *CSF-20-160-2A-GR* harmonic drive from *HD Systems* with a torque ratio of 160 : 1, and specified for repeated and momentary peak torques of $92Nm$ and $147Nm$ respectively.

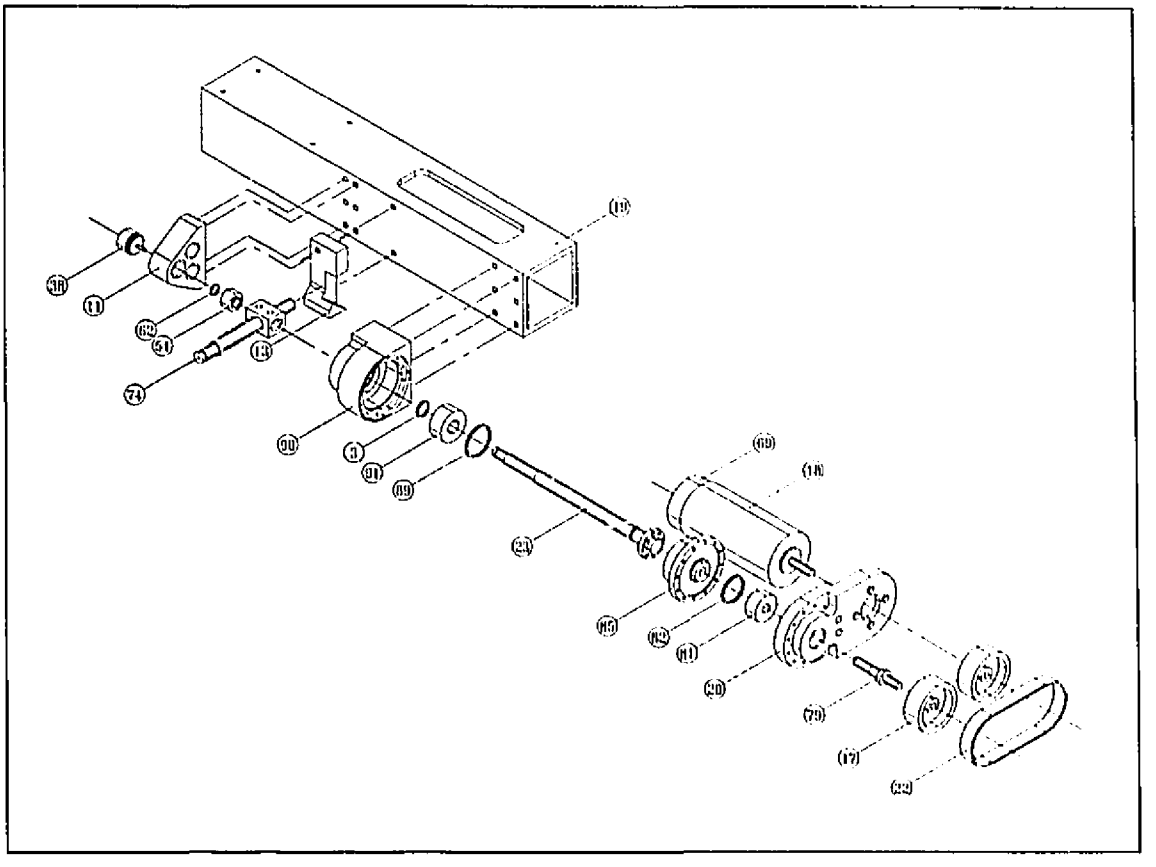

Figure 2.8: *CARL: Lateral actuation exploded view. Refer to Appendix B for CARL's list of parts. Fasteners and keyways are not shown.*

The lateral joint is supported by a *HK 1412* needle roller bearing (part 54) at one end and a *3202 ZZ* double row angular contact ball bearing (part 81) on the other end which in addition provides output support for the harmonic drive. To keep the overall length of the lateral actuation to a minimum, the use of a timing belt and pulleys (parts 17,22) arrange the motor (part 18) in parallel with the harmonic drive.

This also positions the motor in a protective area where it is safe from impacts.

Compliance

The work on compliance design was carried out by P. Grégoire and P. Gregorio. Since it is an integral part of the leg, it is briefly mentioned here while complete details of the work can be found in [16]. Two elastomers, polyurethane and natural rubber, were pursued to provide joint compliance. The torsional knee compliance shown in Fig. 2.9 is composed of a cylindrical shaped elastomer cast between two conical aluminum disks. Since the elastomer is bonded directly onto the aluminum disks, no mechanical fasteners are required. The conical disk shape allows uniform strain of the material and thus optimal material exploitation. In our application, the torsional springs do not sustain more than 75% strain in the worst case situation.

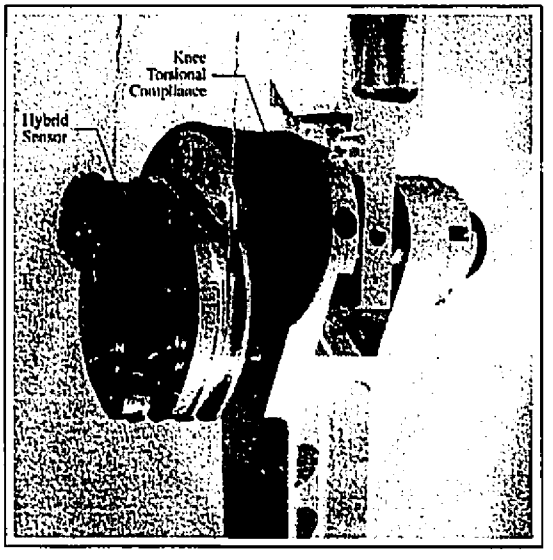

Figure 2.9: *Torsional Knee Compliance.*

Design advantages include a lightweight package: the spring at the knee weighs only $125g$ including compliance and end plates. Moreover, we have measured very low damping coefficients, $\zeta < 0.05$, which permits efficient energy recovery. One device is located at the fore-aft hip (parts 26,27,28), knee (parts 60,27,64) and ankle (parts 44,27,47), as shown in Fig. 2.7. Each compliance is customized in terms of

range and stiffness.

Leg Mass Distribution

Design work focused extensively on minimizing leg mass. A complete list of parts, and respective masses, is included in Appendix B. The leg's total mass without the temporary body is $11.7kg$. Although this is above the required leg specification of $8-9kg$, I include in Appendix D proposed mass reductions totalling $3.8kg$ for future design work.

The current mass includes all items necessary for a fully functional leg, except for the power supply which will be located on the main body. The total planar leg weighs $8.3kg$ while the lateral actuation adds $3.4kg$ to the total, an increase of 43% in leg mass. Limbs, bearings and fasteners account for $1.3kg$ (11.4%), $0.5kg$ (4.4%) and $0.4kg$ (3.5%), respectively. Motors and electronics account for $5.4kg$ (47.4%). The three actuation packages: knee, hip and lateral, without motors, account for $0.9kg$ (7.9%), $1.0kg$ (8.8%) and $1.2kg$ (10.5%) of the total mass.

2.4 Construction and Cost

Construction of CARL began in the early days of March 1994 and was completed by mid June 1994. A complete leg cost including parts and labour is given in Appendix C. Material costs were kept to a minimum by purchasing in bulk for future leg construction and plundering other labs. Machining costs, in order of $\$9,000$, will expect to come down considerably for the construction of multiple legs.

Chapter 3

ATLAS Design and Construction

CARL is the first robot leg to utilize LADD transmissions with the purpose of making motor power available as high joint torques efficiently and at substantial weight savings compared to traditional transmissions. ATLAS, an AnTagonistic LADD Actuation System, illustrated in Fig. 3.1, is an actuator system where a single electric motor drives an antagonistic pair of concentric LADDs over a variable radius pulley, not unlike two muscles actuating a joint.

Sec. 3.1 describes the modeling and construction of the concentric LADDs. The design of the variable radius pulley, which maintains tension in the antagonistic LADDs despite their kinematic nonlinearities, is detailed in Sec. 3.2. Finally, Sec. 3.3 describes the integration of concentric LADDs, variable radius pulley and transmission housing into the ATLAS package, and offers a comparison with conventional transmissions.

3.1 Concentric LADD (CLADD)

3.1.1 (C)LADD Background

LADD stands for Linear-to-Angular Displacement Device, and it is a transmission element converting rotational to translational motion, invented and pioneered by S. C. Jacobsen [19]. It is described as a favorable alternative to gear trains, har-

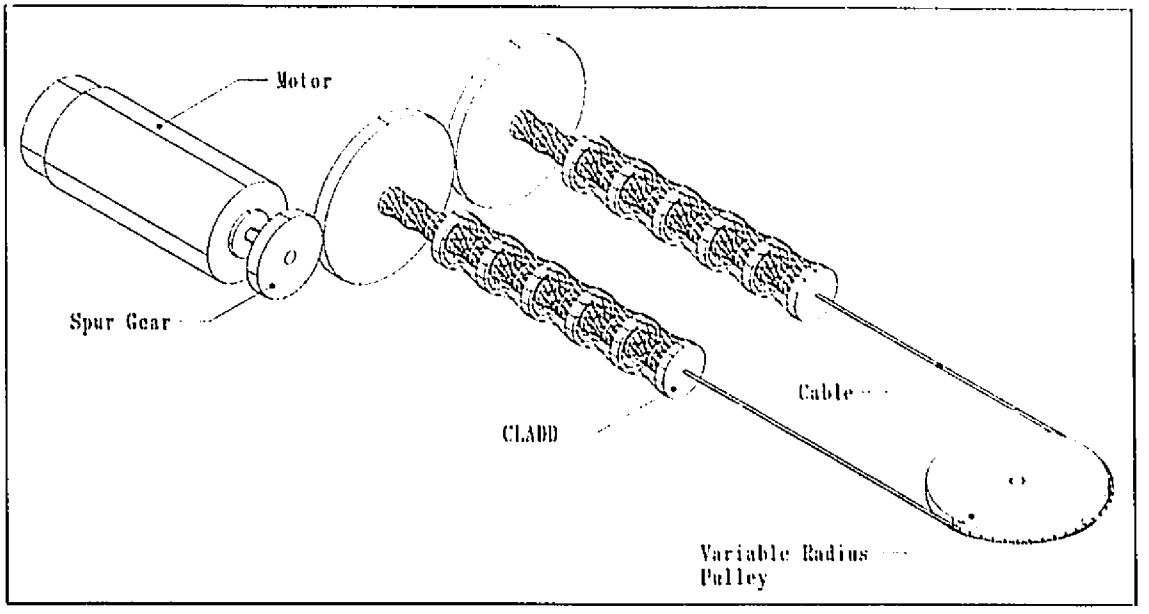

Figure 3.1: *ATLAS description.*

monic drives, ball screws or belt and pulley systems rated according to criteria such as weight, cost, noise, efficiency, life, dynamic performance and strength [20].

A LADD is composed of a number of single LADD cells fixed end to end. Each cell consists of two rings joined by high strength fibers, as shown in Fig. 3.2. The behavior of this single cell describes the LADD's basic operating characteristics: As the cell is twisted, the distance between the rings decreases, thus rotary motion is translated into linear motion. Conversely, if a twisted cell is subjected to linear extension it will unwind, producing a rotary motion. In a LADD based system, a stationary motor rotates one end of the LADD while the other end translates.

Jacobsen conducted a number of tests to establish LADD performance [22]. A $14.3mm$ diameter LADD fabricated of *Kevlar*® supported in excess of $385kg$ with zero input rotation. When the LADD was contracted approximately 20%, its ultimate strength was about $200kg$. A typical test LADD was $203mm$ long, produced an excursion of about $50mm$, and weighed less than $6g$. Fatigue tests have been conducted on a similar sample. The LADD performed in excess of 6,000,000 cycles pulling a $22.7kg$ load through a $50mm$ excursion at a rate of three cycles per second.

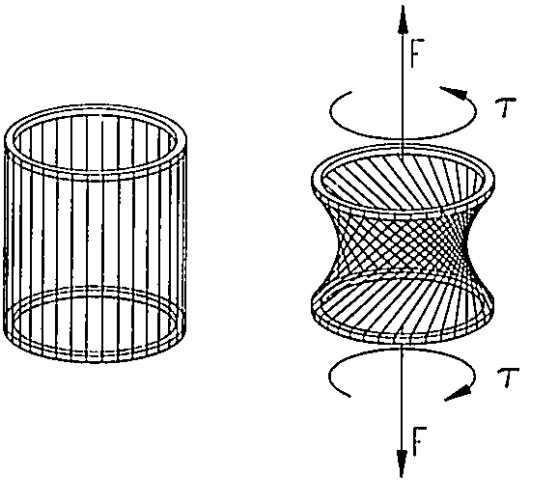

Figure 3.2: *Single LADD cell statics. Fully extended (left), and contracted under a load F maintained by a torque τ (right).*

A Concentric LADD (CLADD), shown in Fig. 3.3, is composed of two sizes of LADDs nested coaxially inside one another and possesses some advantages over the simple LADD. In a CLADD based system, a stationary motor drives (rotates) one end of the inner LADD while the remaining end is rigidly connected to one end of the outer LADD. At this connection point the external load is applied, and both inner and outer LADDs rotate and translate together. The remaining end of the outer LADD is fixed (no rotation or translation) at a position close to the motor.

One of the advantages of a CLADD over the single LADD chain is the removal of the slider mechanism (no-rotation constraint) at the load end which is necessary in LADDs to maintain the torque differential across the cells. This reduces both weight and complexity. With the CLADD, the reaction torque of the LADD cells occurs near the motor where the torque was initially generated. Now the load end of the CLADD must be permitted to rotate freely which can be accommodated by a cable.

Besides eliminating the need for a linear motion guide, a CLADD configuration will increase a single LADD's effective length without physically doing so. The addition of cells allows the CLADD to operate at a higher mechanical advantage over a longer excursion than a single LADD chain with the same physical length. Also, the load

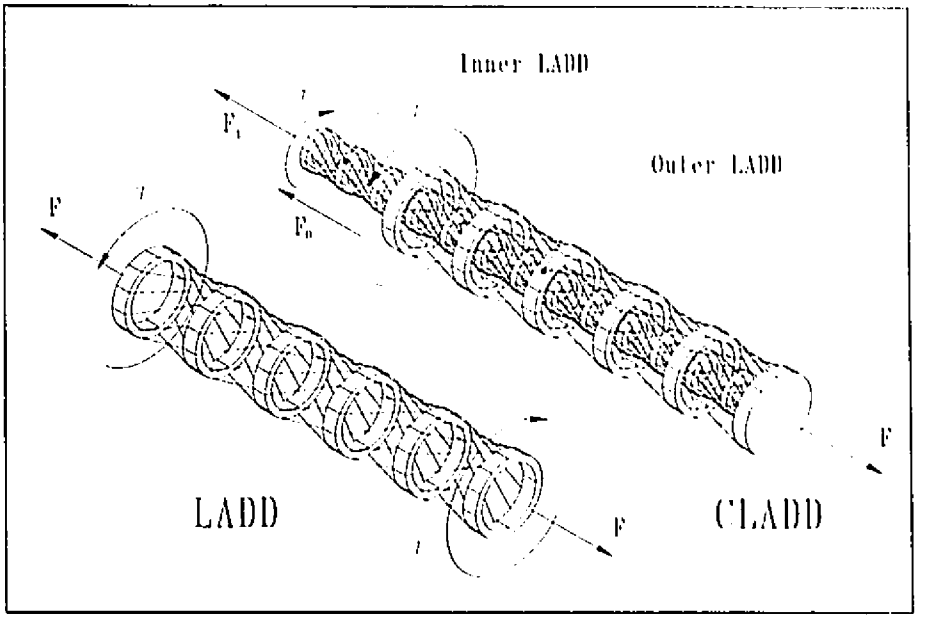

Figure 3.3: *LADD and CLADD statics.*

applied to the CLADD is distributed over both the inner and outer LADDs, thus each LADD carrying a fraction of the load, increases the CLADD's load carrying capabilities.

Jacobsen details LADD's use in two prosthetic devices: the *Utah Arm*, where elbow flexion was actuated by LADDs, and in another configuration where LADD had been used to actuate prehension in an orthotic hand splint [22]. The implementation of LADD in the elbow flexion of the *Utah Arm* includes two CLADDs driven in antagonism by one motor source around a variable radius pulley. This configuration provided quiet operation (42 to 53dB) and a torque ratio of 27 : 1 [21].

In [12], J. C. Carruth describes the design challenges associated with LADD. Physical limits of LADD operation and trade-offs between geometry of the transmission and as well as kinematics, statics, operational instability, interfiber interference and knotting, are presented.

3.1.2 Inelastic (C)LADD Models

LADD Model

The inelastic LADD model taken from [20, 22] relating LADD length l to input rotation θ is readily derived from its geometry, depicted in Fig. 3.4. The cell links are assumed to remain straight and of constant length L during cell rotation.

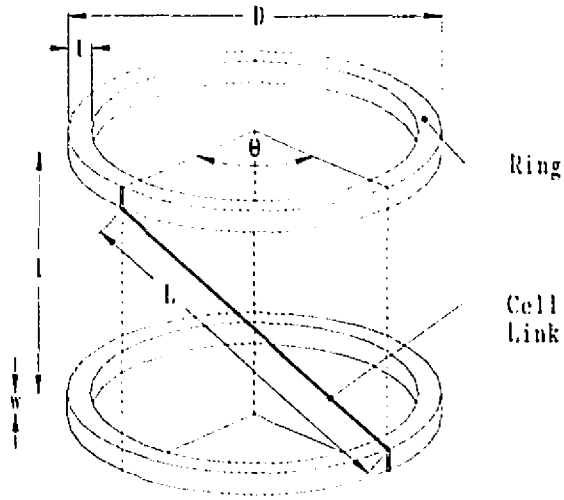

Figure 3.4: *Inelastic LADD model cell geometry taken from [20, 22]. This model assumes that cell links remain straight and of constant length L during cell rotation.*

Keeping the lower ring fixed and rotating the upper ring by θ, the upper link ends displace by $Dsin\left(\frac{\theta}{2}\right)$. With $L^2 = l^2 + D^2 sin^2\left(\frac{\theta}{2}\right)$, and solving for the cell length l, we get

$$l(\theta) = D\sqrt{\mu^2 - sin^2\left(\frac{\theta}{2}\right)}$$

where $\mu \stackrel{\text{def}}{=} L/D$ is the cell's aspect ratio. A chain of n cells will equally divide the input rotation θ, giving the n-cell LADD kinematics as

$$l(\theta) = nD\sqrt{\mu^2 - sin^2\left(\frac{\theta}{2n}\right)} \tag{3.1}$$

and where the contraction from full extension is

$$\Delta l(\theta) = nD\sqrt{\mu^2 - sin^2\left(\frac{\theta}{2n}\right)} - nL. \tag{3.2}$$

Referring to Figures 3.2 and 3.4, the transmission ratio or lead $r(\theta)$ of a LADD can be derived from the principle of virtual work, $dW = Fdl + \tau d\theta = 0$, and the derivative of (3.1) $dl/d\theta$ as

$$r(\theta) \stackrel{\text{def}}{=} \frac{\tau}{F} = -\frac{dl}{d\theta} = \frac{Dsin\left(\frac{\theta}{n}\right)}{4\sqrt{\mu^2 - sin^2\left(\frac{\theta}{2n}\right)}}. \tag{3.3}$$

Rearranging (3.3), a non-dimensional mechanical advantage for LADD $m(\theta)$ is given as

$$m(\theta) = \frac{FD}{\tau} = -\frac{d\theta}{dl}D = \frac{4\sqrt{\mu^2 - sin^2\left(\frac{\theta}{2n}\right)}}{sin\left(\frac{\theta}{n}\right)}. \tag{3.4}$$

Limits on LADD operation include InterFiber Interference (IFI) which occurs when a LADD cell is rotated to a point where the cell links begin bending around and rolling over each other. This rubbing makes modeling difficult and causes wear on the fibers. This region of operation is avoided, and places an upper limit on the LADD input rotation θ. Carruth [12] derives an expression for IFI,

$$\frac{d}{D} = \frac{\sin\left(\frac{\alpha}{2}\right)\cos\left(\frac{\theta_{IFI}}{2n}\right)}{\sqrt{1 + \frac{\sin^2\left(\frac{\theta_{IFI}}{2n}\right)\cos^2\left(\frac{\alpha}{2}\right)}{\mu^2 - \sin^2\left(\frac{\theta_{IFI}}{2n}\right)}}} \tag{3.5}$$

where $\alpha = 4\pi/c$ assuming the cell links to be equally spaced about the circumference of a ring, and c and d are the number and diameter of LADD cell links respectively. The maximum allowable IFI input rotation θ_{IFI} can be obtained numerically.

However, the more important limit on operation is LADD knotting [12]. As the name implies, the string of LADD cells begins to wrap up on itself as it is rotated

beyond a limit set by θ_{knot}. Observations of an over-rotated LADD (see Fig. 3.5) indicate that the axis of each cell shifts off center into a helical pattern.

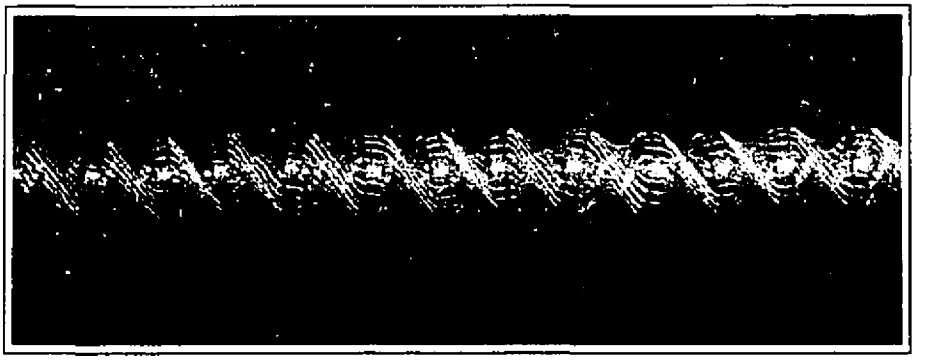

Figure 3.5: *LADD knotting.*

This knotting phenomena, or instability, occurs at rotations before IFI, $0 < \theta_{knot} < \theta_{IFI}$, and is thus the dominant limit. Knotting occurs in strings of LADD cells, and θ_{knot} is a function of the number of cells n. In contrast, IFI is a physical cell limit, independent of the number of cells. While IFI is predictable by (3.5), knotting is difficult to model and predict. It might occur from imperfections in LADD manufacturing due to slight variations in link to ring end conditions and the spacing of links around the circumference of cell rings. When a LADD is excessively rotated under a load, the variations are amplified and the LADD shifts to this helical pattern to redistribute the load.

To review the inelastic LADD model, the cell length l is non-dimensionalized as

$$\frac{l(\theta)}{L} = n\sqrt{1 - \frac{1}{\mu^2}sin^2\left(\frac{\theta}{2n}\right)}. \tag{3.6}$$

Fig. 3.6 shows a plot of (3.6), for a single LADD cell, $n = 1$, with a cell aspect ratio of $\mu = 1$. The variable rate of contraction depends on the rotational position of the cell. This is an important property which contributes greatly to the design flexibility of LADD. In addition, the plot illustrates IFI given by (3.5) occurring at 140° for $c = 24$, $d = 0.5mm$ and $D = 16.0mm$.

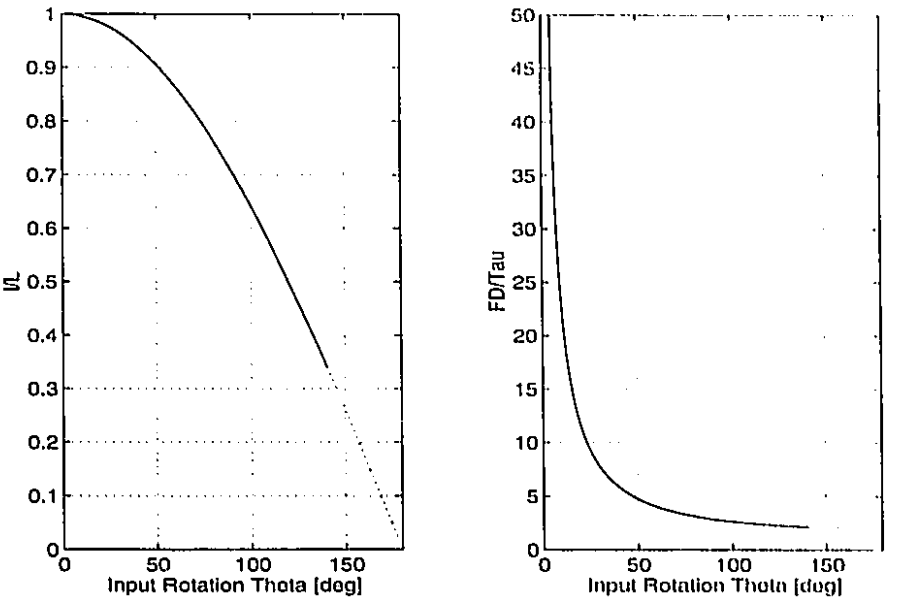

Figure 3.6: *LADD cell kinematics (left) and statics (right) with IFI (dotted curve) given by (3.5) occurring at* 140^o *for* $n = 1$, $\mu = 1$, $c = 24$, $d = 0.5mm$ *and* $D = 16.0mm$.

Since the rate of deflection for a LADD cell is variable, the mechanical advantage $m(\theta)$ given by (3.4), also exhibits position dependent characteristics, as shown in Fig. 3.6. An initial small contraction given by a small rotational input, results in a high mechanical advantage. Increasing the number of cells n allows LADD to operate at a higher mechanical advantage over a longer excursion. A chain of LADD cells divides the linear contraction among the cells while each cell incurs the same force and torque. Each LADD cell therefore operates in a region of higher mechanical advantage than if there were fewer cells in the chain.

In discussing operating characteristics of LADD, it is worth noting that changing the cell aspect ratio μ will produce different rates of contraction and correspondingly different mechanical advantages for equal rotational input (see Fig. 3.7). Up to this point only LADDs with an aspect ratio of 1 have been considered and for most applications an aspect ratio of less than or equal to one provides the optimum transmission [22].

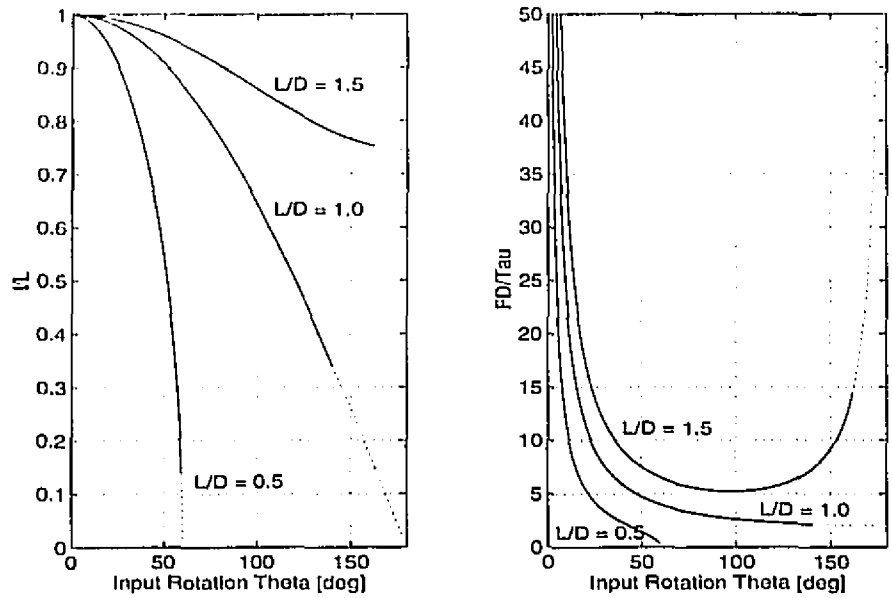

Figure 3.7: *LADD cell kinematics and statics for different aspect ratios μ. The dotted curve refers to IFI given by (3.5) for $n = 1$, $\mu = 1$, $c = 24$, $d = 0.5mm$ and $D = 16.0mm$.*

One advantage of LADD operation is that its nonlinear transmission (kinematics) complements the characteristics of typical DC motors (see Fig. 2.3) used for their actuation. At a high mechanical advantage, LADD has a slow contraction rate. Since the actuating motor need to only provide a low torque at this operating point, a lot of motor speed is available to offset LADD's slow response. At a low mechanical advantage, LADD has a high contraction rate. Again, the motor provides a high torque at the expense of motor speed which is not required.

CLADD Model

In CLADD design, the co-axial positioning of the inner LADD with respect to the outer requires that both LADDs contract by the same amount. Their lengths are given by (3.1) as

$$l_i(\theta_i) = n_i D_i \sqrt{\mu_i^2 - sin^2\left(\frac{\theta_i}{2n_i}\right)} \quad \text{and} \quad l_o(\theta_o) = n_o D_o \sqrt{\mu_o^2 - sin^2\left(\frac{\theta_o}{2n_o}\right)},$$

where subscripts i and o denote the inner and outer LADDs respectively. With each LADD made of equal length, the full length of both LADDs and thus the CLADD is l^o, where

$$l^o = l_i^o = n_i D_i = l_o^o = n_o D_o. \tag{3.7}$$

Further simplification is introduced by giving both LADDs an aspect ratio of unity,

$$\mu_i = \frac{L_i}{D_i} = \mu_o = \frac{L_o}{D_o} = 1. \tag{3.8}$$

Using (3.7) and (3.8), the individual LADD models simplify to

$$l_i(\theta_i) = l^o \cos\left(\frac{\theta_i}{2n_i}\right) \quad \text{and} \quad l_o(\theta_o) = l^o \cos\left(\frac{\theta_o}{2n_o}\right). \tag{3.9}$$

Since both LADDs are in parallel, the contraction lengths of the inner and outer LADDs are identical,

$$l^o(\cos\left(\frac{\theta_i}{2n_i}\right) - 1) = l^o(\cos\left(\frac{\theta_o}{2n_o}\right) - 1)$$

and therefore

$$\frac{\theta_i}{n_i} = \frac{\theta_o}{n_o}. \tag{3.10}$$

The total input rotation θ of the driving source, the motor, is shared by both LADDs, $\theta = \theta_i + \theta_o$. Substituting into equation (3.10), we get

$$\theta_i = \frac{\theta n_i}{n_i + n_o} \quad \text{and} \quad \theta_o = \frac{\theta n_o}{n_i + n_o}. \tag{3.11}$$

Now, from (3.9) and (3.11) the CLADD model is

$$l(\theta) = l^o \cos\left(\frac{\theta}{2(n_i + n_o)}\right) \tag{3.12}$$

and the change in length from full extension is

$$\Delta l(\theta) = l^o(\cos\left(\frac{\theta}{2(n_i+n_o)}\right) - 1). \tag{3.13}$$

As with a LADD, the lead $r(\theta)$ for a CLADD can be derived from the principle of virtual work, $dW = Fdl + \tau d\theta = 0$, and the derivative of (3.12) $dl/d\theta$ as

$$r(\theta) \stackrel{\text{def}}{=} \frac{\tau}{F} = -\frac{dl}{d\theta} = \frac{l^o}{2(n_i+n_o)} sin\left(\frac{\theta}{2(n_i+n_o)}\right). \tag{3.14}$$

Rearranging (3.14), the non-dimensional mechanical advantage for CLADD is given as

$$\frac{FD_i}{\tau} = \frac{2(n_i+n_o)}{n_i sin\left(\frac{\theta}{2(n_i+n_o)}\right)} \quad \text{or} \quad \frac{FD_o}{\tau} = \frac{2(n_i+n_o)}{n_o sin\left(\frac{\theta}{2(n_i+n_o)}\right)}.$$

The load distribution over the two LADDs is solved as

$$F_i = \frac{2\tau}{D_i \sin\left(\frac{\theta}{2(n_i+n_o)}\right)} \quad \text{and} \quad F_o = \frac{2\tau}{D_o \sin\left(\frac{\theta}{2(n_i+n_o)}\right)},$$

where $F_i + F_o = F$. An advantage to CLADD is that the total load F is shared by both the inside and outside LADDs. Therefore, the smaller inside LADD can be designed with fewer fibers, and the inner cells can rotate to larger angles increasing the CLADD range of operation.

In addition to the operational limits on LADDs imposed by IFI and knotting, the range of motion of a CLADD is also limited by the outer LADD necking down and pinching the inner LADD as shown in Fig. 3.8. As rotation increases, the fibers of the outer LADD collapse on the inner LADD and necking occurs when

$$D = D_i + \frac{d}{2} = (D_o - \frac{d}{2}) \cos\left(\frac{\theta_{neck}}{2(n_i+n_o)}\right).$$

The maximum motor input θ_{neck} is given as

$$\theta_{neck} = 2(n_i+n_o) \arccos\left(\frac{D_i + \frac{d}{2}}{D_o - \frac{d}{2}}\right). \tag{3.15}$$

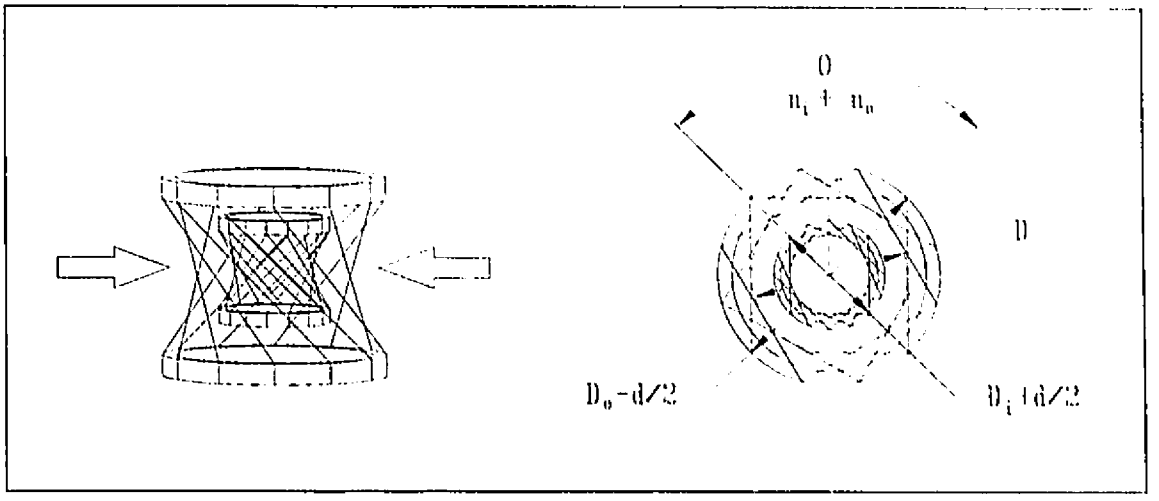

Figure 3.8: *Outer LADD necking down on inner LADD (left) and end view of CLADD with geometry to (3.15) (right).*

3.1.3 CLADD Detail Design

Our CLADD design supports working loads in the excess of $100kg$ over the full operating range. The design, shown in Fig. 3.9, allows for both inner and outer LADDs to be manufactured separately and for co-axial assembly with threaded end pieces. This allows separate inner and outer LADD model validation, and easy replacement of either one.

A general purpose epoxy structural adhesive, *CIBA-GEIGY Araldite*®, bonds the flexible links to the rings and end pieces. Sec. 3.1.4 details the epoxy application. Each end piece is manufactured with 24 equally spaced holes to support the links during manufacturing. The rings are manufactured from aluminum and end pieces from stainless steel.

Requirements for a suitable link material included: high strength, good bonding, low creep and high durability. Two materials, *Kevlar*® and *Spectra*®, were considered but neither satisfied all the criteria. *Kevlar*®, an aramid fiber, which was used by Jacobsen [22] exhibits good bonding, low creep and high strength properties, however it lacks durability which is critical for manufacturing and use. *Spectra*®,

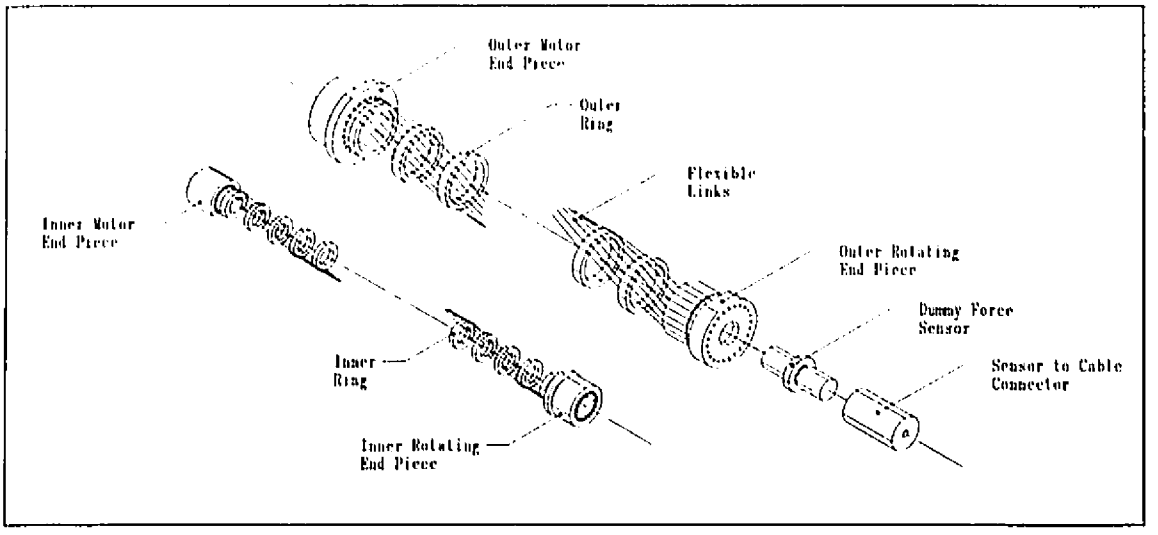

Figure 3.9: *CLADD detail design.*

a polyethylene fiber, is high strength, resilient and exhibits acceptable bonding, but creeps. The results to our creep tests on *Kevlar*® 18.2kg and *Spectra*® 22.7kg lines are presented in Fig. 3.10. Samples, 940mm in length, were loaded with a 5kg static load over a 12 hour period.

Kevlar® demonstrated excellent creep properties of 1.17mm (0.12%) and remained steady for a 2 hour period. However, *Spectra*® crept 7.22mm (0.77%) and exhibited non-vanishing creep properties of 1.13mm/hr (0.12%/hr). It was a difficult decision, but we chose *Spectra*® because of its superior resilience. Further, the low loading of each link during ATLAS operation, approximately 10% of the break strength, suggested creep may not become a problem.

Tests were carried out to determine the bonding limits of the epoxy on the *Spectra*® line for a contracted LADD cell. Single *Spectra*® samples bonded to aluminum fixtures with *Araldite*®, simulating LADD operation at 90° cell rotation, supported 5kg loads. This limits a LADD with 24 links to a maximum load of 120kg.

CLADD system variables were based on the inelastic CLADD model presented in Sec. 3.1.2 and were chosen to maximize contraction, minimize link loading, match torque requirements and satisfy leg design constraints. The design parameters and

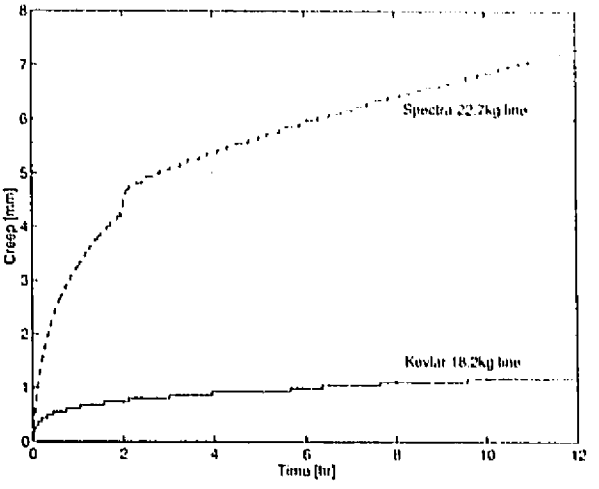

Figure 3.10: *Kevlar® 18.2kg (solid line) and Spectra® 22.7kg (dashed line) line creep. Samples, 940mm in length, were loaded with a 5kg static load over a 12 hour period. The abrupt jump in Spectra® creep at 2hrs, which is probably an artifact, does not invalidate the results. Sensor resolution was* $0.062mm$.

references for the CLADDs, and inner and outer LADDs respectively, are given in Table 3.1. In addition, limits to LADD and CLADD cell rotations are given in Table 3.2. Cell rotation for CLADDs, limited by knotting is 68°, considerably less than limits imposed by necking (92°) and IFI (122°). To increase the usable range of LADDs, it is advantageous to minimize this knotting effect, down to the physical limits imposed by necking and IFI. This is a problem worth investigating in future work.

3.1.4 CLADD Manufacturing

Our approach to the fabrication of LADDs is illustrated in Fig. 3.11. The drawing shows the outer LADD manufacturing set-up; a similar set-up is used for inner LADDs.

The two end pieces and appropriate number of cell rings are aligned axially with a mandrel (rod) that is removable from one end. The mandrel fixes the end pieces

CLADD Number	*LADD Number*	*Link Length L [mm]*	*Cell Diameter D [mm]*	*No. of Cells n*	*CLADD Application*
1	1	16.0	16.0	15	Outer LADD
	2	8.0	8.0	30	Inner LADD
2	3	16.0	16.0	15	Outer LADD
	4	8.0	8.0	30	Inner LADD
3	5	16.0	16.0	12	Outer LADD
	6	8.0	8.0	24	Inner LADD
4	7	16.0	16.0	12	Outer LADD
	8	8.0	8.0	24	Inner LADD

Table 3.1: *CLADDs designed and built based on inelastic model presented in Sec. 3.1.2. CLADD pairs 1,2 and 3,4 are for the knee and hip fore-aft ATLAS packages respectively.*

CLADD Number	$\theta^{\dagger}_{knot}$ *[deg]*	$\theta^{\dagger}_{neck}$ *[deg]*	$\theta^{\dagger}_{IFI}$ *[deg]*	*LADD Number*	$\theta^{\dagger}_{knot}$ *[deg]*	$\theta^{\dagger}_{IFI}$ *[deg]*
1	68	92	122	1	68	140
				2	69	122
2	68	92	122	3	68	140
				4	69	122
3	*na**	74	122	5	*na**	140
				6	*na**	122
4	*na**	74	122	7	*na**	140
				8	*na**	122

Table 3.2: *LADD and CLADD limits on cell input rotation. Refer to Table 3.1 for CLADD and LADD design parameters. (*† *Values are given per cell:* $\frac{\theta}{n_i+n_o}$ *for CLADDs and* $\frac{\theta}{n}$ *for LADDs.* * *Not available.)*

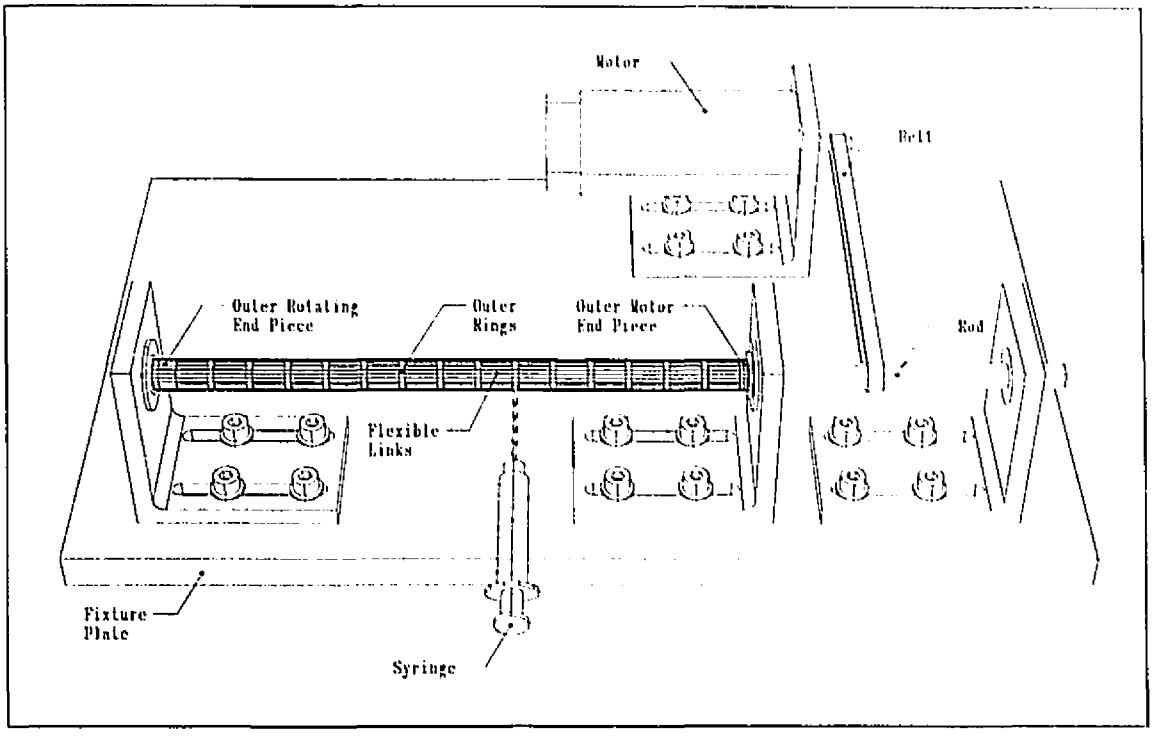

Figure 3.11: *The outer LADD is set rotating for the final bonding of the fibers to the rings and the end pieces. The epoxy is applied with the help of a syringe needle which provides an excellent application tip. The constant rotation of the LADD during this process provides excellent control over the adhesive application and the subsequent 12 hour drying stage.*

at the desired total LADD length. A single *Spectra*® $22.7kg$ line is used to string the entire LADD through the holes located in the end pieces. This minimizes the problem of dealing with 48 end conditions down to only 2, thus producing a more reliable and stronger LADD. Every time the fiber is threaded across, a $1.5kg$ load is used to tension the fiber and the tensioned link is bonded at both end pieces with fast-drying *Permabond*® *Bonding Adhesive* before the next threading. The line is threaded through every fourth hole, and the two free ends are tied together.

The rings are then equally spaced using a comb with the appropriate cell length and grooves of the appropriate ring width. With two of these combs in place, selected

fibers are tacked to the rings with drops of fast-drying glue. After the glue sets, the combs are removed and the LADD is set rotating for the final bonding of the fibers to the rings and the end pieces. The two-part epoxy, *CIBA-GEIGY Araldite*®, is mixed and left to cure for 45 minutes. This gives it the right consistency preventing the epoxy from running up the links. This is especially important for the inner LADDs where the small cell diameter ($D = 8.0mm$) packs the 24 $0.5mm$ diameter links tightly together. The epoxy is applied with the help of a syringe needle which provides an excellent application tip. Two coats of epoxy are applied. The first is a light application, while the second sculpts the epoxy into a bead stretching evenly around the circumference of the rings. The steady rotation of the LADD during this process provides excellent control over the adhesive application and the subsequent 12 hour drying stage.

The LADD is allowed to cure for an additional 48 hours (without rotation) before being disassembled from the mandrel and waiting 7 days before being placed into operation. Individual LADD cost is in the order of $240 requiring a complete design to implementation timeline of 2 weeks. A detailed list of manufacturing and materials costs is included in Appendix C. We expect with further design iterations and improved fabrication techniques that both the cost and timeline of LADD manufacturing can be significantly reduced. The two knee ATLAS CLADDs are shown in Fig. 3.12.

3.2 Variable Radius Pulley (VRP)

3.2.1 VRP Algorithm

The solution to maintaining tension in ATLAS lies in a Variable Radius Pulley (VRP) that compensates for the difference in the rates of contraction and extension of the protagonist and antagonist CLADDs. The derivation of the VRP focuses on the principles of virtual work and geometry taken from [12].

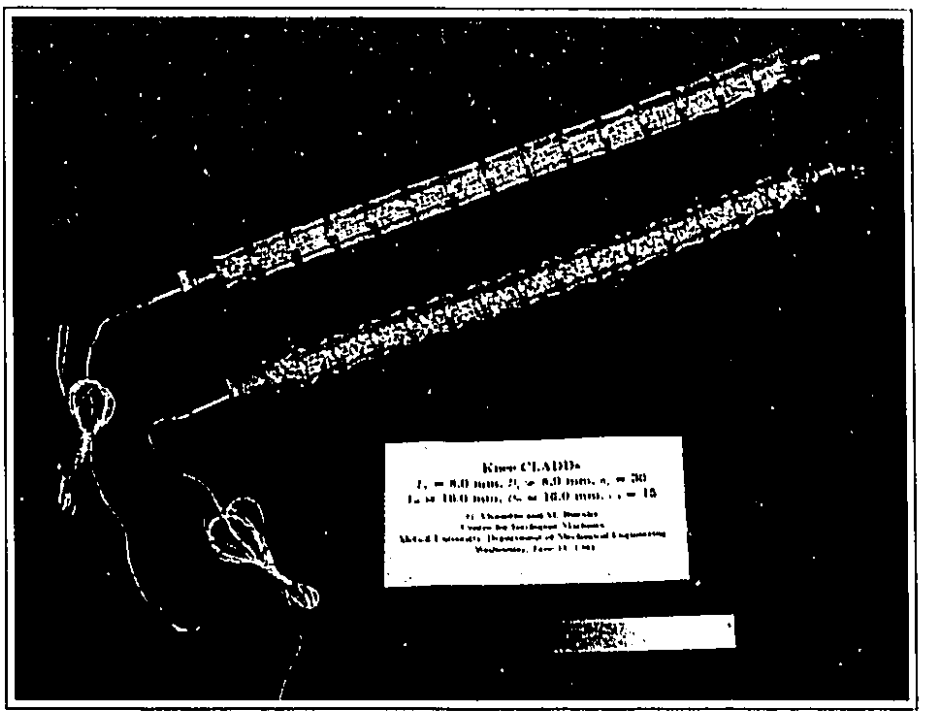

Figure 3.12: *Knee ATLAS CLADDs.*

A CLADD and pulley system driven by a motor is shown in Fig. 3.13. Applying the principle of virtual work, we equate the total input work to the total intermediate CLADD work and to the total output work at the pulley, $\tau_i d\theta = Fdl = FRd\phi = \tau_o d\phi$. From this we get two important relations. First,

$$d\theta = \frac{\tau_o}{\tau_i} d\phi \tag{3.16}$$

which, when integrated, specifies the CLADD input angle θ given a specific torque ratio τ_o/τ_i and pulley position ϕ. The second relation

$$R = \frac{\tau_o}{\tau_i} \left. \frac{dl}{d\theta} \right|_\theta$$

gives the required lever arm R satisfying the torque ratio and contraction rate $dl/d\theta$.

In ATLAS, the antagonist and protagonist CLADDs must satisfy two operating boundary conditions. First, the two CLADDs driven by the same motor implies $\theta_{ant} = \theta^o_{ant} + \theta^o_{prot} - \theta_{prot}$, where superscript o denotes a pretwist, and subscripts

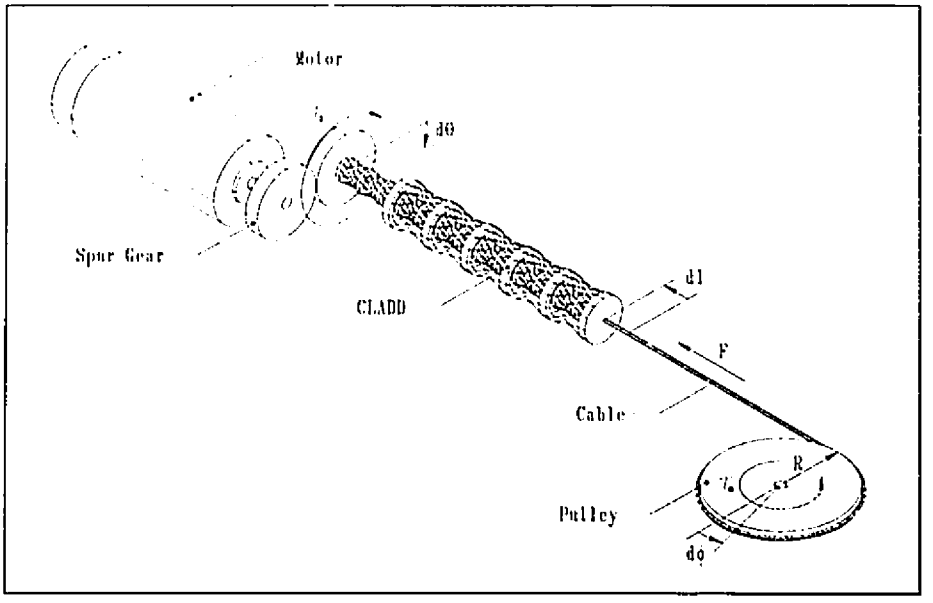

Figure 3.13: *CLADD and pulley system driven by a motor.*

ant and *prot* refer to the antagonist and protagonist respectively. Second, to maintain tension requires

$$\left(\frac{d\theta}{d\phi}\right)_{ant}\Big|_{\phi} = \left(\frac{d\theta}{d\phi}\right)_{prot}\Big|_{\phi}$$

and recalling expression (3.16), we have

$$\left(\frac{\tau_o}{\tau_i}\right)_{ant} = \left(\frac{\tau_o}{\tau_i}\right)_{prot}.$$

This means that the same desired torque ratio τ_o/τ_i should be used for both antagonist and protagonist pulley surfaces. The resulting VRP not only gives the desired torque ratio, but also keeps both CLADDs in tension.

The torque ratio can be constant or some position-dependent relation. However, there are limitations. First, discontinuities in the torque ratio are not possible, since the output of the CLADD is continuous. Second, large deviations over small rotations are not acceptable. Large decreases would not allow the previous larger lever to rotate out of the way, and large increases would cause the fiber to separate from the surface.

Knowing the effective radius R at any given pulley position ϕ, the geometry depicted in Fig. 3.14 gives a description of the position of the CLADD in the form of a line equation with its origin at the pulley center. The initial position of the protagonist is shown in Fig. 3.14(a), where

$$\beta = \arctan\left(\frac{Offset}{Base}\right); \quad \gamma_1 = \arccos\left(\frac{R_1}{Arm}\right); \quad \text{and,} \quad \phi_1 = \gamma_1 + \beta.$$

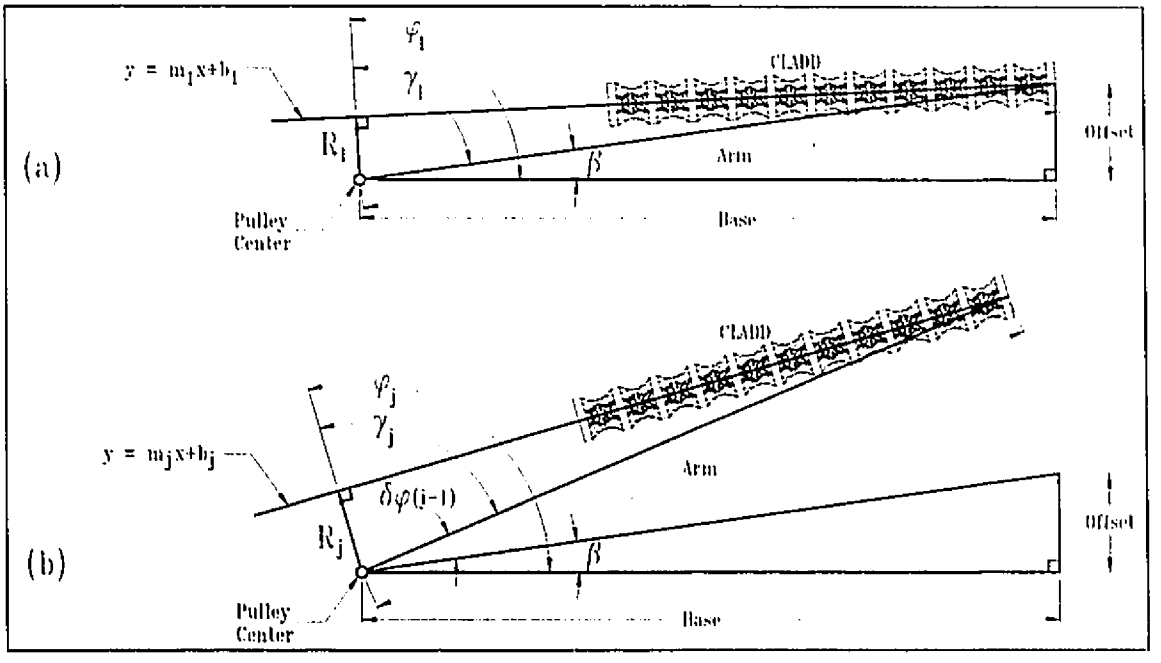

Figure 3.14: *VRP geometry.*

Since the CLADD approaches the pulley surface tangentially, the slope of the line that describes the current CLADD position is perpendicular to the slope of R_1 with respect to the *Base*, $m_1 = -\cot\phi_1$. To solve for b_1, we use the coordinates of the end point of R_1, $(x_1, y_1) = (R_1\cos\phi_1, R_1\sin\phi_1)$, and substitute them along with m_1 into the line equation $y = m_1x + b_1$ to get

$$b_1 = R_1(\sin\phi_1 + \cos\phi_1\cot\phi_1). \tag{3.17}$$

By keeping the pulley fixed and incrementing the *Arm* by $d\phi$ from its initial angle, the various descriptions of CLADD positions encapsulate the desired pulley surface,

Fig. 3.14(b). We generate a set of equations describing the positions of the protagonist CLADD,

$$\begin{aligned}
\beta &= \arctan\left(\frac{Offset}{Base}\right); \\
\gamma_j &= \arccos\left(\frac{R_{prot_j}}{Arm}\right); \\
\phi_j &= \gamma_j + \beta + d\phi(j-1); \\
y &= m_j x + b_j; \\
m_j &= -\cot\phi_j; \qquad (3.18) \\
b_j &= R_j(\sin\phi_j + \cos\phi_j \cot\phi_j); \qquad (3.19) \\
\theta_{prot_j} &= \frac{\tau_o}{\tau_i}\phi_j + \theta^o_{prot}; \quad \text{and,} \\
R_{prot_j} &= \frac{\tau_o}{\tau_i}\left.\frac{dl}{d\theta}\right|_{\theta_{prot_j}},
\end{aligned}$$

where $j = 1 : m$, and m is the number of increments of $d\phi$ over the pulley range ϕ.

Finding the intersection of two successive lines gives a point describing the pulley surface. This intersection approach results in a smooth transition between successive varying radii. The increment $d\phi$ should be made small enough to maximize pulley surface continuity. The pulley X and Y surface coordinates are given as a function of two successive slopes and y-intercepts,

$$(X_j, Y_j) = \left(\frac{b_{j+1} - b_j}{m_j - m_{j+1}}, \frac{m_j b_{j+1} - m_{j+1} b_j}{m_j + m_{j+1}}\right). \qquad (3.20)$$

For the antagonist CLADD, we apply the same procedure as above and substitute θ with $\theta_{ant} = \theta^o_{ant} + \theta^o_{prot} - \theta_{prot}$.

The algorithms that generate the pulley surfaces for the protagonist and antagonist CLADDs are coded in a $MATLAB^{®}$ program given in Appendix E. The program generates the necessary pulley X and Y surface coordinates that are then loaded in a CAD program for final pulley design. In addition, the program generates the tool path given the tool diameter and rotates the pulley surface coordinates, if so desired.

The required inputs to the program are ATLAS variables: τ_o/τ_i, L_i, D_i, n_i, L_o, D_o, n_o, θ^o_{prot}, θ^o_{ant}, $Base$, $Offset$, $d\phi$ and pulley range ϕ. The final CAD design is downloaded to a numerically controlled milling machine for fabrication.

3.2.2 VRP Detail Design

The VRP design required a compromise between torque ratio τ_o/τ_i and pulley range ϕ: more of one, meant less of the other. A torque ratio of 25 : 1 is achieved between the CLADDs and VRP for both ATLAS packages. This pairs with a pulley range ϕ of 110° and 80° for the knee and hip respectively. A pretwist θ^o of 720° was assigned to each CLADD to deal with near zero pulley radii at small CLADD input angles. An $Offset$ of $30mm$, and $Base$ of $374mm$ and $215mm$ for knee and hip were imposed by leg design constraints. CLADD variables are given in Table 3.1. The total input rotation to the knee and hip CLADDs are 9.6 and 7.5 revolutions respectively.

An unsuspected problem with the VRP detail design was CLADD compliance. Early experimental work with CLADDs revealed that the contraction rate $dl/d\theta$ was load dependent. Therefore, we replaced (3.3) with experimental data of CLADDs loaded with a $15kg$ load. Data from each pair of similar CLADDs was averaged for their respective pulleys. Further details on CLADD compliance is included in Chapter 4.

Detail designs of both VRPs are given in Fig. 3.15. The pulleys were designed compact and of minimal mass; $89g$ for the knee and $77g$ for the hip. The CLADD load ends are connected to the VRP with a cable to take up the end rotation of the CLADDs. The cable loops around a pin that is tightened with a wrench and then locked with a nut.

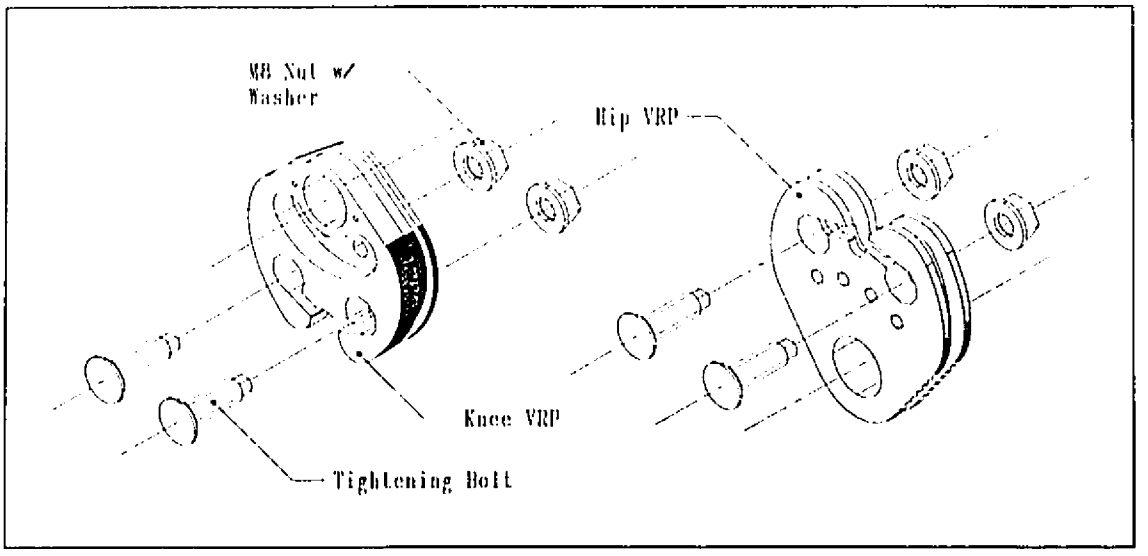

Figure 3.15: *Knee (left) and hip (right) VRP detail designs with cable tightening systems.*

3.3 ATLAS Packages

The ATLAS transmission housing provides the gearing that allows the single electric motor to drive the two antagonistic CLADDs. Details of the housing are shown in Fig. 3.16. The housing (part 75) provides support for both hip and knee motors (part 18), in addition to their respective CLADD pairs. The leg processor board (part 1), that provides low level servo control, is conveniently mounted on the housing. The knee ATLAS package is shown in Fig. 3.17. The hip ATLAS package is similar in design except for the hip requiring guide wheels (part 33, see Fig. 2.7) to redirect cables back up to the hip VRP. This configuration houses both motors near the hip, lowering the leg inertia significantly.

Combined needle roller/axial ball bearings (*INA NX 7*) (part 108) support the axial load on each CLADD while allowing the torque input through spur gears (parts 94,97). The spur gears are double supported, on one end with the roller/axial ball bearings and the other with flanged ball bearings (part 109). This ensures proper gear alignment under heavy operation. The spur gears between the motors and CLADDs provide

Knee Transmission	*Gear Ratio*	*Mass [kg]*	*Efficiency [%]*	*Increase in Leg Inertia [%]*
Current ATLAS	50 : 1	0.9	$85 \sim 90^*$	5
Optimized ATLAS†	50 : 1	0.7	$85 \sim 90^*$	4
Harmonic Drive [1, 4]	60 : 1	1.2	$80 \sim 90$	58
Planetary Gearhead [5]	71 : 1	1.6	70	65

Table 3.3: *Comparison of selected CARL knee transmissions. (*Expected ATLAS efficiencies based on CLADD efficiencies presented in Sec. 4.6. †Mass saving are achieved with material substitutions given in Appendix D.)*

additional gear reduction of 2 : 1, bringing the total torque ratio between motor and joint to 50 : 1.

The two packages, without motors weigh $0.9kg$ and $1.0kg$ respectively, assuming the mass of the shared parts is equally divided between them. These mass savings favor considerably with the $1.2kg$ harmonic drive lateral actuation. The quadruped weight savings are $2.0kg$ with ATLAS as opposed to all harmonic drive. Additional mass savings through material substitution are given in Appendix D, reducing both packages to $0.7kg$.

Positioning of motors is critical for minimizing inertia in multi-limbed robots. A comparison of our current knee ATLAS package and optimized one, against knee actuation with a harmonic drive or planetary gearhead suitable for the *Maxon 2260* ($1.3kg$) is given in Table 3.3. The latter two require the motor in close proximity of the joint, significantly increasing the leg inertia ($0.4kg\,m^2$ without actuation) by 58% and 65% respectively. This is an order of magnitude larger than the knee ATLAS package that increases leg inertia by only 5%. CLADD efficiencies (see Sec. 4.6) are comparable to harmonic drives and favorable over planetary gearheads.

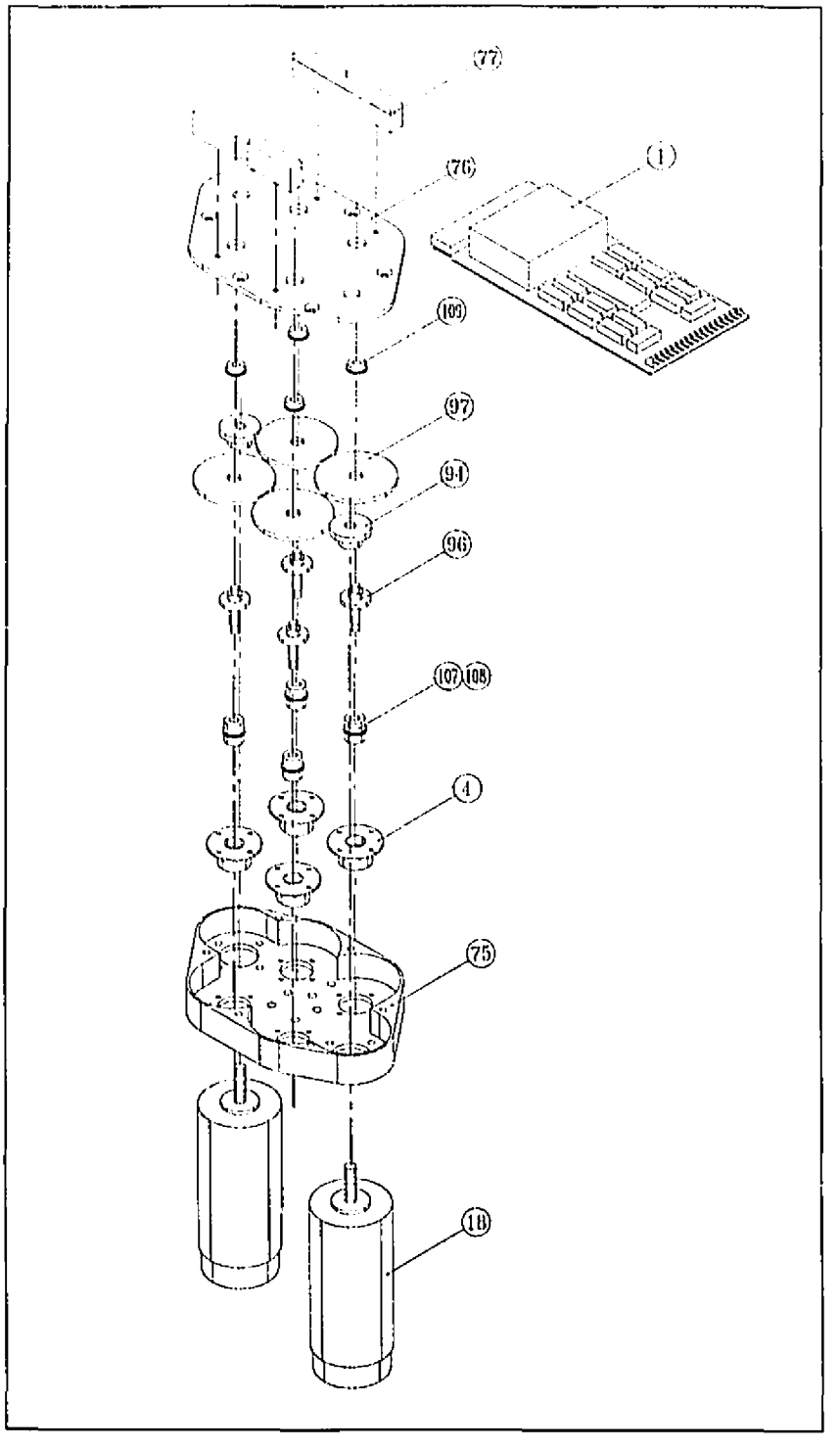

Figure 3.16: *Exploded view of ATLAS transmission housing. Refer to Appendix B for CARL's list of parts. Fasteners and keyways are not shown.*

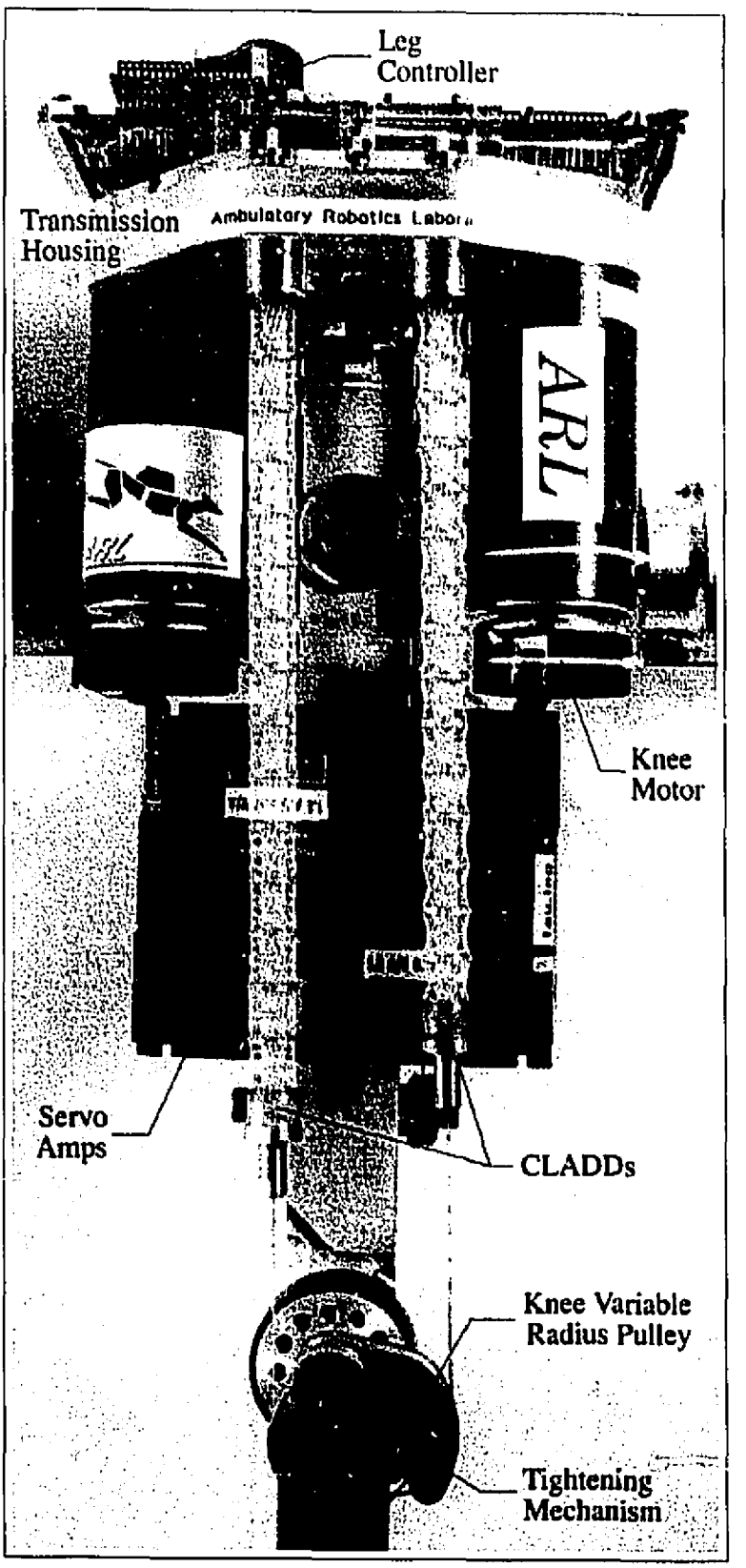

Figure 3.17: *Knee ATLAS.*

Chapter 4

(C)LADD Modeling

Accurate kinematic models of LADDs and CLADDs are vital to both the design and control of ATLAS. The inelastic LADD and CLADD models presented in Sec. 3.1.2 upon which we based our CLADD design are experimentally tested in Sec. 4.3. Finding the inelastic models inadequate, in Sections 4.4 and 4.5 we propose and validate improved kinematic models for both LADDs and CLADDs. Finally, we review CLADD efficiency and LADD manufacturing repeatability in Sections 4.6 and 4.7 respectively.

4.1 Experimental Set-Up

4.1.1 Mechanical Hardware

Kinematic validation of the CLADDs and their respective inner and outer LADDs (see Table 3.1) involved testing them under a variety of static loads with the mechanical set-up illustrated in Fig. 4.1. A $19mm$ thick aluminum plate with equally spaced $M8$ tapped holes serves as a fixture for all experimental work. All mechanical components are fixed to the plate with bolts, allowing for quick set-up and turnover.

A $80W$ brush DC motor (*Maxon 2260*) is used to actuate the LADDs. A combined needle roller/axial ball bearing (*INA NX 7*) supports the axial LADD load on the

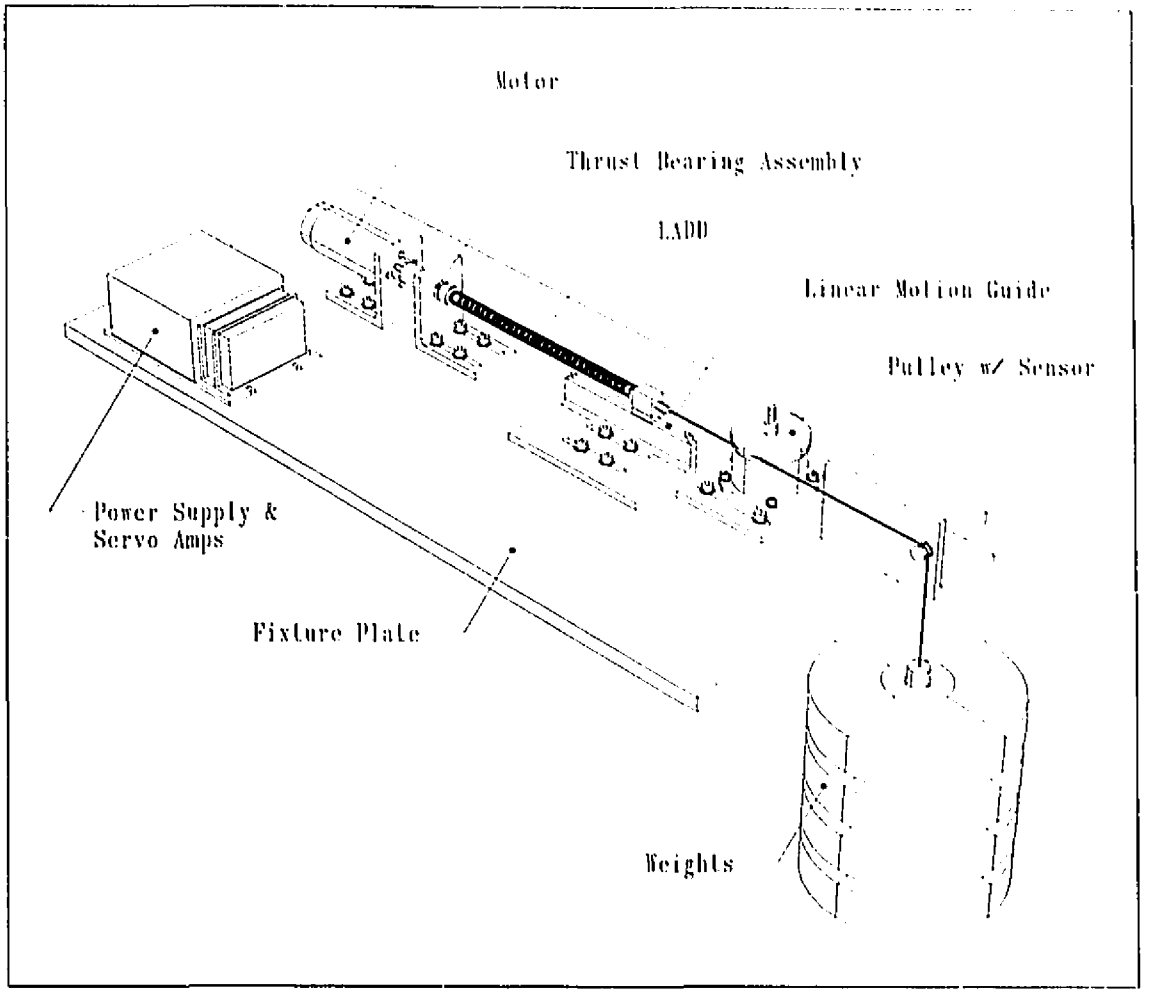

Figure 4.1: *Mechanical set-up for kinematic validation of LADDs.*

motor while allowing the torque input. A linear motion guide (*THK RSR series*) maintains the torque differential across the LADDs allowing the free end to translate. For CLADD testing, the linear motion guide is removed. LADD displacements are measured via a pulley assembly instrumented with an incremental optical encoder (*Hewlett Packard's HEDS-6010*). An identical sensor fixed to the motor shaft is used to monitor motor displacements. The motor torque is available as a feedback signal from the servo amplifier. A *Kevlar*® line rated at $272.7kg$ break strength attaches to the translating LADD end, loops around the pulley and over an idler to a fixed load.

Data for constant load runs (weights attached to the LADDs as shown in Fig. 4.1) were collected over ten periods of full LADD contraction and extension. The actuation rate was kept at a low $0.1Hz$ to avoid dynamic effects. The maximum load applied was set by the maximum allowable continuous motor torque of $0.4Nm$, while short term peak motor torques were allowed up to $1.8Nm$. As a result, the maximum loads for both outer and inner LADDs were $25kg$ and $35kg$ respectively, and $50kg$ for CLADDs. A lower bound on the input angle θ_{min} was established to avoid data scatter at low sensor values, while an upper bound θ_{max} avoided LADD knotting (see Sec. 3.1.3). These bounds were different for inner LADDs, outer LADDs and CLADDs, and limited the modeling range of each device.

4.1.2 Electronic Hardware

The electronic interface to the mechanical hardware is illustrated in Fig. 4.2. A single *XP/DCS* transputer node [3] is used to read and process sensor signals, compute control outputs, log data, and interface with servo amplifiers. The *XP/DCS* consists of a processor board and a custom I/O board which links sensors and servo amplifiers to the *XP/DCS*. This custom I/O board performs analog to digital data conversion for servo amplifier feedback signals, quadrature decoding of raw encoder signals, and digital to analog conversion of controller output signals.

Software is developed and compiled on a *Sun SPARCstation* and downloaded through an ethernet link (*IMS B300 TCPlink*) to the *XP/DCS* board before an experimental run. There is no communication between the *XP/DCS* and the *SPARCstation* during the run. After the experiment is completed, logged data is downloaded to the *SPARCstation* for offline analysis by the user.

Power for the motor comes from the grid through a single *Advanced Motion Controls PS2x300W* unregulated DC power supply which feeds an *Advanced Motion Controls 25A PWM* servo amplifier. The servo amplifier can provide $2kW$ peak power and servo the motor current at a $2.5kHz$ closed loop bandwidth. The servo amplifier

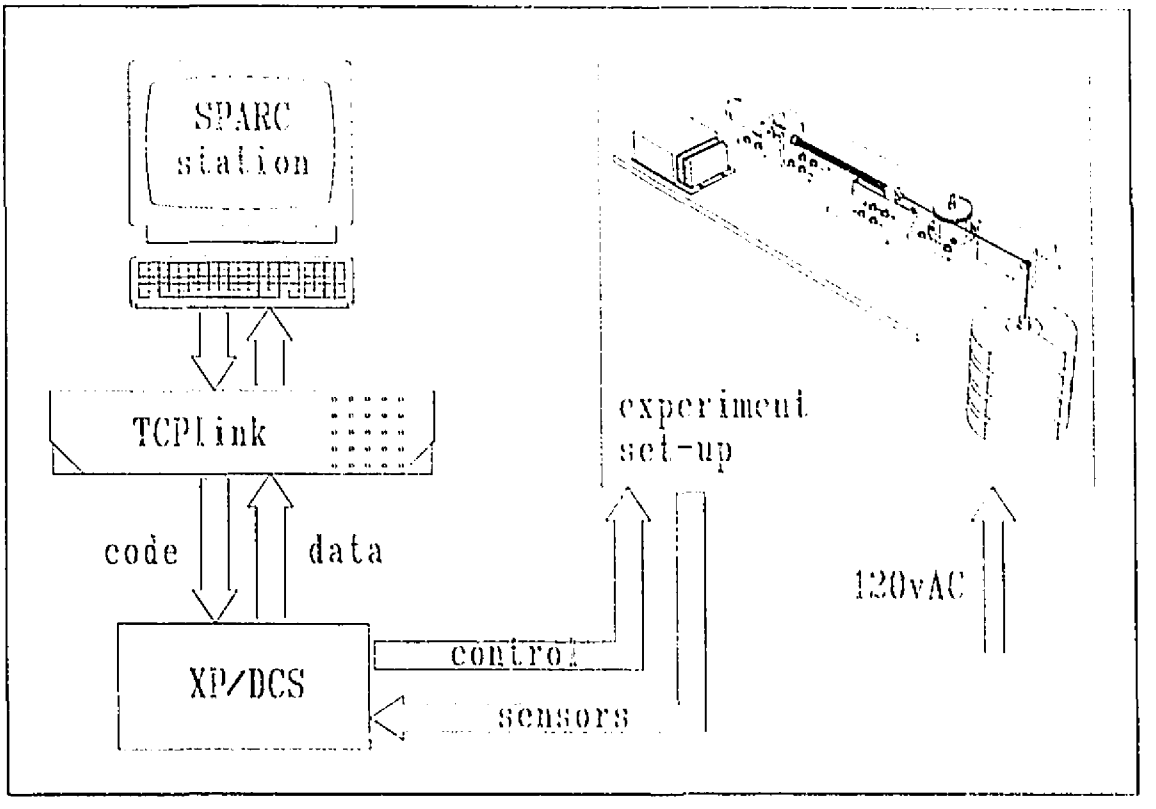

Figure 4.2: *Electronic hardware connection diagram.*

operates in a current feedback mode allowing motor torque to be specified directly.

4.1.3 Software

C coded software is developed and compiled on the *SPARCstation* before being loaded into the transputer. The software consists of an initialization routine, a main loop and a data recovery routine which downloads data from the transputer memory to the *SPARCstation* following the experimental run. The main loop is executed once every millisecond and performs the following functions:

- keeps track of real time used to compute time dependent physical quantities and to synchronize the controller frequency;
- reads raw sensor data through the I/O board;

- processes raw sensor data into usable form including differentiation and filtering of position data to obtain rates;
- maintains a watchdog timer signal which disables the servo amplifiers when the signal is not present;
- controls an audible alarm which informs the operator of the beginning and end of an experimental run;
- runs the control algorithms to determine desired torque values;
- sends desired torque values to the servo amplifiers which control and power the motors; and,
- records experimental data into an array for later recovery into the *SPARCstation*.

4.2 Experimental Issues

Issues relating to experimental error and properties unique to LADDs are addressed before evaluating the experimental data.

4.2.1 Hardware Experimental Error

Sensor Resolution

Motor and LADD displacements are measured with incremental optical encoders (*Hewlett Packard's HEDS-6010*) which have a resolution of 1024 quadrature counts per revolution. A quadrature decoder-counter interface IC (*Hewlett Packard's HCTL-2016*) quadruples the resolution to 4096 counts per revolution, equivalent to 0.001534 radians per count. With a pulley radius of 40.2mm (including cable thickness), a maximum resolution of 0.062mm for LADD displacements and 0.001534rad for motor displacements are obtainable.

Cable Creep

Two types of lines were available to attach the translating LADD end to the load: a *Spectra*® 136.4*kg* line and a *Kevlar*® 272.7*kg* line. Any stretch in the cable between the LADD and pulley would affect recorded LADD displacements. Therefore, their creep properties were evaluated. One sample of each line, 940*mm* in length, was monitored for a 12 hour period under a 60*kg* static load, Fig. 4.3.

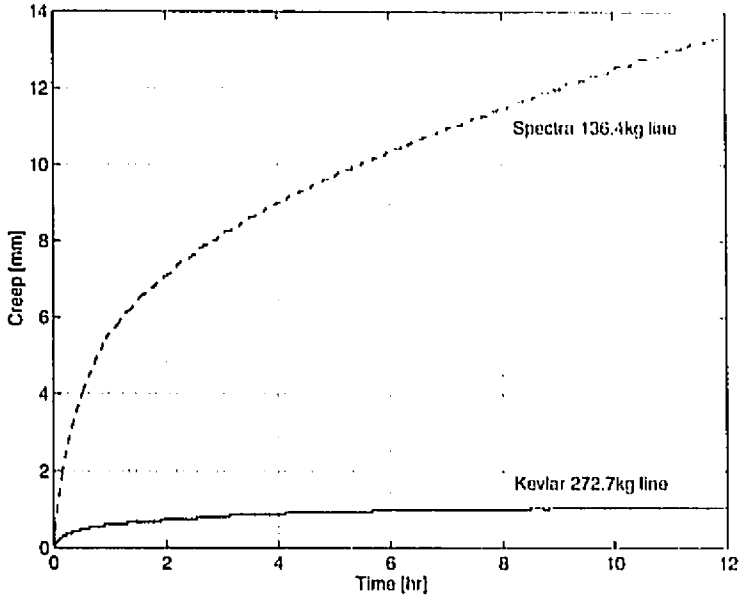

Figure 4.3: *Kevlar*® *272.7kg (solid curve) and Spectra*® *136.4kg (dashed curve) line creep. One sample of each, 940mm in length, was loaded with a 60kg static load over a 12 hour period. Sensor resolution was* 0.062*mm*.

The *Kevlar*® line crept 1.05*mm* (0.11%) and remained steady for a 3 hour period. The *Spectra*® line, in contrast, crept over 13.43*mm* (1.43%) in 12 hours and worse, still exhibited a steady creep rate of 0.51*mm/hr* (0.054%/*hr*) at that time. A repeated test on the 272.7*kg Kevlar*® line revealed even less creep of 0.68*mm* (0.072%) over the same period. As a result, we used the *Kevlar*® line for all our experimental work.

Using this last data set and linear interpolation for different line lengths and weights, we estimate creep values. With a maximum cable length linking the LADD to the pul-

ley of $250mm$ and maximum static load of $50kg$, we expect a maximum creep during 1 hour break-in and 10 minute experiment runs of $0.06mm$ and $0.01mm$ respectively. Since these values fall below the $0.062mm$ resolution of LADD displacement measurements, we need not to be concerned with creep effects. However creep for longer term experiments will have to be addressed separately.

4.2.2 LADD Break-In

In order to verify LADD models, repeatable experiments are a basic prerequisite. We found two dominant "break-in" phenomena which have to be eliminated or characterized before modeling can begin. The first one, fiber creep, has been documented in Sec. 3.1.3 for individual links. The second effect, glue shaping, is caused when the cell links slowly work away the corners of the glue that bond them to the LADD rings and end pieces. Both effects can be minimized by proper break-in procedures described below. However, both effects show non-vanishing steady state changes which, though small, may contribute to the current modeling limits.

LADD Fiber Creep

We applied a $50kg$ static load to each LADD at full extension for a 12 hour period. Since each LADD was designed with 24 *Spectra*® links, this loading represents 9.2% of each line's $22.7kg$ break strength. The results are shown in Fig. 4.4: LADDs 1 through 3 exhibited a total "break-in" creep of $1.54mm$ (0.64%), while LADD 4 was slightly larger at $1.73mm$ (0.72%). LADDs 1 and 4 approached a creep rate of $0.04mm/hr$ (0.017%/hr) versus $0.05mm/hr$ (0.021%/hr) for LADDs 2 and 3.

This data shows that there is substantial break-in creep which must be eliminated before model validation. Unfortunately, the creep continues at a slow, but steady rate. This does not affect our relatively short experimental runs, but could be a problem for long term LADD operation.

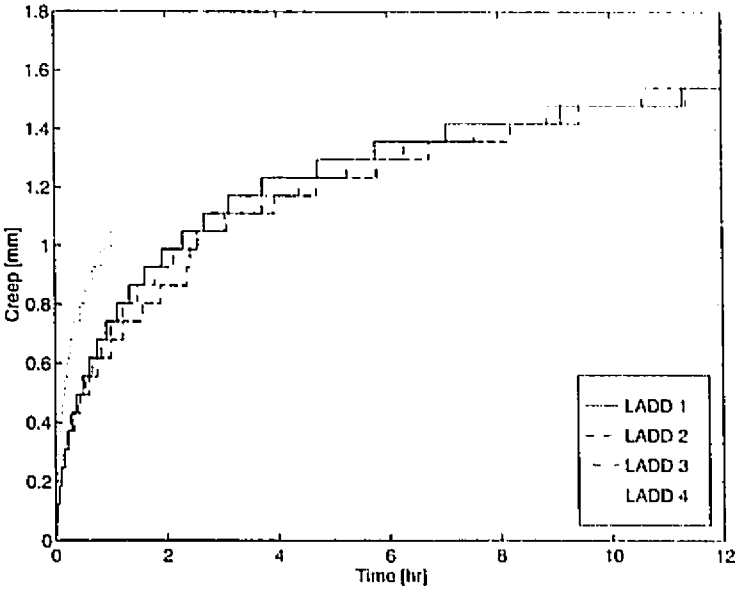

Figure 4.4: *LADD fiber creep at full extension under a 50kg load over a 12 hour period. With each LADD designed with 24 Spectra® links, this loading represents 9.2% of each line's 22.7kg break strength. Steady creep rates of 0.04mm/hr and 0.05mm/hr were recorded by LADDs 1,4 and LADDs 2,3 respectively. Sensor resolution was* $0.062mm$.

LADD Glue Shaping

Glue shaping arises because the epoxy that bonds the *Spectra®* fibers to the aluminum rings gives way as the cells are twisted and untwisted repeatably. We operated the LADDs for $30min$ at $0.1Hz$ over the maximum operating range of each LADD under loads of $12.5kg$ and $25kg$ for outer and inner LADDs respectively.

The first $30min$ tests on the four LADDs showed that the kinematics varied noticeably ("break-in" effect) while the second showed immediate convergence. Fig. 4.5 illustrates this behavior for LADD 1. We plot the LADD contraction dl for every contraction input angle θ of $16rad$. The first run shows a large initial break-in followed by a steady rate of $0.35mm/hr$ ($0.15\%/hr$). In the second $30min$ run, the

convergence is quicker and a rate of $0.30mm/hr$ $(0.13\%/hr)$ is recorded. These rates are an order more than those obtained from fiber creep, making LADD glue shaping the dominating "break-in" effect.

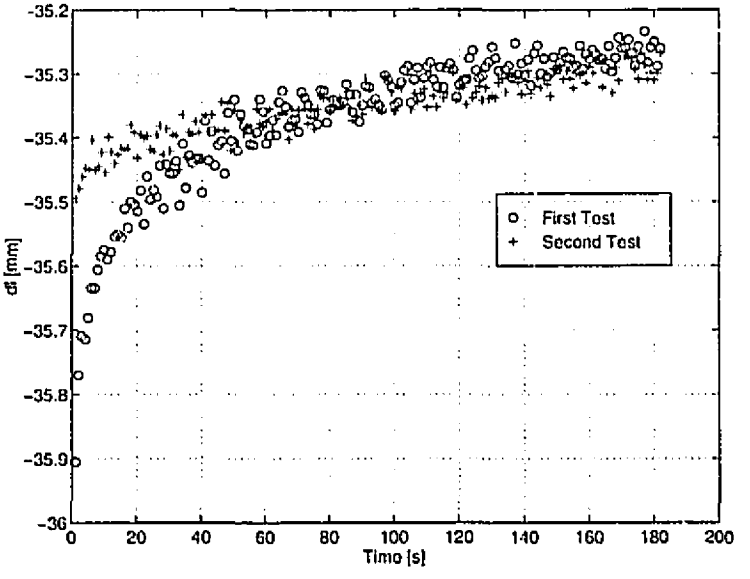

Figure 4.5: *LADD 1 glue shaping tests. Variations in LADD kinematics were verified with break-in tests that ran for* $30min$ *at* $0.1Hz$ *over the maximum operating range of each LADD under loads of* $12.5kg$ *and* $25kg$ *for outer and inner LADDs respectively. We plot the contraction dl of LADD 1 for every contraction input angle* θ *of* $16rad$*, where "o" and "+" refer to the first and second tests respectively. The first run shows a large initial break-in followed by a steady break-in rate of* $0.35mm/hr$ $(0.15\%/hr)$*. In the second run, the LADD immediately approaches a steady rate of* $0.30mm/hr$ $(0.13\%/hr)$*.*

4.3 Inelastic (C)LADD Model Validation Results

Inelastic LADD Model

Motor torque plots for LADD 4 are shown in Fig. 4.6 along with torque predictions by the inelastic LADD model (3.3). Torque scatter for the $1kg$ load is a result of

the torque feedback signal resolution ($0.02Nm$) being of the same order as the data. The offset in the motor torque data between extension and contraction is due to the combined friction torques in the bearings of the motor, thrust bearing assembly, linear motion guide and pulleys. Given the limited accuracy of the measured data, the model matches the data and is acceptable, even though it deviates increasingly towards large motor angles.

More problematic is the kinematic relationship between motor input angle and LADD length. The experimental contraction length dl of LADD 4 is plotted with the inelastic LADD model (3.2) in Fig. 4.12. LADD 4 had a full scale model difference of 18.3% at a $1kg$ load and 9.2% at a $35kg$ load. We notice as the motor angle θ increases, the magnitude of error increases as well and in contrast, as the load F increases, the error reduces. The other LADDs illustrate the same behavior with similar errors. Clearly an error of up to 20% is not acceptable as a basis for design and control with LADDs.

The motor torque predictions, Fig. 4.6, show that the model predicts the general trend with noticeable deviations at large motor angles. This is the same trend as with the kinematic validation. This is to be expected since the torque relation (3.3) is derived from the kinematic relation (3.1). Therefore, we can expect that an improvement in the kinematic model will undoubtedly bring about improvements in the motor torque predictions.

Inelastic CLADD Model

Similar kinematic validation experiments were conducted on CLADDs 1 and 2 (see Table 3.1). Results for CLADD 1 are shown in Figures 4.7 and 4.13. Just as for the LADDs, the inelastic model for the CLADDs fails to match the experimental data by as much as 20% full scale, and the error is a function of both input angle as well as load. Again, an improved model is necessary.

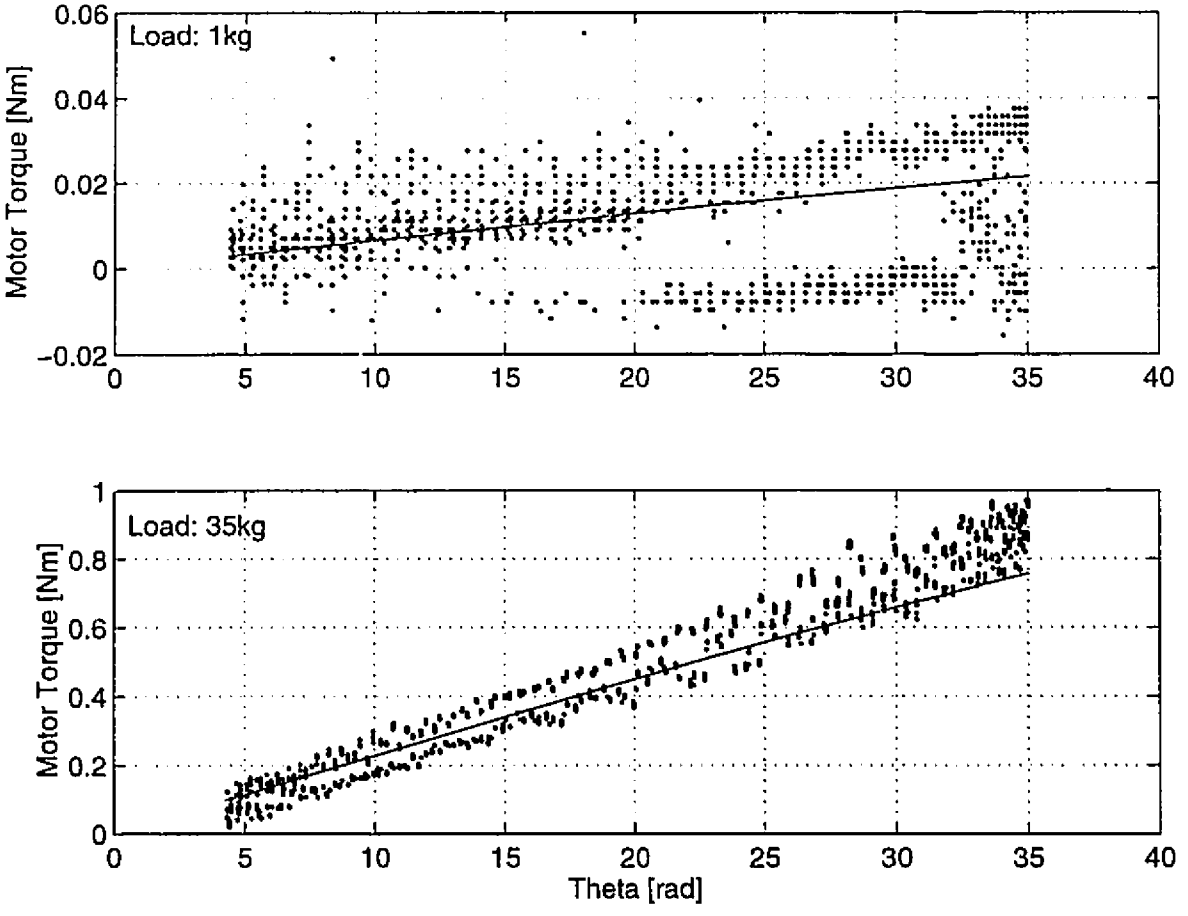

Figure 4.6: *LADD 4 Statics. Experimental motor torque data (:) for the 1kg and 35kg runs of Fig. 4.12 are shown with torque predictions given by the inelastic LADD model (3.3) (solid curve). Torque scatter for the 1kg load (:)(upper plot) is a result of the torque feedback signal resolution (0.02Nm) being of the same order as the data. A look at the 35kg load data (:)(lower plot) shows that the model predicts the general trend but deviates at large motor angles. The offset in the motor torque data between extension and contraction is due to the combined friction torques in the bearings of the motor, thrust bearing assembly, linear motion guide and pulleys.*

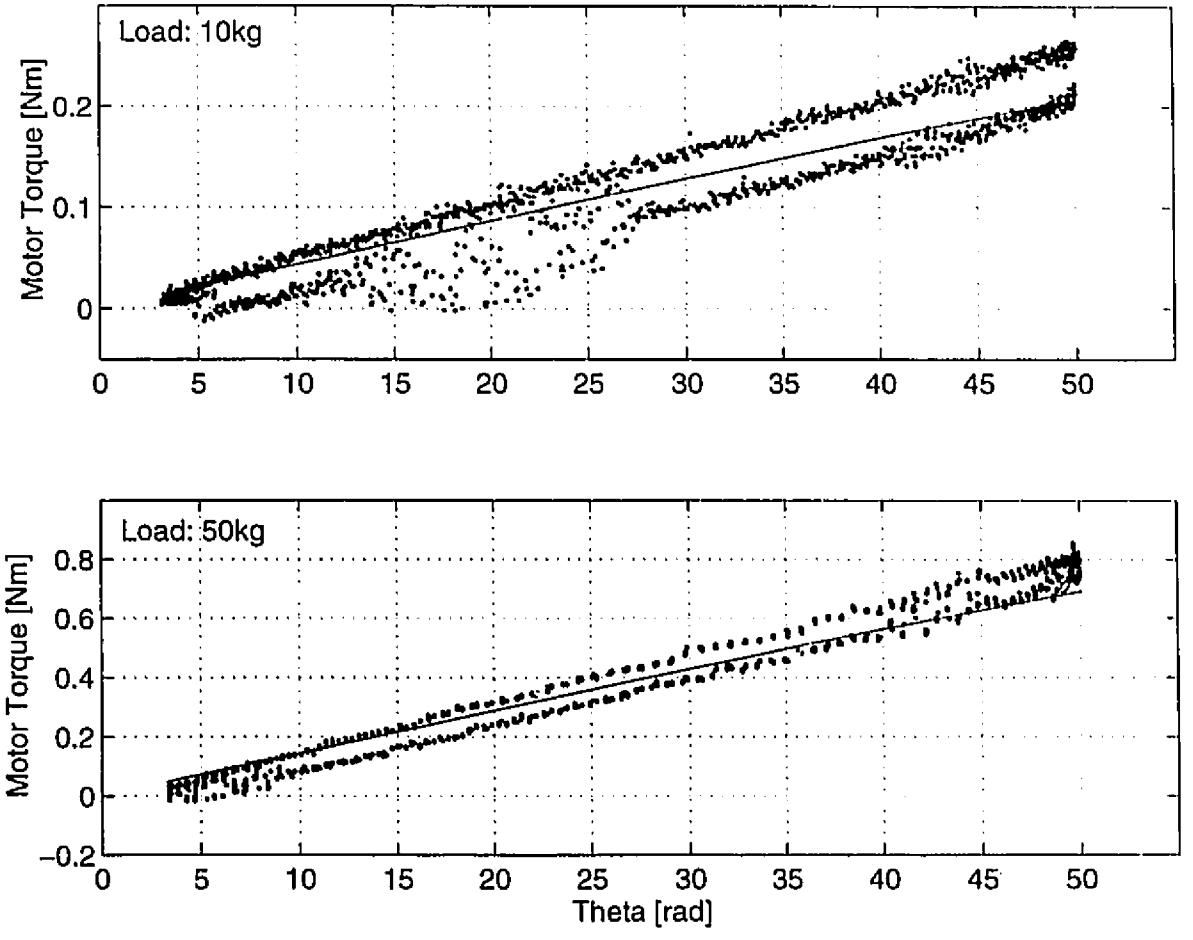

Figure 4.7: *CLADD 1 Statics. Experimental motor torque data (·) for the 10kg (upper plot) and 50kg (lower plot) runs of Fig. 4.13 are shown with torque predictions given by the inelastic CLADD model (3.14) (solid curve). Both plots show that the model predicts the general trend deviating at large motor angles.*

4.4 New LADD Models

The results from the previous model validation section establish a clear need for a compliance model, since the modeling error is directly related to the applied load. While previous work on compliance models [22, 33] simply attributed this to fiber elasticity, both our experiments with fiber creep and others [13] show that *Spectra*®'s high stiffness cannot account for this effect.

Fiber Bending

A close look at a LADD cell in operation shows that the links have a finite curvature at the boundaries to the rings due to the clamping action of the epoxy, as illustrated in Fig. 4.8. This contradicts the inelastic model's assumption that LADD cell links remain straight during operation. We observe that fiber bending becomes more apparent at large cell twist angles and vanishes at near zero twist angles. Furthermore, the effect diminishes with increasing LADD loads. This explains very well the increasing errors at large angles and decreasing errors at large forces between the inelastic models and our experiments, as shown in Figures 4.12 and 4.13. Thus we are motivated to include a force dependent "fiber bending term" in the inelastic theory, captured in the "Local Compliance Model" described below, to improve model predictions.

4.4.1 Local Compliance Model (LCM)

The LCM identifies an effective fiber link length L as a function of both LADD angle θ and load F. It is titled "local" because it addresses the previously identified modeling problem due to fiber bending at the source, locally at the level of the individual cell kinematics, before the overall LADD kinematics are developed. Motivated by the particular form of the errors (see Fig. 4.9) between the inelastic model and

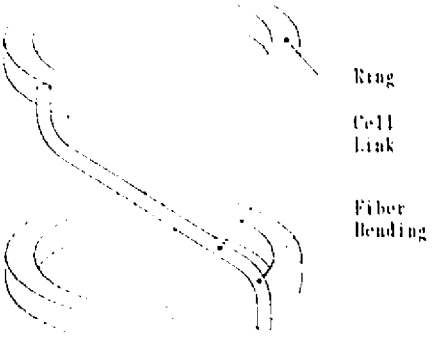

Figure 4.8: *Cell link fiber bending.*

experiments, $L(\theta, F)$ was chosen to be of the form

$$L(\theta, F) = L^o - a(F)\frac{\theta^2}{n^2}, \qquad a(F) = b_1 exp^{b_2 F} + b_3 \tag{4.1}$$

where L^o is the design cell length L.

Using the same approach as the inelastic LADD model, we derive the kinematic and static relations of the LCM as

$$l(\theta, F) = n\sqrt{\left(L^o - a(F)\frac{\theta^2}{n^2}\right)^2 - D^2 sin^2\left(\frac{\theta}{2n}\right)} \tag{4.2}$$

and

$$r(\theta, F) \stackrel{\text{def}}{=} \frac{\tau}{F} = -\frac{dl}{d\theta} = \frac{2a(F)\frac{\theta}{n}\left(L^o - a(F)\frac{\theta^2}{n^2}\right) + \frac{D^2}{4} sin\left(\frac{\theta}{n}\right)}{\sqrt{\left(L^o - a(F)\frac{\theta^2}{n^2}\right)^2 - D^2 sin^2\left(\frac{\theta}{2n}\right)}}. \tag{4.3}$$

Rewriting the inelastic LADD model kinematics (3.1) as

$$L(\theta, F)_{exp} = \sqrt{\left(\frac{l_{exp}}{n}\right)^2 + D^2 sin^2\left(\frac{\theta_{exp}}{2n}\right)} \tag{4.4}$$

we know, from experimental data, the effective cell link length as a function of both LADD angle θ and load F. We then find the coefficients b_j, $j = 1, 3$, in (4.1) by curve fitting to experimental data (see Fig. 4.10).

The improvements, shown in Fig. 4.12 are dramatic: The worst case error was decreased from 18.3% full scale to 1.3% over the entire load and angle range! We

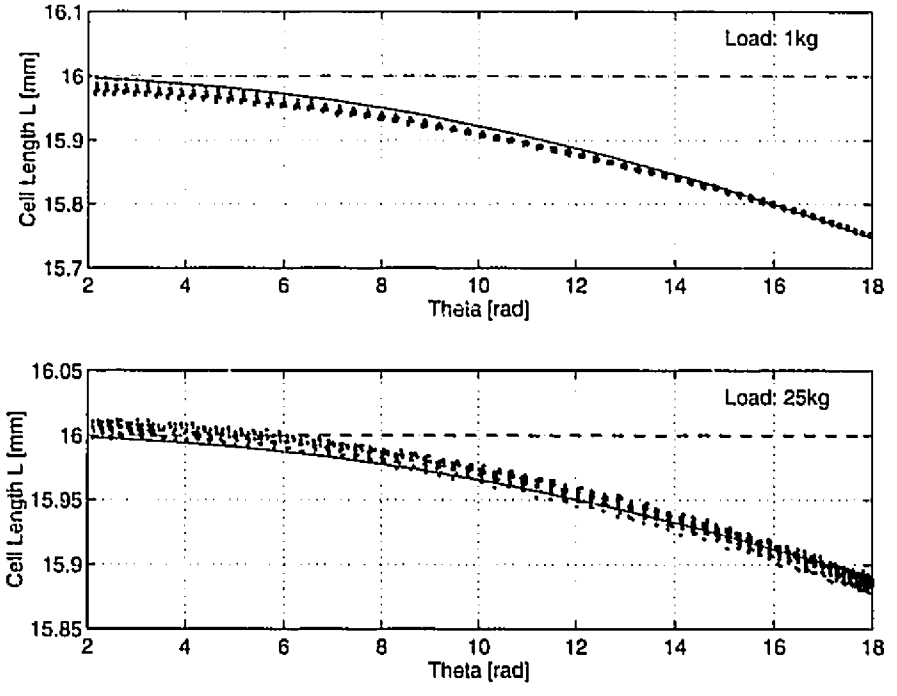

Figure 4.9: *Effective fiber link length $L(\theta, F)$ for LADD 1 from the Local Compliance Model given by (4.1) (solid curve) plotted with the inelastic model (dashed curve) and experimental data (:) for loads of $1kg$ (upper plot) and $25kg$ (lower plot).*

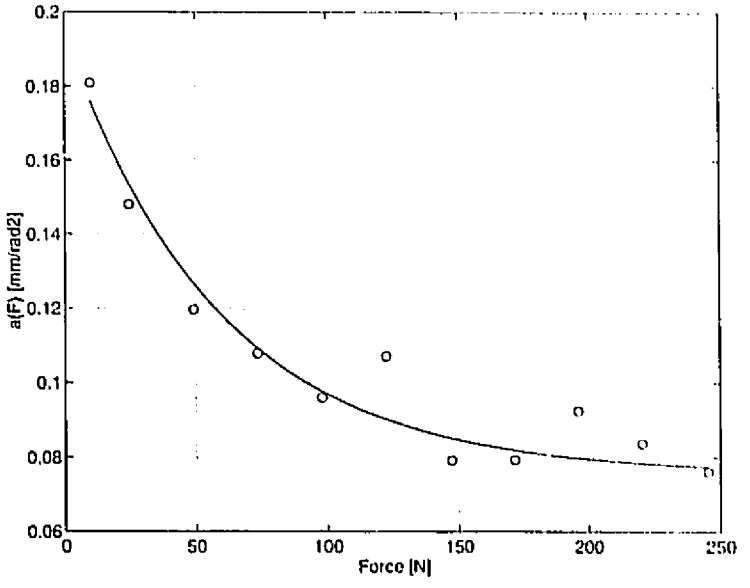

Figure 4.10: *Local Compliance Model $a(F)$ for LADD 1. The LCM identifies an effective fiber link length L given as $L(\theta, F) = L^o - a(F)(\theta/n)^2$. The data from constant load experimental runs (o) is fitted to $a(F) = b_1 exp^{b_2 F} + b_3$ (solid curve).*

have thus developed and verified an improved model, paying attention to the physical realities. Given the resulting complex model, the question arises: Can we simplify the model and still maintain accuracy? This question is answered in the next section.

4.4.2 Global Compliance Model (GCM)

The GCM identifies a global compliance term $g(F)$. It is considered "global" because it attempts to improve modeling by multiplying the overall contraction LADD length (3.2) by a factor that accounts for fiber bending as a function of LADD loading. Unlike the LCM, the GCM is developed after the inelastic model is developed, and is of the form

$$\Delta l(\theta, F) = \Delta l(\theta)_{inelastic}\, g(F) \tag{4.5}$$

where

$$g(F) = a_1 exp^{a_2 F} + a_3 \tag{4.6}$$

and the coefficients a_j, $j = 1,3$, are determined using curve fits to experimental data (see Fig. 4.11). We derive the lead r, with $\mu = 1$, as

$$r(\theta, F) \stackrel{\text{def}}{=} \frac{\tau}{F} = -\frac{dl}{d\theta} = \frac{D}{2} sin\left(\frac{\theta}{2n}\right) g(F). \tag{4.7}$$

For each constant load run, we used the experimental data and inelastic model predictions with least squares to evaluate a single value for $g(F)$ for (4.5). By evaluating respective $g(F)$s for various loads, the coefficients to (4.6) were evaluated through curve fitting. The results for the simplified GCM are shown in Fig. 4.12. Surprisingly, with 1.5% error the accuracy is only minimally worse than that of the physically motivated and more complex LCM. Therefore, we prefer to use the simpler GCM for further modeling efforts.

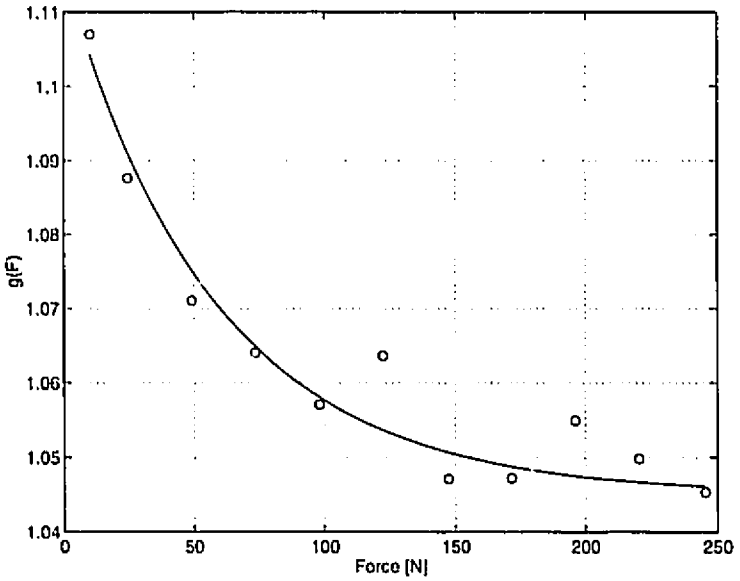

Figure 4.11: *Global Compliance Model $g(F)$ for LADD 1. The GCM accounts for inelastic LADD modeling errors by multiplying (3.2) by $g(F)$. The data from constant load experimental runs (o) is fitted to $g(F) = a_1 exp^{a_2 F} + a_3$ (solid curve).*

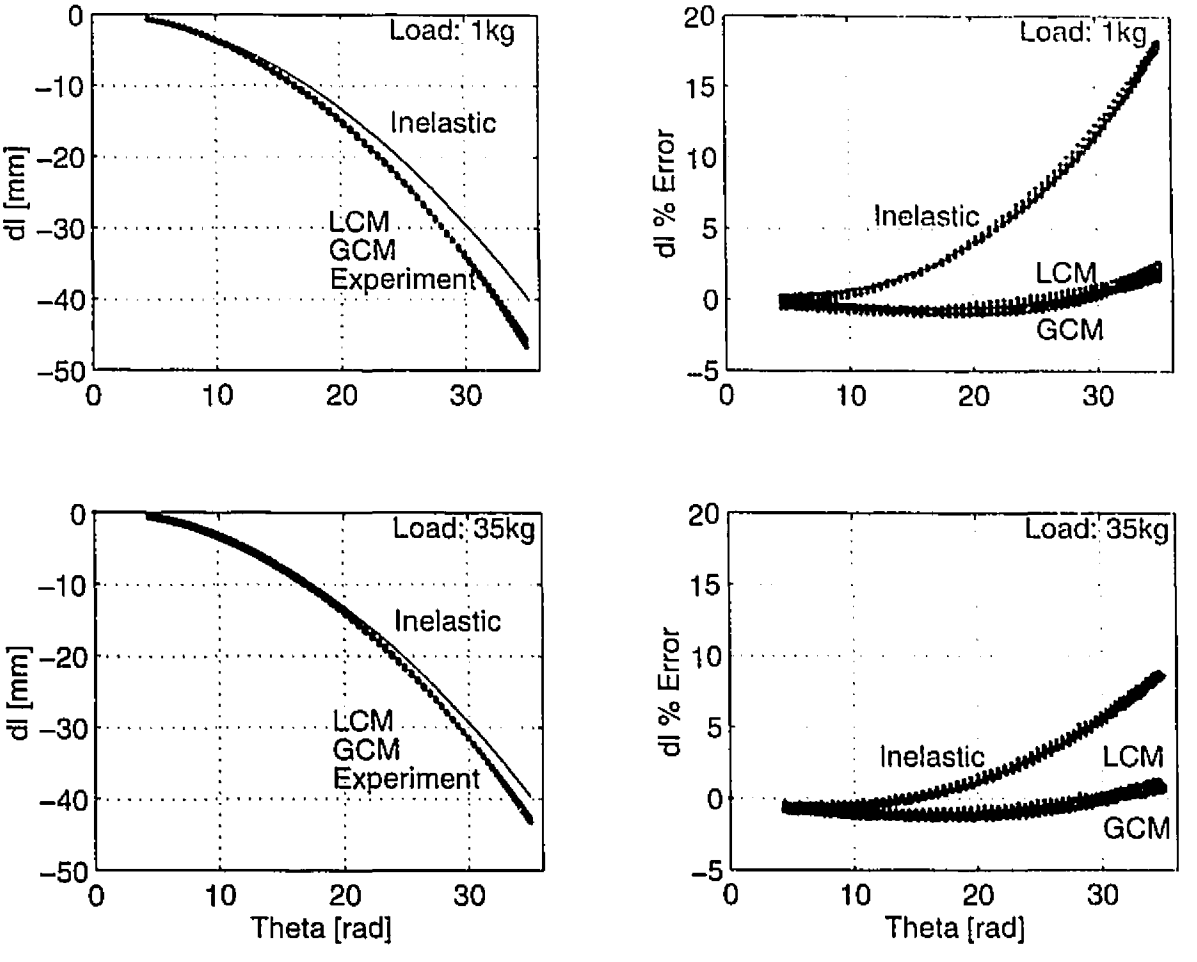

Figure 4.12: *LADD 4 Kinematics. The experimental contraction dl of LADD 4 (:)(lower curves) is plotted against the inelastic LADD model (solid curve) given by (3.2). LADD 4 had a maximum full scale model difference of 18.3% at a 1kg load (upper plots) and 9.2% at a 35kg load (lower plots). We notice that as the motor angle θ increases, the magnitude of error increases as well and in contrast, as the load F increases, the error reduces. In the left plots, both LCM and GCM models are indistinguishable from the experimental data. The error plots on the right show an error reduction down to 1.5% full scale independent of the applied load.*

4.5 New CLADD Model

The new CLADD model is based on the GCM (CGCM) and is developed in a similar manner as the inelastic model presented in Sec. 3.1.2. However, due to the number and complexity of the equations involved, a purely numerical relationship between the external load F, motor torque τ, the CLADD contraction Δl and total input angle θ, is derived.

From (4.5), assuming the outer and inner LADDs are made to be of equal length at zero relative rotation, the change in length for each LADD is given as

$$\Delta l_i(\theta_i, F_i) = \left[n_i D_i \sqrt{\mu_i^2 - sin^2\left(\frac{\theta_i}{2n_i}\right)} - n_i L_i \right] g_i(F_i) \tag{4.8}$$

and

$$\Delta l_o(\theta_o, F_o) = \left[n_o D_o \sqrt{\mu_o^2 - sin^2\left(\frac{\theta_o}{2n_o}\right)} - n_o L_o \right] g_o(F_o). \tag{4.9}$$

Equating the contraction length of the inner to that of the outer and giving both LADDs an aspect ratio of unity, simplifies to

$$\left[\cos\left(\frac{\theta_i}{2n_i}\right) - 1\right] g_i(F_i) = \left[\cos\left(\frac{\theta_o}{2n_o}\right) - 1\right] g_o(F_o). \tag{4.10}$$

Unlike the simple CLADD model presented in Sec. 3.1.2, we are not able to obtain a simple relation between θ_i and θ_o. As before, the total input rotation θ of the driving source, the motor, is shared by both LADDs,

$$\theta = \theta_i + \theta_o. \tag{4.11}$$

In addition, we have

$$F = F_i + F_o. \tag{4.12}$$

As with the inelastic model, the load distribution over the two CLADDs can be derived from the principle of virtual work, $dW_k = F_k dl_k + \tau d\theta_k = 0$, and the derivative of Equations 4.8 and 4.9, $dl/d\theta_k$, $k = i, o$, as

$$F_i = \frac{2\tau}{D_i \sin\left(\frac{\theta_i}{2n_i}\right) g_i(F_i)} \tag{4.13}$$

and

$$F_o = \frac{2\tau}{D_o \sin\left(\frac{\theta_o}{2n_o}\right) g_o(F_o)}. \tag{4.14}$$

To verify the model, we solve numerically the set of equations (4.10), (4.11), (4.12), and either (4.13) or (4.14), with experimental data for load F, input torque τ and input rotation θ to get CLADD displacement Δl. The results are shown in Fig. 4.13. For large loads of $50kg$ both the inelastic model (3.13), as well as our new CLADD model (CGCM) derived from the two LADDs' GCM model are within 4% of the experimental data. But again, just like with the individual LADDs, the differences increase with decreasing load, since the fiber bending effect is increasing. At a load of $10kg$, for example, the inelastic CLADD model results in a worst case error of 20%. In contrast, with our new model, the error is substantially reduced, and remains bounded to within 5%.

A global CLADD model could be identified, which might match the experimental data even better. However, such a model would not allow us to derive the load distribution for individual LADDs (Equations 4.13 and 4.14), which is necessary to monitor the individual LADD's operating conditions. On the other hand, one might ask why our model is not predicting the CLADD response better, being built upon LADD models which are accurate to within 1.5%. Besides the additive nature of both LADD models' inaccuracies, the main cause can almost certainly be attributed to our novelty to LADD manufacturing: the inner LADD is a small amount longer than the outer LADD ($\approx 1mm$ or 0.4%) – the CLADD thus violates assumption (3.7). A better match between inner and outer LADD length should further improve our model's accuracy.

The new CLADD model might lead to advantages in the design of ATLAS. First, compliance in the two antagonistic CLADDs alleviates the need for a highly accurate VRP. Second, the model can be used to calculate bounds on the internal force

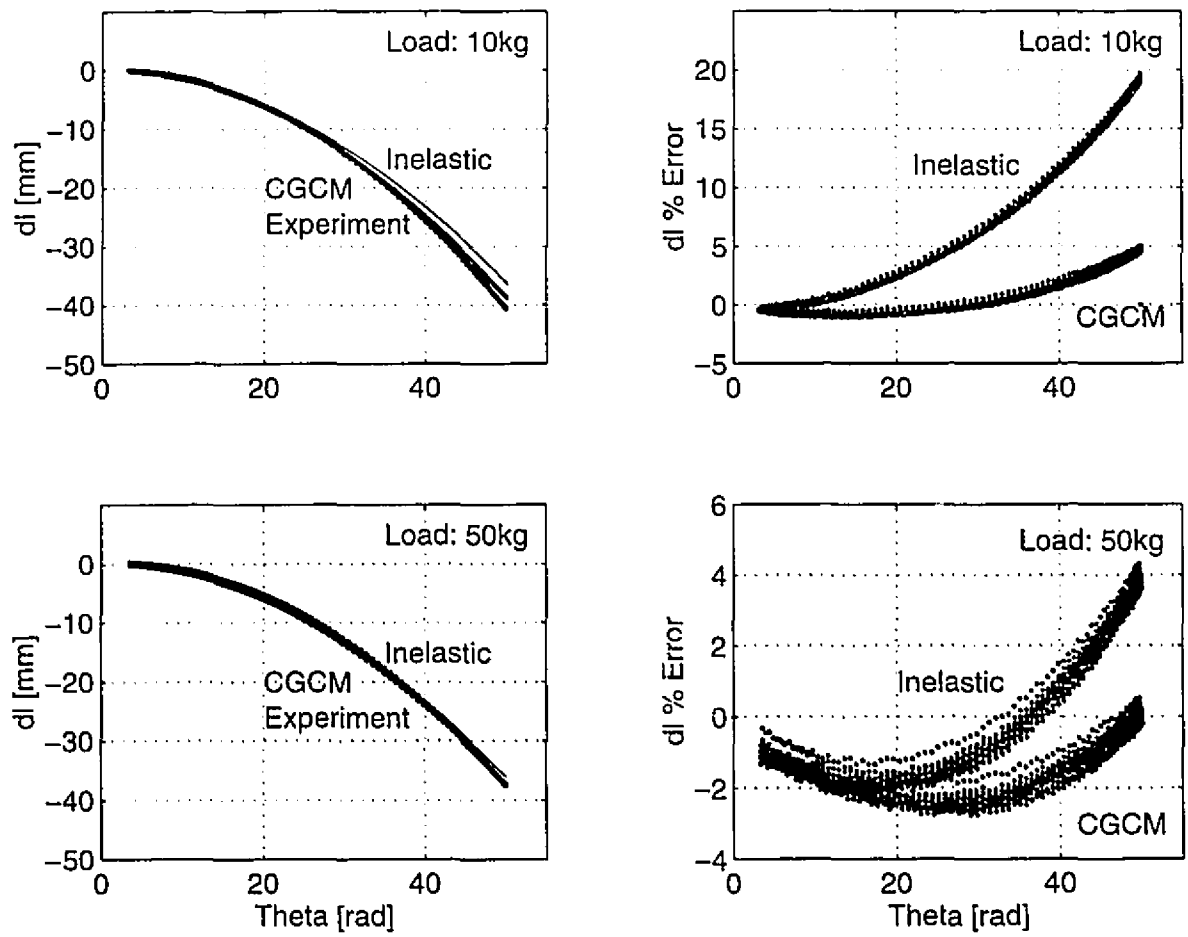

Figure 4.13: *CLADD 1 Kinematics. The inelastic CLADD model (solid curve) given by (3.13) is plotted together with experimental contraction dl of a CLADD (:)(lower curves) and our new model (CGCM)(:)(top curves) based on the individual LADDs' GCM. For large loads of 50kg both the inelastic model (3.13), as well as our new CLADD model are within 4% of the experimental data. But again, just like with the individual LADDs, the differences increase with decreasing load, since the fiber bending effect is increasing. At a load of 10kg, for example, the inelastic CLADD model results in a worst case error of 20%. In contrast, with our new model, the error is substantially reduced, and remains bounded to within 5%.*

necessary to keep the system from going slack.

4.6 CLADD Efficiency

One of the key figures of merit of a transmission is its efficiency. Referring to Figures 3.13 and 4.1, we define the overall CLADD efficiency as the total output useful work in the form of weight displacement Fdl, over the total input motor work $\tau d\theta$,

$$\eta = \frac{W_{out}}{W_{in}} = \frac{F\int^{l} dl}{\int^{\theta} \tau d\theta}. \tag{4.15}$$

The efficiencies of both knee CLADDs (see Table 3.1) for increasing load using the experimental model validation data are given in Fig. 4.14. Average efficiencies over full contractions of CLADD 1 varied from 88% for a $5kg$ load to 93% for a $50kg$ load, with similar results for CLADD 2. Efficiency increased with load because system friction plays a smaller role at higher loads. At low loads, a larger portion of the motor torque is used to overcome friction. These efficiency results of CLADDs place them within those of traditional devices: standard harmonic drive gearing efficiencies are normally in the $80 \sim 90\%$ range [1, 4] and ball screws under normal operation offer $90 \sim 95\%$ [2].

4.7 LADD Manufacturing Repeatability

To simplify modeling we look to improving the manufacturing repeatability of LADDs and CLADDs. This will replace the need to "fingerprint" every LADD manufactured, with a generic LADD model which is a function of system variables L, D, n, and d. We establish LADD manufacturing repeatability with the results of the LADD GCM given in Sec. 4.4.2. Fig. 4.15 plots the GCM coefficient $g(F)$ for LADDs 1 through 4. LADDs of identical system variables (see Table 3.1), should illustrate similar curves. Curves for LADDs 1 and 3 overlap but do not illustrate the same decay for increasing

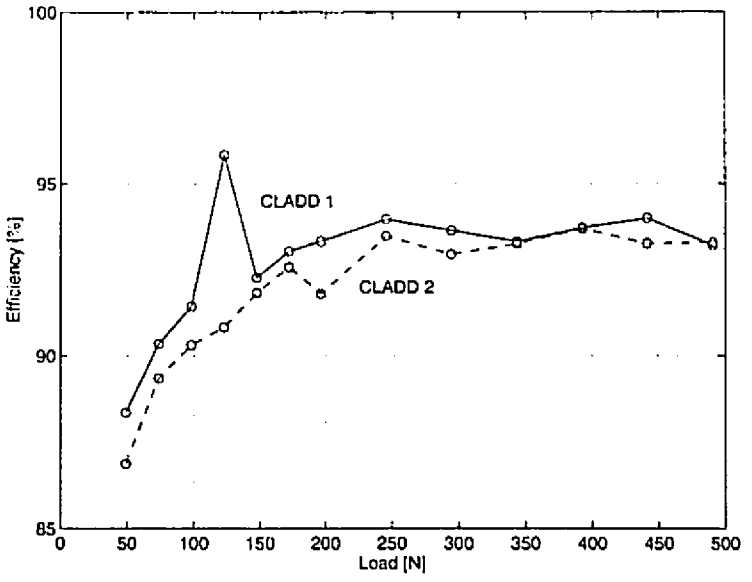

Figure 4.14: *Load dependent CLADD efficiency.*

load. On the other hand, LADDs 2 and 4 exhibit similar decays but the curves are offset considerably.

Short term operation of LADDs has shown that there are problems with LADD fiber creep and glue shaping, (see Sec. 4.2.2). But at the heart of the problem may lie our manufacturing technique. We identify two areas of concern. First, there is the application of epoxy to bond the *Spectra*® fibers to the rings and end pieces. It is left up to the steady hand of the operator and his sharp eye to determine whether the right amount of epoxy is applied to the ring: too much or too little? In the four LADDs tested, a total of 8 end pieces and 86 rings were applied with epoxy. Repeatability is extremely problematic with manual application. This is especially so for the smaller inner LADDs 2 and 4, where the densely packed links around the rings make it difficult to apply epoxy effectively. In many instances the epoxy had a tendency to run off the rings and up the fibers. Our 8*mm* diameter inner LADDs were very difficult to build for this reason, and the results in Fig. 4.15 illustrate the inconsistencies. Second, there is the equal spacing of links around each ring. The holes in the end pieces help to maintain this spacing locally. However, in the mid-section

of the LADD, the fibers tend to wander off during the epoxy application. Again this problem is most pronounced with the inner LADDs.

In conclusion, inconsistencies among inner LADDs are attributed to manufacturing issues where the small cell diameters make link spacing and epoxy application difficult. A remedy to this is to move away from small cell diameter LADDs ($\leq 8mm$) and use larger ones ($\geq 10mm$) or use a fewer number of links (≤ 20). The outer LADD inconsistencies derive from the break-in phenomena of fiber creeping and glue shaping that affect all LADDs.

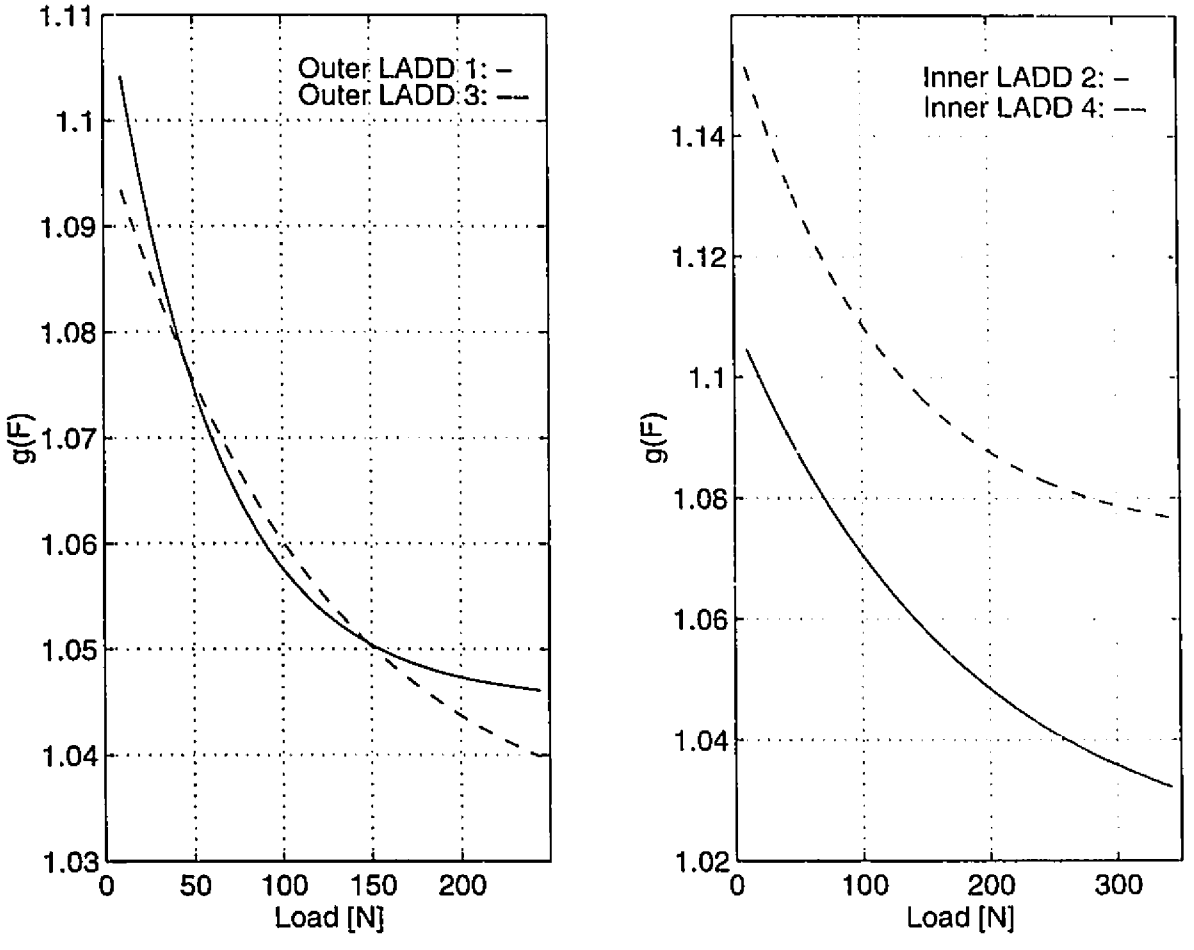

Figure 4.15: *Using the GCM to evaluate LADD manufacturing repeatability.*

Chapter 5

Conclusion

The subject of this thesis is CARL: a new articulated leg prototype, targeted for an electrically actuated, autonomous quadruped. It consists of three limbs - an upper leg, lower leg and a foot, with four degrees of freedom - an unactuated ankle, a knee, a hip and a lateral joint. CARL's key feature is ATLAS, a LADD based actuation package that integrates along robot limbs in a similar fashion as muscles do in biological systems. ATLAS exploits small $80W$ DC motors, weighing $1.3kg$ to provide more than $60Nm$ peak torque at the knee and hip joints. The current knee and hip packages, without motors, weigh $0.9kg$ and $1kg$ respectively, a favourable comparison to the $1.2kg$ harmonic drive lateral actuation. When considering the quadruped, this reflects a mass savings of $2kg$ with considerable reduction in leg inertia due to motor positioning.

Since LADDs are not commercially available, I had to construct my own. Despite the difficulties encountered, I felt my ability to customize these devices to changing future needs was well worth the investment. I have described my manufacturing process which is readily duplicatable and shown experimental data. In addition, I have selected LADD design parameters according to the simulation of a planar two-legged compliant robot to meet ATLAS torque ratios of 50 : 1. Current concentric LADDs employed in the knee ATLAS weigh $\approx 72g$ and can displace a $50kg$ load

through a $40mm$ excursion with 93% efficiency.

Based on experimental work with LADDs, I have identified a substantial error between the traditionally used inelastic kinematic model based on a simple geometric derivation and the experimentally observed data. I have identified the underlying effect to be not fiber elasticity, but fiber bending. Two new compliance models, a Local Compliance Model (LCM) and a Global Compliance Model (GCM) were introduced, the first modeling the fiber bending effect explicitly. Both models resulted in a reduction of the worst case error by an order of magnitude for LADDs.

These improvements were achieved despite some effects which limit LADD modeling accuracy. First, while *Spectra*®, is extremely durable and has negligeable compliance for cell links, it exhibits a persistent creep rate. Second, glue shaping of the epoxy that bonds the links to the rings and end pieces has a similar effect on the LADD kinematic model. Both of these effects are extremely slow but will have to be eliminated for long term operation. Finally, the manufacturing tolerances have to be kept tight, particularly for concentric LADDs, where the model predictions depend critically on the inner and outer LADDs matching lengths. These challenges may explain why these devices have not been used in the past.

With our improved knowledge about LADDs' properties, their manufacturing challenges, and more accurate models, these interesting devices could find many applications in electrically actuated autonomous systems or any other motion control application where mass is critical and suitable space is available.

Future Work

Before control work on a CARL based quadruped can begin, improvements should be carried out on two areas of design. First, to satisfy quadruped specifications, CARL's mass is to be reduced to $8kg$. A first step includes a review of the materials used for various mechanical components such as gears, joint shafts and bushings. Material substitutions for these components are given in Appendix D and save $0.9kg$

per leg. Prof. L. Lessard of McGill's Composites Laboratory proposes to substitute the aluminum limbs with graphite-epoxy ones for further mass reduction. An additional savings of $0.7kg$ is achieved with modifications to the control electronics combined with removing the heat sinks from the servo amplifiers, using the body and limbs as substitutes.

The most significant mass savings results from replacing the current *Maxon 2260* motors with *Inland 1203*. The same torque-speed characteristics are available with mass savings in the order of $2.2kg$ per leg and $8.8kg$ for the quadruped. Provisions have been made in CARL's design to incorporate these motors. At this point ARL must decide as to whether the mass savings outweigh the cost of these motors ($1200). As it stands, the cheaper ($390) but heavier ($1.3kg$) *Maxon* motors are doing a fine job.

Second, improved LADD design for reliable long term ATLAS modeling requires alternatives to *Spectra*® which show less long term creep. *Kevlar*® is a possible solution at the expense of durability. In addition, to reduce glue shaping a tougher epoxy than *CIBA-GEIGY Araldite*® must be used. Improvements in LADD manufacturing repeatability require larger cell diameters ($\geq 10mm$) or fewer cell links (≤ 20). Further, superior dynamic operation of CLADDs can be achieved by substituting aluminum for the stainless steel end pieces and graphite-epoxy for the aluminum rings, reducing current LADD mass by 50%.

Besides these design changes, future work needs to address some unanswered questions. What is the cause of LADD knotting and how can it be modeled? How does LADD cell link fiber bending effect the onset of IFI? How can the improved CLADD compliance model be exploited in the VRP design for ATLAS? It is apparent that CARL, along with ATLAS, offers a virtually non-exhaustible platform for the study of dynamic legged locomotion design and control, that ARL can exploit for time to come.

Bibliography

[1] *Cup and Pancake Component Gear Sets.* Harmonic Drive, Wakefield, MA, 1989.

[2] *Linear Motion Products.* NSK Corporation, Ann Arbor, MI, 1989.

[3] *XP/DCS CPU/MOD Rev. B Technical Manual.* Evergreen Design, Branford, CT, 1989.

[4] *Cup Type HDUC and HUC Component Sets.* HD Systems, Inc., Hauppauge, NY, 1994.

[5] Interelectric AG. *Maxon Motor.* Sachseln, Switzerland, 1993/94.

[6] R. McN. Alexander. Elastic energy stores in running vertebrates. *American Zoologist*, 24:85–94, 1984.

[7] R. McN. Alexander. *Elastic Mechanisms in Animal Movements.* Cambridge University Press, Cambridge, 1988.

[8] R. McN. Alexander. Three Uses for Springs in Legged Locomotion. *Int. J. Robotics Research*, 9(2):53–61, 1990.

[9] R. McN. Alexander and G. Goldspink. *Mechanics and Energetics of Animal Locomotion.* Chapman and Hall, London, 1977.

[10] J. F. Blackburn, G. Reethof, and J. L. Shearer. *Fluid Power Control.* The Technology Press of MIT and John Wiley and Sons, NY and London, 1960.

[11] B. Boulet and V. Hayward. Robust control of a robot joint with hydraulic actuator redundancy. Technical Report TR-CIM-93-6, McGill University, Montréal, Canada, 1993.

[12] J. C. Carruth. Operations characteristics of the LADD actuator. M. Eng. Thesis, University of Utah, 1975.

[13] A. Nahvi et al. An investigation of the transmission system of a tendon driven robot hand. In *Proc. IEEE/RSJ Conf. Intelligent Systems and Robots*, pages 202–208, Munic, Germany, Sep 1994.

[14] P.K. Freakley and A.R. Payne. *Theory and Practice of Engineering with Rubber.* Applied Science Pub., London, 1978.

[15] J. Gray. *How Animals Move.* Cambridge University Press, Cambridge, 1953.

[16] P. Grégoire. Elastomeric torsional springs. Technical report, McGill University, Montréal, Canada, 1995 (to appear).

[17] P. Grégoire, T. Marincic, and O. Payant. CARL: Compliant Articulated Robotic Leg. Design V Final Report, McGill University, Apr 1994.

[18] P. Gregorio. Design, control and energy minimization strategies for an electrically actuated legged robot. M.Eng. Thesis, McGill University, Aug 1994.

[19] S. C. Jacobsen. Rotary-to-linear and linear-to-rotary motion converters. US Patent 3864983, 1975.

[20] S. C. Jacobsen and R. B. Jerrard. Torsion of Rope-Connected Hoops Leads to Light Weight Prosthetic Actuator. In *26th ACEMB*, Sep 1973.

[21] S. C. Jacobsen, R. B. Jerrard, and D. Knutti. Preliminary Report on the Utah Arm. In *Conference on Engineering Devices in Rehabilitation*, Boston, MA, May 1974.

[22] S. C. Jacobsen, R. B. Jerrard, D. Knutti, and J. Carruth. The Ladd Actuator as a Prosthetic Muscle. In *Proc. of 5th Int. Symp. on External Control of Human Extremities*, Dubrovnik, Yugoslavia, Aug 1975.

[23] Z. J. Lansky and L. F. Schrader. *Industrial Pneumatic Control.* Marcel Dekker, NY, 1986.

[24] D. McCloy and H. R. Martin. *The Control of Fluid Power.* John Wiley and Sons, NY, 1973.

[25] T. A. McMahon. *Muscles, Reflexes, and Locomotion.* Princeton University Press, Princeton, 1984.

[26] M. M. Moghaddam. A planar virtual motion system for legged robots. M.Eng. Project Report, McGill University, Apr 1993.

[27] E. Muybridge. *Animals in Motion.* Dover Publications, Inc., NY, NY, 1957.

[28] CTV National News. Leading Edge, Aug 10, 1994.

[29] G. Pahl and W. Beitz. *Engineering Design.* Design Council, London, 1984.

[30] K. V. Papantoniou. Control architecture for an electrical, actively balanced multi-leg robot, based on experiments with a planar one leg machine. In *IFAC*, Vienna, Austria, 1991.

[31] K. V. Papantoniou. Electromechanical design for an electrically powered, actively balanced one leg planar robot. In *Proc. IEEE/RSJ Conf. Intelligent Systems and Robots*, Osaka, Japan, 1991.

[32] K. V. Papantoniou. Experiments concerning the power efficiency during locomotion of an electrical, actively balanced one-leg planar robot. In *Fourth World Conf. on Robotics Research*, Pittsburg, Pennsylvania, Sep 1991. RI/SME.

[33] K. L. Pottebaum and J. J. Beaman. A dynamic model of a concentric LADD actuator. *ASME J. Dynamics Systems, Measurement, and Control*, 105:157–164, Sep 1983.

[34] H. Rad, P. Gregorio, and M. Buehler. Design, modeling and control of a hopping robot. In *Proc. IEEE/RSJ Conf. Intelligent Systems and Robots*, pages 1778–1785, Yokohama, Japan, Jul 1993.

[35] M. H. Raibert. *Legged Robots That Balance*. MIT Press, Cambridge, MA, 1986.

[36] M. H. Raibert. Legged robots. In P. H. Winston and S. A. Shellard, editors, *Artificial Intelligence at MIT*, pages 149–179. MIT Press, Cambridge, MA, 1990.

[37] G. J. Zeglin. Uniroo: A one legged dynamic hopping robot. B. Sc. Thesis, MIT, May 1991.

Appendix A

Nomenclature

Parameter	Description	Units
τ	LADD torque (fig. 3.2)	Nm
F	LADD axial load (fig. 3.2)	N
D	LADD cell diameter (fig. 3.4)	m
L	LADD cell length (fig. 3.4)	m
θ	LADD input rotation (fig. 3.4)	rad
w	LADD cell ring width (fig. 3.4)	m
t	LADD cell ring thickness (fig. 3.4)	m
l	LADD length (3.1)	m
n	number of LADD cells (3.1)	
μ	LADD cell aspect ratio: L/D (3.1)	
Δl	LADD length change (3.2)	m
r	LADD mechanical lead (3.3)	m/rad
m	LADD mechanical advantage (3.4)	
d	LADD cell link diameter (3.5)	m
α	spacing of LADD links around cell rings (3.5)	rad
c	number of LADD cell links (3.5)	
τ_i	LADD input torque (fig. 3.13)	Nm
τ_o	VRP output torque (fig. 3.13)	Nm
R	VRP radius (fig. 3.13)	m
ϕ	VRP angle (fig. 3.14)	rad
γ	angle between *Base* and R (fig. 3.14)	rad
β	angle between *Arm* and *Base* (fig. 3.14)	rad
Base	perp. distance from CLADD beginning to VRP center (fig. 3.14)	m
Offset	perp. distance from *Base* to CLADD beginning (fig. 3.14)	m
Arm	distance from center of VRP to CLADD beginning (fig. 3.14)	m
m	slope (3.18)	
b	y intercept (3.19)	m
(X, Y)	VRP surface coordinates (3.20)	m
L^o	design LADD cell length (4.1)	m
$a(F)$	LCM coefficient (4.1)	rad^{-2}
$b_j,\ j = 1,3$	coefficients to $a(F)$ (4.1)	
$g(F)$	GCM coefficient (4.5)	
$a_j,\ j = 1,3$	coefficients to $g(F)$ (4.6)	
η	CLADD efficiency (4.15)	
W	total work (4.15)	Nm

Table A.1: *Nomenclature (in order of appearance).*

Acronym	*Description*
CARL	Compliant Articulated Robot Leg
ATLAS	AnTagonistic LADD Actuation System
LADD	Linear-to-Angular Displacement Device
CLADD	Concentric LADD
VRP	Variable Radius Pulley
LCM	Local Compliance Model
GCM	Global Compliance Model
CGCM	CLADD GCM

Table A.2: *Acronyms (in order of appearance).*

Appendix B

CARL Parts List

Part No.	Description	Qty	Material	Mass [g]
1	Integrated Transputer w/ IO	1	Stock	450
2	M3x12 Hexagonal Cap Screw	15	Stock	13
3	15*mm* ϕ Shaft Retaining Ring	1	Stock	1
4	ATLAS NX 7 Z Bearing Bushing	4	Stainless Steel	168
5	CLADD Outer Motor End Piece	4	Stainless Steel	*
6	Pulley Tightening Bolt	4	Stainless Steel	48
7	Hip Variable Radius Pulley	1	Aluminum 6061-T6	77
8	M8 Washer	4	Stock	6
9	M8 Nut	4	Stock	18
10	M5x12 Hexagonal Cap Screw	10	Stock	28
11	Lateral HK 1412 Bearing Housing	1	Aluminum 6061-T6	130
12	M6x8 Dog Point Setscrew	3	Stock	3
13	Lateral Hard Stop	1	Aluminum 6061-T6	78
14	5x5x20 Key	1	Key Stock	4
15	A.M.C. 25A PWM Servo Amplifier	3	Stock	846
16	M4x12 Hexagonal Cap Screw	8	Stock	14
17	HTD Timing Belt Pulley	2	Aluminum Alloy	102
18	Maxon 2260 80 Watt DC Motor	3	Stock	3780
19	Makeshift Body	1	Aluminum 6061-T6	†
20	Harmonic Drive Input Housing	1	Aluminum 6061-T6	242
21	HTD Timing Belt Pulley Flange	2	Aluminum	6
22	HTD Timing Belt	1	Neoprene	18
23	Lateral Hip Shaft	1	Steel 4340 HT	270
24	M4 Washer	2	Stock	1
25	M4x8 Hexagonal Cap Screw	2	Stock	3
26	Hip Spring: Right End Plate	1	Aluminum 6061-T6	*
27	Torsional Compliance	3	Elastomer	*
28	Hip Spring: Left End Plate	1	Aluminum 6061-T6	*
29	HK 1512 Bearing	1	Stock	11
30	HK 1516 Bearing	2	Stock	30
31	Dummy Force Sensor	4	Stainless Steel	*
32	M8x30 Hexagonal Cap Screw	2	Stock	30
33	A 7Y16-2 Guide Wheels	2	Stainless Steel	79
34	Upper Limb	1	Aluminum 6061-T6	581
36	Bearing Cap	3	Aluminum 6061-T6	72
37	Knee Shaft	1	Steel 4140 Q&T	108
38	CP-2FK(B) Angle Sensor	5	Stock	75
39	M2x6 Setscrew	5	Stock	1
40	12*mm* ϕ Shaft Retaining Ring	4	Stock	1
41	NKIB 5901 Bearing	3	Stock	129

Table B.1: *CARL parts list: 1 of 3. Numbered parts are illustrated in Figures 2.7, 2.8 and 3.16. (*Mass included as an assembly. †Mass not included. ‡Not available.)*

Part No.	Description	Qty	Material	Mass [g]
42	NK1B 5901 Bushing	2	Stainless Steel	50
43	Lower Limb	1	Aluminum 6061-T6	555
44	Ankle Spring: Left End Plate	1	Aluminum 6061-T6	*
45	M6 Washer	9	Stock	8
46	M6x16 Hexagonal Cap Screw	14	Stock	76
47	Ankle Spring: Right End Plate	1	Aluminum 6061-T6	*
48	Ankle Index Coupling	1	Aluminum 6061-T6	≈30
49	4x4x15 Key	1	Key Stock	1
50	M5x10 CSK Cap Screw	8	Stock	14
51	HK 1212 Bearing	1	Stock	9
52	HK 1212 Bushing	1	Stainless Steel	37
53	Toe w/ Switch	1	Stock	32
54	HK 1412 Bearing w/ IR 10x14x13	1	Stock	18
55	Foot	1	Aluminum 6061-T6	149
56	Ankle Shaft	1	Steel 4140 Q&T	94
59	Knee Variable Radius Pulley	1	Aluminum 6061-T6	89
60	Knee Spring: Left End Plate	1	Aluminum 6061-T6	*
61	NX 10 Z Bearing	1	Stock	25
62	10mm ϕ Shaft Retaining Ring	2	Stock	2
63	HK 1516 Bushing	1	Stainless Steel	46
64	Knee Spring: Right End Plate	1	Aluminum 6061-T6	*
65	M4x12 CSK Cap Screw	3	Stock	4
66	136.4kg Line	na†	Spectra® Fiber	*
67	Sensor to Fiber Connector	4	Stainless Steel	*
68	CLADD Outer Rotating End Piece	4	Stainless Steel	*
69	HP HEDS-6010 Optical Encoder	3	Stock	210
70	22.7kg Line	na†	Spectra® Fiber	*
71	CLADD Outer Ring	50	Aluminum 6061-T6	*
72	CLADD Inner Ring	104	Aluminum 6061-T6	*
73	Hip Bushing	1	Stainless Steel	61
74	Hip Fore-Aft Shaft	1	Steel 4140 Q&T	197
75	ATLAS Housing	1	Aluminum 6061-T6	329
76	ATLAS Housing Cover	1	Plexiglass	141
77	Electronic Board Supports	2	Plexiglass	52
78	M4x16 Hexagonal Cap Screw	2	Stock	4
79	Harmonic Drive Input Shaft	1	Stainless Steel	34
80	M4x10 Setscrew	2	Stock	1
81	3200 ZZ Bearing	1	Stock	52
82	30mm ϕ Bore Retaining Ring	1	Stock	2

Table B.2: *CARL parts list: 2 of 3. Numbered parts are illustrated in Figures 2.7, 2.8 and 3.16. (*Mass included as an assembly. †Mass not included. ‡Not available.)*

Part No.	Description	Qty	Material	Mass [g]
83	M3x30 Hexagonal Cap Screw	12	Stock	21
84	3x3x15 Key	1	Key Stock	1
85	HD CSF-20-160-2A-GR	1	Stock	227
86	$9mm\ \phi$ Shaft Retaining Ring	1	Stock	1
87	M5x10 Hexagonal Cap Screw	8	Stock	22
88	Harmonic Drive Clamp Ring	1	Stainless Steel	6
89	$35mm\ \phi$ Bore Retaining Ring	1	Stock	3
90	Harmonic Drive Output Housing	1	Aluminum 6061-T6	364
91	3202 ZZ Bearing	1	Stock	72
92	3x12 Dowel Pin	2	Stock	1
93	6x10 Dowel Pin	4	Stock	8
94	$30mm\ \phi$ Fairloc® Spur Gear	2	Stainless Steel	78
95	M5 Washer	8	Stock	3
96	ATLAS Shaft	4	Stainless Steel	78
97	$60mm\ \phi$ Hubless Spur Gear	4	Stainless Steel	220
98	M5x20 CSK Cap Screw	6	Stock	17
99	CLADD Inner Motor End Piece	4	Stainless Steel	*
100	CLADD Inner Rotating End Piece	4	Stainless Steel	*
101	Model 31 Force Sensor	4	Stock	†
102	M5x31 Shoulder Bolt	1	Stock	9
103	M2.5x8 Hexagonal Cap Screw	10	Stock	4
104	Angle Sensor Clip	10	Stock	1
105	M4 Nut	2	Stock	2
106	M3x8 Hexagonal Cap Screw	16	Stock	12
107	$14mm\ \phi$ Shaft Retaining Ring	4	Stock	1
108	NX 7 Z TN Bearing	4	Stock	56
109	Flanged Ball Bearing	4	Stock	11
110	M6x20 Hexagonal Cap Screw	6	Stock	36
111	Guide Wheel Bushing	2	Stainless Steel	17
	Assembled Knee CLADD	2	Parts: 5,31,66,67, 68,70,71,72,99,100	144
	Assembled Hip CLADD	2	Parts: 5,31,66,67, 68,70,71,72,99,100	130
	Assembled Ankle Torsional Spring	1	Parts: 27,44,47	≈125
	Assembled Knee Torsional Spring	1	Parts: 27,60,64	125
	Assembled Hip Torsional Spring	1	Parts: 26,27,28	≈125
CARL Total Mass	$\approx 11.7kg$			

Table B.3: *CARL parts list: 3 of 3. Numbered parts are illustrated in Figures 2.7, 2.8 and 3.16. (*Mass included as an assembly. †Mass not included. ‡Not available.)*

Appendix C

CARL Costs

Part No.	Description	Qty	Unit Price		Total	
1	Integrated Transputer w/ IO	1	2000.00		2000.00	
15	A.M.C. 25A PWM Servo Amplifier	3	445.00	*US*	1335.00	*US*
17	HTD Timing Belt Pulley	2	13.97	*US*	27.94	*US*
18	Maxon 2260 80 Watt Motor	3	300.65	*US*	901.95	*US*
22	HTD Timing Belt	1	9.90	*US*	9.90	*US*
29	HK 1512 Bearing	1	4.53		4.53	
30	HK 1516 Bearing	2	4.75		9.50	
33	A 7Y16-2 Guide Wheels	2	43.55	*US*	87.10	*US*
38	CP-2FK(B) Angle Sensor	5	39.00	*US*	195.00	*US*
41	NKIB 5901 Bearing	3	47.66		142.98	
51	HK 1212 Bearing	1	4.25		4.25	
54	HK 1412 Bearing w/ IR 10x14x13	1	11.60		11.60	
61	NX 10 Z Bearing	1	40.91		40.91	
66	Spectra® 136.4kg Line	91.4m	16.80	*US*	16.80	*US*
69	HP HEDS-6010 Optical Encoder	3	129.35		388.05	
70	Spectra® 22.7kg Line	304.8m	38.00	*US*	38.00	*US*
81	3200 ZZ Bearing	1	17.73		17.73	
85	HD CSF-20-160-2A-GR	1	725.00	*US*	725.00	*US*
91	3202 ZZ Bearing	1	21.56		21.56	
94	30mm ϕ Fairloc® Spur Gear	2	14.17	*US*	28.34	*US*
97	60mm ϕ Hubless Spur Gear	4	13.14	*US*	52.56	*US*
108	NX 7 Z TN Bearing	4	30.08		120.32	
109	Flanged Ball Bearing	4	11.73	*US*	46.92	*US*
	Steel 4340 Heat Treated (assorted)	na*	≈15.00		≈15.00	
	Steel 4140 Annealed (assorted)	na*	≈25.00		≈25.00	
	Aluminum 6061-T6 (assorted)	na*	≈200.00		≈200.00	
	Plexiglass (assorted)	na*	≈20.00		≈20.00	
	Fasteners (assorted)	na*	≈50.00		≈50.00	
	Harmonic Grease HC-1	0.5kg	44.00	*US*	44.00	*US*
	Polyurethane Elastomer	na*	≈50.00		≈50.00	
	CIBA-GEIGY Araldite®	206g	≈30.00		≈30.00	
	Permabond® Bonding Adhesive	28.4g	≈10.00		≈10.00	
	Machining Costs w/o LADDs	250hr	30/hr		7500.00	
	Variable Radius Pulley Machining	4hr	30/hr		120.00	
	LADD Machining	50hr	30/hr		1500.00	
	LADD Construction	32hr	10/hr		320.00	
	Quenching & Tempering	na*	120.00		120.00	
	Grinding	na*	200.00		200.00	

CARL Total Cost	≈ $17,500

Table C.1: *CARL costs dated June 1994. (Exchange rate: 1 US= 1.3 CAN. Canadian duties on imports and taxes not included. *Not available)*

Appendix D

Proposed CARL Mass Savings

Part No.	Description	Qty	Substitution	Savings [g]
1	Integrated Transputer w/ IO	1	Modify design.	225
4	ATLAS NX 10 Z Bearing Bushing	4	Aluminum 606 -T6	109
5	CLADD Outer Motor End Piece	4	Aluminum 6061-T6	"
15	A.M.C. 25A PWM Servo Amplifier	3	Remove heat sink.	450
18	Maxon 2260 80 Watt DC Motor	3	Inland 1203	2214
23	Lateral Hip Shaft	1	Titanium	108
31	Dummy Force Sensor	4	Aluminum 6061-T6	"
33	A 7Y16-2 Guide Wheels	2	Aluminum 6061-T6	≈40
37	Knee Shaft	1	Titanium	43
42	NKIB 5901 Bushing	2	Aluminum 6061-T6	32
52	HK 1212 Bushing	1	Aluminum 6061-T6	24
56	Ankle Shaft	1	Titanium	38
63	HK 1516 Bushing	1	Aluminum 6061-T6	30
67	Sensor to Fiber Connector	4	Aluminum 6061-T6	"
68	CLADD Outer Rotating End Piece	4	Aluminum 6061-T6	"
73	Hip Bushing	1	Aluminum 6061-T6	40
74	Hip Fore-Aft Shaft	1	Titanium	79
94	$30mm\ \phi$ Fairloc® Spur Gear	2	Aluminum Alloy	51
97	$60mm\ \phi$ Hubless Spur Gear	4	Aluminum Alloy	143
99	CLADD Inner Motor End Piece	4	Aluminum 6061-T6	"
100	CLADD Inner Rotating End Piece	4	Aluminum 6061-T6	"
111	Guide Wheel Bushing	2	Aluminum 6061-T6	11
	Assembled Knee CLADD	2	Replace parts: 5,31, 67,68,99,100 with Aluminum 6061-T6.	62
	Assembled Hip CLADD	2	Replace parts: 5,31, 67,68,99,100 with Aluminum 6061-T6.	62

Expected Mass Savings	$\approx 3.8kg$	32.5%
CARL New Mass	$\approx 7.9kg$	67.5%

Table D.1: *Proposed CARL mass savings. (" Mass savings included as an assembly.)*

Appendix E

VRP Program

```
% (c) G. Kermitto 1994
% Program "vrp.m"
% Generates Variable Radius Pulley for ATLAS Package
% ---------------------------------------------------

% Flow of Program
% ---------------

% (1) Get Data
%     - CLADD Variables
%     - BASE
%     - OFFSET
%     - To_Ti: Desired fixed reduction ratio

% (2) Design VRP Surface For Protagonist CLADD
%     Calculate:
%     - THETA_PROT: Integrate Torque Ratio Data
%     - dLdTHETA_PROT: Substitute THETA_PROT
%     - REFFEC_PROT: Using dLdTHETA_PROT and To_Ti
%     - LINE EQUATIONS OF CLADDs: Incrementing ARM by dPHI
%     - X_PROT and Y_PROT: Intersection of two successive LINEs

% (3) Design VRP Surface For Antagonist CLADD
%     Calculate:
%     - THETA_ANT: From THETA_PROT
%     - dLdTHETA_ANT: Substitute THETA_ANT
%     - REFFEC_ANT: Using dLdTHETA_ANT and To_Ti
%     - LINE EQUATIONS OF CLADDs: Incrementing ARM by dPHI
%     - X_ANT and Y_ANT: Intersection of two successive LINEs

% (4) Close Off VRP Surface

% (5) Miscellaneous Calculations

% (6) Assemble Vector Containing Complete VRP Surface Coordinates

% (7) Generate Milling Tool Path

% (8) Rotate VRP Surface Coordinates

% (9) Save VRP Surface Coordinates and Tool Path


% MAIN Program
% ------------

clc
clg
clear


% (1) GET DATA
%     --------

% Load ATLAS Variables
load cladd_data.data;
L_i = cladd_data(1);                % [m]
D_i = cladd_data(2);                % [m]
n_i = cladd_data(3);                % [integer]
m_i = cladd_data(4);                % number of inner LADD links
L_o = cladd_data(5);                % [m]
D_o = cladd_data(6);                % [m]
n_o = cladd_data(7);                % [integer]
m_o = cladd_data(8);                % number of outer LADD links
BASE = cladd_data(9);               % [m]
OFFSET = cladd_data(10);            % [m]
PULLEY_RANGE = cladd_data(11)*pi/180;   % [rad]
THETA_PROTo = cladd_data(12)*pi/180;    % [rad]
mu = L_i/D_i;

% Pulley Range
dPHI = 0.01;                        % [rad]
PHI = [0:dPHI:PULLEY_RANGE];
n = length(PHI);

% Gear Ratio: To_Ti
To_Ti = 25;
GEARs = 2;

% CLADD's Limited Rotation
THETA_MAX = [90*(n_i+n_o); 90*(n_i+n_o)];
PHI_MAX = [PHI(1); PHI(n)];


% (2) PROTAGONIST VRP SURFACE
%     -----------------------

dTHETAdPHI_PROT = To_Ti;

THETA_PROT = To_Ti.*(PHI-PHI(1))+THETA_PROTo;

if max(THETA_PROT)*180/pi >= THETA_MAX(1),
error('EXCEEDED CLADDs ROTATION LIMIT!!!')
end

dLdTHETA_PROT = -n_i*D_i.*sin(THETA_PROT./(n_i+n_o))...
                ./(4*(n_i+n_o).*(mu^2-(sin(THETA_PROT...
                ./(2*(n_i+n_o)))).^2).^0.5);

REFFEC_PROT = -To_Ti.*dLdTHETA_PROT;

% EQUATIONS OF LINES
m = length(REFFEC_PROT);
ARM = (BASE^2+OFFSET^2)^0.5;
BETA = atan(OFFSET/BASE);

GAMMA_PROT = acos(REFFEC_PROT./ARM);
PHI_REFFEC_PROT = GAMMA_PROT+BETA+PHI;
SLOPE_PROT = -1./(tan(PHI_REFFEC_PROT));
B_PROT = REFFEC_PROT.*(sin(PHI_REFFEC_PROT)...
           .*tan(PHI_REFFEC_PROT)+cos(PHI_REFFEC_PROT))...
           ./(tan(PHI_REFFEC_PROT));

% INTERSECTION OF TWO LINES
for j = 2:m,
X_PROT(j-1) = (B_PROT(j)-B_PROT(j-1))/(SLOPE_PROT(j-1)-SLOPE_PROT(j));
Y_PROT(j-1) = (SLOPE_PROT(j-1)*B_PROT(j)-SLOPE_PROT(j)*B_PROT(j-1))...
           /(SLOPE_PROT(j-1)-SLOPE_PROT(j));
end
```

```
% (3) ANTAGONIST VRP SURFACE
%     ----------------------

THETA_ANTo = max(THETA_PROT);
THETA_ANT = -THETA_PROT+(THETA_ANTo+THETA_PROTo);

dLdTHETA_ANT = -n_i*D_i.*sin(THETA_ANT./(n_i-n_o))...
               ./(4*(n_i-n_o).*(mu^2-(sin(THETA_ANT...
               ./(2*(n_i-n_o)))).^2).^0.5);

REFFEC_ANT = -To_Ti.*dLdTHETA_ANT;

% EQUATIONS OF LINES
n = length(REFFEC_ANT);
ARM = (BASE^2+OFFSET^2)^0.5;
BETA = atan(OFFSET/BASE);

GAMMA_ANT = acos(REFFEC_ANT./ARM);
PHI_REFFEC_ANT = -(GAMMA_ANT+BETA-PHI);
SLOPE_ANT = -1./(tan(PHI_REFFEC_ANT));
B_ANT = REFFEC_ANT.*(sin(PHI_REFFEC_ANT)...
          .*tan(PHI_REFFEC_ANT)+cos(PHI_REFFEC_ANT))...
          ./(tan(PHI_REFFEC_ANT));

% INTERSECTION OF TWO LINES
for j = 2:n,
X_ANT(j-1) = (B_ANT(j)-B_ANT(j-1))/(SLOPE_ANT(j-1)-SLOPE_ANT(j));
Y_ANT(j-1) = (SLOPE_ANT(j-1)*B_ANT(j)-SLOPE_ANT(j)*B_ANT(j-1))...
             /(SLOPE_ANT(j-1)-SLOPE_ANT(j));
end


% (4) CLOSE OFF VRP SURFACE
%     --------------------

% LINES
X_PROT_i = (B_ANT(n)-B_PROT(1))/(SLOPE_PROT(1)-SLOPE_ANT(n));
Y_PROT_i = (SLOPE_PROT(1)*B_ANT(n)-SLOPE_ANT(n)*B_PROT(1))...
           /(SLOPE_PROT(1)-SLOPE_ANT(n));

X_PROT_LINE = X_PROT_i;
Y_PROT_LINE = Y_PROT_i;

X_ANT_LINE = X_PROT_i;
Y_ANT_LINE = Y_PROT_i;

% ARC
B_PROT_arc = Y_PROT(n-1)-X_PROT(n-1)/SLOPE_PROT(n);
B_ANT_arc = Y_ANT(1)-X_ANT(1)/SLOPE_ANT(1);

X_CENTER = (B_ANT_arc-B_PROT_arc)*SLOPE_PROT(n)*SLOPE_ANT(1)...
           /(SLOPE_PROT(n)-SLOPE_ANT(1));
Y_CENTER = -X_CENTER/SLOPE_PROT(n)+B_PROT_arc;

ARC_RADIUS1 = ((X_CENTER-X_PROT(n-1))^2+(Y_CENTER-Y_PROT(n-1))^2)^0.5;
ARC_RADIUS2 = ((X_CENTER-X_ANT(1))^2+(Y_CENTER-Y_ANT(1))^2)^0.5;
ARC_RADIUS = (ARC_RADIUS1 + ARC_RADIUS2)/2;

ALPHAo = atan2((Y_PROT(n-1)-Y_CENTER),(X_PROT(n-1)-X_CENTER));
ALPHAf = atan2((Y_ANT(1)-Y_CENTER),(X_ANT(1)-X_CENTER));

if ALPHAo < 0
   ALPHAo = ALPHAo + 2*pi;
end

if ALPHAf < 0
   ALPHAf = ALPHAf + 2*pi;
end
ALPHA = [ALPHAo:dPHI:dPHI:ALPHAf-dPHI];

X_ARC = X_CENTER+ARC_RADIUS.*cos(ALPHA);
Y_ARC = Y_CENTER+ARC_RADIUS.*sin(ALPHA);


% (5) MISCELLANEOUS CALCULATIONS
%     --------------------------

BETA = atan(OFFSET/BASE);

% AVERAGE EFFECTIVE RADII
AVG_REFFEC_ANT = mean(REFFEC_ANT)*1000          % [mm]
AVG_REFFEC_PROT = mean(REFFEC_PROT)*1000        % [mm]

% CLARO LATERAL VARIATION
MIN_LV_ANGLE_PROT = -(BETA-pi/2-acos(min(REFFEC_PROT)/ARM))*180/pi  % [deg]
MAX_LV_ANGLE_PROT = -(BETA-pi/2-acos(max(REFFEC_PROT)/ARM))*180/pi  % [deg]

MIN_LV_ANGLE_ANT = -(BETA-pi/2-acos(min(REFFEC_ANT)/ARM))*180/pi    % [deg]
MAX_LV_ANGLE_ANT = -(BETA-pi/2-acos(max(REFFEC_ANT)/ARM))*180/pi    % [deg]


% (6) ASSEMBLE VECTOR CONTAINING COMPLETE VRP SURFACE COORDINATES
%     -----------------------------------------------------------

a = length(X_PROT_LINE);
b = length(X_PROT);
c = length(X_ARC);
d = length(X_ANT);
e = length(X_ANT_LINE);

X_VRP_VECTOR(1:a) = X_PROT_LINE(1:a);
Y_VRP_VECTOR(1:a) = Y_PROT_LINE(1:a);

X_VRP_VECTOR(a+1:a+b) = X_PROT(1:b);
Y_VRP_VECTOR(a+1:a+b) = Y_PROT(1:b);

X_VRP_VECTOR(a+b+1:a+b+c) = X_ARC(1:c);
Y_VRP_VECTOR(a+b+1:a+b+c) = Y_ARC(1:c);

X_VRP_VECTOR(a+b+c+1:a+b+c+d) = X_ANT(1:d);
Y_VRP_VECTOR(a+b+c+1:a+b+c+d) = Y_ANT(1:d);

X_VRP_VECTOR(a+b+c+d+1:a+b+c+d+e) = X_ANT_LINE(1:e);
Y_VRP_VECTOR(a+b+c+d+1:a+b+c+d+e) = Y_ANT_LINE(1:e);
```

```
% (7) GENERATE MILLING TOOL PATH
%     -------------------------

TOOL_RAD = 4/1000;  % [m]

% NEW Y-INTERCEPTS
RHO_PROT = atan(SLOPE_PROT);
B_TOOL_PROT = B_PROT-sign(RHO_PROT)*TOOL_RAD./cos(RHO_PROT);

RHO_ANT = atan(SLOPE_ANT);
B_TOOL_ANT = B_ANT-sign(RHO_ANT)*TOOL_RAD./cos(RHO_ANT);

% INTERSECTION OF TWO LINES
for j = 2:n,
X_TOOL_PROT(j-1) = (B_TOOL_PROT(j)-B_TOOL_PROT(j-1))/...
                   (SLOPE_PROT(j-1)-SLOPE_PROT(j));
Y_TOOL_PROT(j-1) = (SLOPE_PROT(j-1)*B_TOOL_PROT(j)-SLOPE_PROT(j)*...
                   B_TOOL_PROT(j-1))/(SLOPE_PROT(j-1)-SLOPE_PROT(j));
end

for j = 2:n,
X_TOOL_ANT(j-1) = (B_TOOL_ANT(j)-B_TOOL_ANT(j-1))/...
                   (SLOPE_ANT(j-1)-SLOPE_ANT(j));
Y_TOOL_ANT(j-1) = (SLOPE_ANT(j-1)*B_TOOL_ANT(j)-SLOPE_ANT(j)*...
                   B_TOOL_ANT(j-1))/(SLOPE_ANT(j-1)-SLOPE_ANT(j));
end

% CLOSING OFF PULLEY
% LINES
X_PROT_i = (B_TOOL_ANT(n)-B_TOOL_PROT(1))/(SLOPE_PROT(1)-SLOPE_ANT(n));
Y_PROT_i = (SLOPE_PROT(1)*B_TOOL_ANT(n)-SLOPE_ANT(n)*B_TOOL_PROT(1))...
           /(SLOPE_PROT(1)-SLOPE_ANT(n));

X_PROT_LINE = X_PROT_i;
Y_PROT_LINE = Y_PROT_i;

X_ANT_LINE = X_PROT_i;
Y_ANT_LINE = Y_PROT_i;

% ARC
ARC_RADIUS1 = ((X_CENTER-X_TOOL_PROT(n-1))^2+...
              (Y_CENTER-Y_TOOL_PROT(n-1))^2)^0.5;
ARC_RADIUS2 = ((X_CENTER-X_TOOL_ANT(1))^2+(Y_CENTER-Y_TOOL_ANT(1))^2)^0.5;
ARC_RADIUS = (ARC_RADIUS1 + ARC_RADIUS2)/2;

X_ARC = X_CENTER+ARC_RADIUS.*cos(ALPHA);
Y_ARC = Y_CENTER+ARC_RADIUS.*sin(ALPHA);

% MILLING VECTOR
X_MILLING_VECTOR(1:a) = X_PROT_LINE(1:a);
Y_MILLING_VECTOR(1:a) = Y_PROT_LINE(1:a);

X_MILLING_VECTOR(a+1:a+b) = X_TOOL_PROT(1:b);
Y_MILLING_VECTOR(a+1:a+b) = Y_TOOL_PROT(1:b);

X_MILLING_VECTOR(a+b+1:a+b+c) = X_ARC(1:c);
Y_MILLING_VECTOR(a+b+1:a+b+c) = Y_ARC(1:c);

X_MILLING_VECTOR(a+b+c+1:a+b+c+d) = X_TOOL_ANT(1:d);
Y_MILLING_VECTOR(a+b+c+1:a+b+c+d) = Y_TOOL_ANT(1:d);

X_MILLING_VECTOR(a+b+c+d+1:a+b+c+d+e) = X_ANT_LINE(1:e);
Y_MILLING_VECTOR(a+b+c+d+1:a+b+c+d+e) = Y_ANT_LINE(1:e);

% (8) ROTATE VRP SURFACE COORDINATES
%     ----------------------------

OFFSET = pi/2;
ROTATE = OFFSET - atan2(Y_PROT_i,X_PROT_i);

MAG_VRP_VECTOR = (X_VRP_VECTOR.^2+Y_VRP_VECTOR.^2).^0.5;
PHASE_VRP_VECTOR = atan2(Y_VRP_VECTOR,X_VRP_VECTOR);

X_VRP_VECTORR = MAG_VRP_VECTOR.*cos(PHASE_VRP_VECTOR+ROTATE);
Y_VRP_VECTORR = MAG_VRP_VECTOR.*sin(PHASE_VRP_VECTOR+ROTATE);

MAG_MILLING_VECTOR = (X_MILLING_VECTOR.^2+Y_MILLING_VECTOR.^2).^0.5;
PHASE_MILLING_VECTOR = atan2(Y_MILLING_VECTOR,X_MILLING_VECTOR);

X_MILLING_VECTORR = MAG_MILLING_VECTOR.*cos(PHASE_MILLING_VECTOR+ROTATE);
Y_MILLING_VECTORR = MAG_MILLING_VECTOR.*sin(PHASE_MILLING_VECTOR+ROTATE);

VRP(:,1) = X_VRP_VECTORR'*1000;  % [mm]
VRP(:,2) = Y_VRP_VECTORR'*1000;  % [mm]

CNC(:,1) = X_MILLING_VECTORR'*1000;  % [mm]
CNC(:,2) = Y_MILLING_VECTORR'*1000;  % [mm]


% (9) SAVE VRP SURFACE COORDINATES AND TOOL PA'
%     ----------------------------------------

format short e
save VRP.scr VRP -ascii, save CNC.scr CNC -ascii;
```